DYNAMIC WIRELESS INTERROGATION OF ANTENNA-SENSOR IN HARSH ENVIRONMENT

by

JUN YAO

Presented to the Faculty of the Graduate School of
The University of Texas at Arlington in Partial Fulfillment
of the Requirements
for the Degree of

DOCTOR OF PHILOSOPHY

THE UNIVERSITY OF TEXAS AT ARLINGTON

November 2016

ACKNOWLEDGEMENTS

Foremost, I would like to express my sincere gratitude to my two advisors Dr. Saibun Tjuatja and Dr. Haiying Huang for the continuous support of my Ph.D. study and research. I would also like to extend my appreciation to the two professors for providing financial support for my doctoral studies and taking the time to critically evaluate this manuscript. Their enthusiasm and attitude toward research have deeply influenced me and helped me to do better researches.

Besides my advisors, I would like to thank the rest of my thesis defense committee: Dr. Jonathan Bredow, Dr. Robert Magnusson, Dr. Iohannis D. Schisms, for their interest in my research.

I would like to thank my lab colleagues from Advanced Sensor Technology Lab (ASTL), Franck, T. Mbanya and Farshad Zahedi for the simulation discussion and hardware system setup. I am also grateful to my former colleagues, Jeremiah Senders, Mauricio Jaguan, Austin Mears and Monica Hew for the sleepless nights we were working together before deadlines and for the fun we had during the past 4 years.

Finally, I would like to express my deep gratitude to my parents who have encouraged me, inspired me and sponsored my undergraduate and graduate studies. I also thank several of my friends who have helped me throughout my career.

November 18, 2016

ABSTRACT

DYNAMIC WIRELESS INTERROGATION OF ANTENNA-SENSOR IN HARSH ENVIRONMENT

JUN YAO, Ph.D.

The University of Texas at Arlington, 2016

Supervising Professors: Dr. Saibun Tjuatja and Dr. Haiying Huang

Microstrip antenna-sensor has received considerable interests in recent years due to its simple configuration, compact size, and multi-modality sensitivity. Due to its simple and conformal planar configuration, antenna-sensor can be easily attached on the structure surface for Structure Health Monitoring (SHM). As a promising sensor, the resonant frequency of the antenna-sensor is sensitive to different structure properties: such as planar stress, temperature, pressure and moisture. As a passive antenna, antenna-sensor's resonant frequency can be wirelessly interrogated at a middle range distance without using an on-board battery. However, a major challenge of antenna-sensor's wireless interrogation is to isolate the antenna backscattering from the background structure backscattering to avoid "self-jamming" problem. The goal of this thesis is to develop a high-speed wireless interrogation mechanism for antenna-sensor to realize real-time SHM. Furthermore, since the proposed antenna sensor-node is designed without using any electronics this dynamic remote sensing system can be used in high-temperature harsh environment.

In our researches, High-speed wireless interrogation of antenna-sensor for vibratory strain

sensing is firstly achieved in room temperature using an amplitude modulator and a Frequency Modulated Continue Wave (FMCW) interrogator. A rectangular patch antenna was bonded on aluminum beam to perform as a stress sensor as well as a wireless transceiver. By switching the load of the antenna-sensor between an open and a matching load using a square wave, the antenna backscattering signal is an amplitude modulated signal whose envelop is a square wave. The resonant frequency of the antenna-sensor can be determined at the frequency which has the largest amplitude in the envelop curve. Since the FMCW can sweep the interrogation frequency at a rate up to 300 Hz, real-time interrogation of antenna-sensor can be easily realized.

Far-field static antenna-senor interrogation for high temperature sensing was also developed. In this study, a patch antenna was used as temperature sensing unit and a Reactive Impedance Surface (RIS) based Ultra-wide Band (UWB) antenna was added as a passive wireless transceiver (Tx/Rx) for the antenna-sensor. A mircrostrip delay line was implemented in the sensor node circuitry to connect the Tx/Rx antenna and patch antenna-sensor. Since the new sensor node contains no electronics it can be applied in harsh environment which has a temperature up to 300 °C. Due to the time delay caused by the microstrip delay line in the sensor node, the antenna backscattering can be separated from the background structure backscattering in time domain using time-gating technology. The gated time domain sensing signal was converted into frequency domain using Fast Fourier Transform (FFT). The frequency spectrum of the gated signal indicates the reflection coefficient of the antenna-sensor and the resonant frequency of the antenna-sensor can be determined at the frequency which has the lowest reflection coefficient.

Furthermore, dynamic wireless interrogation of antenna-sensor for temperature sensing in harsh environment was realized by using a FMCW radar interrogator and non-electronics sensor node. Since this approach performs the time gating in the frequency domain instead of time domain substantial improvement on the interrogation speed can be achieved without adding any electronics in the sensor node. A down-conversion RF mixer was implemented in the interrogator circuit to demodulate the reflected FMCW interrogation signal and get the backscattering from both structure and sensor. Due to the difference of the beat frequencies of those two signals, the sensor backscattering can be easily separated from the structure backscattering using a digital band pass filter. In this study, a high interrogation speed of 50 Hz was achieved and the accuracy of the FMCW interrogator was validated using a temperature testing.

Compact FMCW interrogator was also developed for an antenna-based foot pressure sensing system. The interrogator consists of three parts: a FMCW synthesizer, a RF circulator and a power detector. The power consumption of this interrogator is only 160 mw and the interrogation rate is up to 55 Hz. Static pressure tests were performed to validate the accuracy of the proposed FMCW interrogator and the experimental results were compared with those from network analyzer measurements. The normalized discrepancies of two measurements are within 0.002%.

TABLE OF CONTENTS

LIST OF ILLUSTRATIONS

LIST OF TABLES

CHAPTER 1

INTRODUCTION

SHM is a technique used to detect and characterize the damage of engineering structures [1] [2]. Sensors which convert the physical properties into electric signals are becoming more and more significant in SHM technology since it observes the structure properties [3] [4] [5] [6] [7]. Various wired sensor, such as thermocouples [8] [9] [10], strain gauge [11] [12] [13], optical fiber sensors [14] [15] [16] [17] and etc. are developed and commonly used. However, these types of sensors can only be interrogated via wired connection which limits the mobility of dynamic systems and also requires high maintenance costs [18] [19]. Furthermore, wired sensing system cannot survive in the high-temperature harsh environment due to the temperature limitation of the cable and solder connections [20]. By eliminating the electric wiring of conventional sensors, wireless sensors are inexpensive and easier to install, which advances us one step closer to ubiquitous sensing [21] [22] [23]. A typical wireless sensing system can be separated into two parts: a wireless sensor and a wireless reader [24]. The wireless sensor is responsible for encoding the sensing information into a Radio Frequency (RF) signal that can be wirelessly transmitted via an antenna while the function of the wireless reader is to decode the received RF signal and extract the original sensing information. A wireless sensor can be broadly classified as either being active or passive, depending on whether it needs an on-board battery or not.

1.1 Active wireless sensor

Active wireless sensor requires an on-board battery to power the sensor node circuitry. In the circuitry, a microcontroller chip is used to perform sensing signal processing and wireless transmission [25] [26] and an on-board radio is also implemented to broadcast the sensing signal. Most active wireless sensors are designed based on the Berkeley mote platform [27] [28] [29]. A sensor module called "Telos" was designed based on the Berkeley mote platform and represented in [27]. In the circuitry of Telos, a Texas Instruments MSP430 microcontroller and a Chipcon IEEE 802.15.4-compliant radio were implemented. The maximum power consumption is around 40 mW.

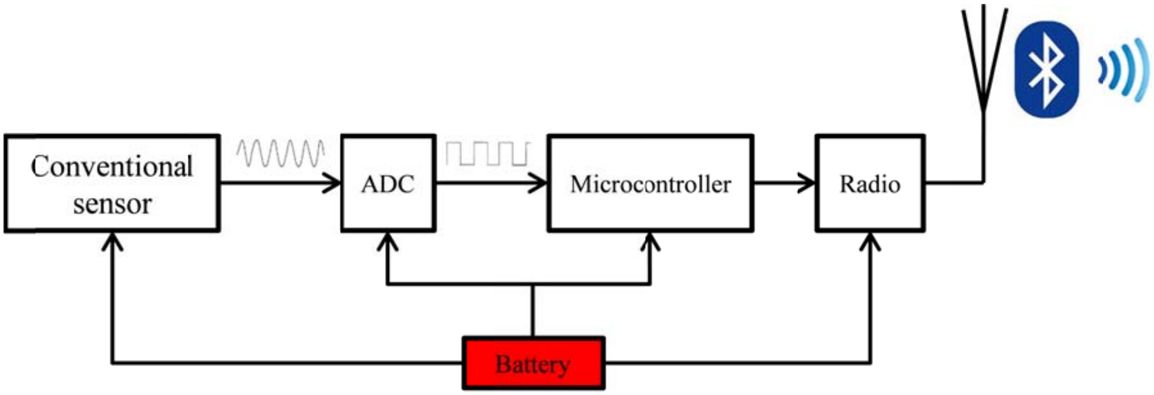

Figure 1.1 Block diagram of sensor node circuitry of Berkeley mote platform

The sensor node diagram of Berkeley mote platform active sensor is shown in Fig. 1.1. In the sensor node circuity, the sensing information is acquired as an analog signal then converted into digital signal using an Analog to Digital Convertor (ADC). The converted digital sensing signal will be processed by the microcontroller and wirelessly transmitted through a radio antenna using mature wireless protocol, such as Bluetooth and ZigBee. The advantage of this active sensing system is it can provide an interference-free data communication for a distance of more than 100 meters. However, one major limitation of the active wireless sensors is that they require an on-board battery in order to power the radio as well as the electronic components. Replacing or recharging the battery introduces a significant maintenance challenge [30].

1.2 Passive wireless sensor

Compare to active sensor, the main advantage of passive wireless sensor is that it does not require an on-board battery to power the sensor node circuitry. Passive sensors either consume no power at all or their power consumption is so low that it can be powered using the energy harvested from other sources. The operation time of the sensor is not limited by the battery life so that sensor node's maintenance cost can be reduced a lot. The passive wireless sensor can be classified into two categories depends on if there is electronics in the sensor node circuitry. Wireless Radio Frequency Identification (RFID) enable sensor is a typical wireless sensor with electronics. Non-electronics passive sensor includes Surface Acoustic Wave (SAW) sensor, inductive coupled sensor, and antenna sensor.

1.2.1 Wireless RFID enable sensor

Passive RFID sensor [31] [32] [33] is widely used for SHM due to its low-cost, long detection range and compact size. It can be classified into two major categories: chip RFID and chipless RFID sensor. In [34], a Wireless Identification and Sensing Platform (WISP) was represented using chip RFID sensor. Similar to an active wireless sensor, a WISP sensor is also equipped with a microprocessor, an ADC, an external memory and one or more conventional sensors [35] [36]. But the WISP sensor was powered by the energy harvested from the interrogation signal [37] rather than using an on-board battery. In order to achieve compact and low power RFID chip sensor, a CMOS temperature sensor was implemented into the RFID tag [38] [39]. Chipless RFID tags provide an identification code realized by nonchip-based means with physical permanent modification in the tag that modulated the reader's backscattered signal [40] [41]. In Girdau's paper [42], a resistive temperature sensor was implemented as the load of a UWB antenna that modulates the amplitude of the antenna backscattering as a function of temperature. A microstrip delay [43] [44] line is used to connect the UWB antenna and the sensor so that the tag mode antenna backscattering can be separated from the structural mode in the time domain.

Chipless temperature sensor with self-calibration ability was also developed by Girdau's group [45]. An operation amplifier based calibrator was added in the sensor-node circuit to remove the clutter and make the temperature measurement independent of the reader-tag distance and angle.

A solar-powered chipless RFID stress sensor was presented in [46] [47]. Based on a conventional thin-film strain gauge, the wireless sensor is capable of measuring both static and vibration deformations. The block diagram of the low-power wireless vibration system is shown in Fig 1.2. In order to achieve low power wireless transmission of the strain signal, a signal conditioning circuit is introduced to convert the low-frequency strain signals to a high frequency oscillatory signal whose frequency is directly controlled by the strain gauge output. As such, antenna backscattering can be exploited for wireless transmission of this oscillatory signal with zero power consumption. The sensor antenna, which receives the interrogation signal broadcasted by the wireless interrogator, is connected to a 50 Ω matching resistor via an impedance switch. When the impedance switch is on, the sensor antenna is connected to the matching resistor. Since the received antenna signal will be mostly dissipated by the 50 Ω

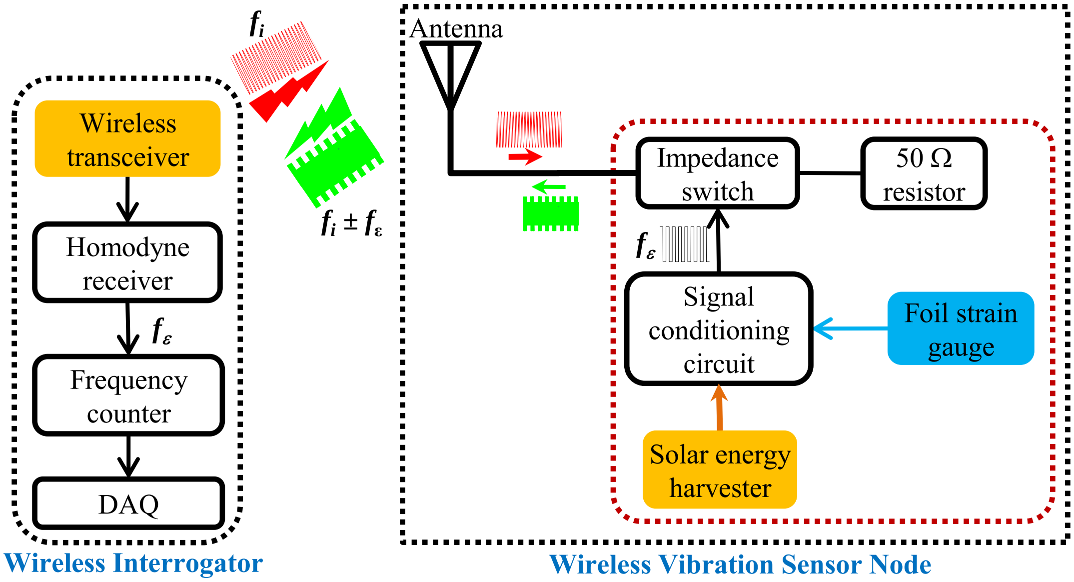

Figure 1.2 Low-power wireless vibration sensing system based on thin film strain gauge

resistor, very little energy will be reflected back and re-radiated by the sensor antenna. On the other hand, turning the switch off disconnects the sensor antenna from the 50 Ω resistor and thus terminates the sensor antenna with an open load. As such, all of the received signal will be reflected at the open load and re-radiated by the sensor antenna, resulting in a large antenna backscattering. Controlling the impedance switch using the oscillatory signal f_ε can then encode the frequency of the oscillatory signal in the amplitude modulation of the antenna backscattered signal. Due to this modulation, the backscattered sensing signal has a frequency component of $f_i \pm f_\varepsilon$. Once received by the wireless interrogator, the backscattered antenna signal $f_i \pm f_\varepsilon$ is passed through a homodyne receiver to recover the oscillatory signal f_ε, which is then input into a frequency counter that can determine the frequency of the oscillatory signal at a relatively high speed. Since f_ε is directly proportional to the strain experienced by the foil strain gauge, dynamic demodulation of the strain gauge output from the backscattered antenna signals can be achieved.

Both chip and chipless RFID wireless sensors require electronics in the sensor-node circuitry and most of the electronic components cannot survive in high temperature [42] [45] [46]. Therefore, RFID wireless sensors cannot be used in harsh environment.

1.2.2 Non-electronics wireless passive sensor

1.2.2.1 Wireless SAW sensor

The wireless SAW sensing system can be separated in two parts: an Electromagnetic (EM) transducer and a SAW sensor node [48] [49] [50]. The transducer is used to broadcast the interrogation EM wave to the sensor node and process the reflected EM wave to get the sensing information. The SAW sensor node consists of a piezoelectric substrate connected to a passive antenna. Reflectors are patterned on the piezoelectric substrate at short distance from the antenna connection [51] [52]. An incoming EM signal from the transducer is firstly received by the passive antenna and sent to the piezoelectric substrate to excite SAWs. The SAWs propagate along the substrate and get reflected back to the antenna once reaching the reflector. The variation of substrate physical properties will be encoded in the reflected SAWs which will be converted back into EM signal and re-broadcast to the EM transducer. Thus, the sensing information can be decoded in the transducer. In [53], a remote temperature sensing system using a SAW sensor and a passive dipole antenna was demonstrated. The temperature affects the propagation speed of the SAW so that it changes the time-delay of the reflected SAW. Since there is no electronics in the sensor node, the proposed SAW sensor can be applied in an environment with a high temperature which is up to 200 °C. Wireless stain sensing using SAW sensors are also represented in [54] [55] [56]. Since the SAW sensor is passive the lifetime of its sensing system is not limited to the lifetime of the battery. However, in order to keep a low SAW propagation loss, the frequency of the EM wave is limited to tens of megahertz. This frequency limitation makes the miniaturization of the passive antenna extremely difficult.

1.2.2.2 Wireless inductive coupled sensor

The inductive coupled sensing system consists a wireless reader and a wireless resonance sensor. The sensor node equivalent circuit is a RLC circuit. The resonant frequency of the RLC circuit is wirelessly detected via the inductive coupling between the sensor and reader coils [57] [58] [59]. Depending on the sensor, the measured quantity affects the capacitance, inductance and resistance of the sensor circuit. A wireless strain sensor was developed in [60] using inductive coupled sensor. The coil sensor acts like a LC resonance circuit, as shown in Fig. 1.3. Mechanical strain changes the inductance of the embedded sensor thus shift its resonant frequency. By wirelessly measuring the resonant frequency shift the strain can be calculated. In [61], a wireless hydrogel sensor was also demonstrated using the similar principle. Instead of

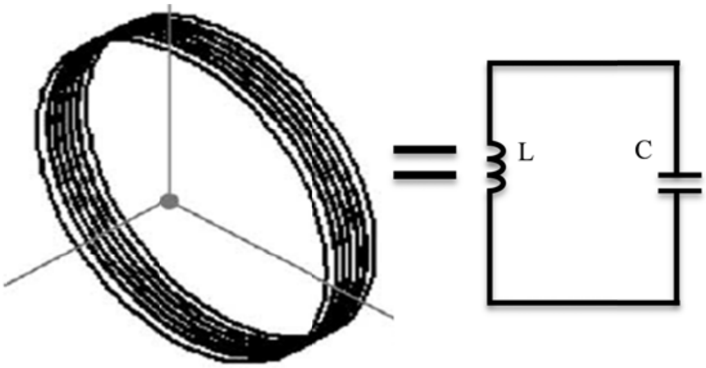

Figure 1.3 Inductive coupled strain sensor and its equivalent circuit

changing the inductance, a pressure sensitive capacitor was implemented in the sensor node to develop a wireless passive pressure sensor for pressure garment application [62]. Compared to SAW sensor, the inductive coupled sensor have a much simpler configuration and a smaller physical size. A major limitation of such sensor is that the interrogation distance is typically limited to be a few centimeters since the coils of sensor and reader should be placed near each other.

1.2.2.3 Wireless antenna-sensor

Antenna-sensor technology has received considerable researches and development interests due to its low cost, compact size, passive operation and multi-modality sensitivity [63] [64]. One unique advantage of the antenna-sensor is that it can act not only as a wireless transceiver but also a passive sensor. Therefore, antenna-sensors can be implemented with minimum number of components. As a promising sensor, its sensing ability for mechanical stress, temperature, pressure and crack has been demonstrated [65] [66] [67] [68]. In Tata's paper [65], a rectangular patch antenna was attached on a cantilever beam and the stress applied on the beam will be transferred onto the patch and change its physical dimension. Since the resonant frequency of the patch antenna-sensor is determined by its dimension, the stress applied on the beam changes antenna-sensor's resonant frequency. By monitoring the variation of antenna-sensor's resonant frequency using a network analyzer, the mechanical stress on the beam can be estimated. A temperature sensor was also proposed by Sanders using a patch antenna [66]. A radiation patch antenna-sensor was bonded on a metal base to perform as a temperature sensor. Temperature variation changes the dialectical constant of antenna-sensor's substrate as well as the physical dimension of the patch antenna, which will result in its resonant frequency shift. The relationship between the resonant frequency shift and temperature variation was calibrated and the accuracy of the temperature sensor was validated in the paper. Patch antenna-sensor was also used for structure crack detection [67]. The presence of a crack in the ground plane of the antenna-sensor increases the electrical length of the patch, which results in antenna-sensor's resonant frequency shift. In the paper, it shows 1 mm crack growth caused the antenna-sensor frequency to shift by 22.1 MHz.

Due to its simple and conformal planar configuration, antenna-sensor can be easily attached on the structure surface for SHM [69] [70]. By detecting the resonant frequency shift of the antenna-sensor, the structure physical properties can be determined. In the aspect of passive antenna, antenna-sensor can be wirelessly interrogated at middle range distances without an on-board battery [71].

1.2.3 Wireless interrogation mechanism of antenna-sensor

The wireless interrogation system for antenna-sensor can be separated into two parts: a wireless interrogator and wireless antenna-sensor node. First of all, an interrogation signal is broadcasted to the antenna-sensor node. After encoding the sensing information in the interrogation signal, the antenna sensor backscatters the modulated signal so that the wireless interrogator can retrieve the sensing information from the backscattered interrogation signal. The signals received by the wireless interrogator usually consist of both the signal backscattered by

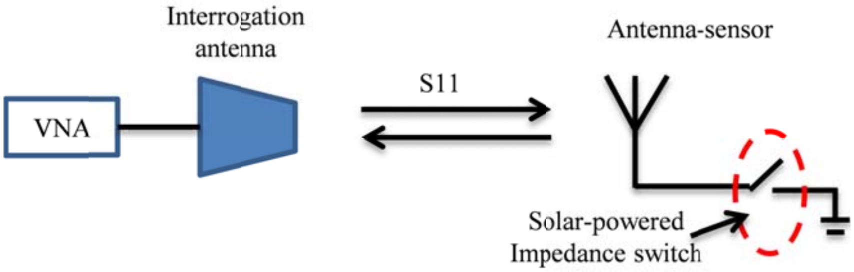

Figure 1.4 Wireless communication setup and sensor node circuitry of NTDR antenna-sensor interrogation

the antenna sensor, i.e. the antenna backscattering and the background clutter, which creates the “self-jamming” problem [64]. A major challenge for the wireless interrogator is therefore to isolate the antenna backscattering from the background clutter. Several wireless interrogation techniques that address the self-jamming problem have been developed including a widely used approach of “time gate interrogation” [71] [72] [73] [74] [75] [76], in which the reflected signal is time-gated to select the part of the signal that is concurrent with the antenna backscattering. The antenna resonant frequency can then be determined from the Inverse Discrete Fourier Transform (IDFT) of the time-gated signal. In Deshmukh’s paper [71], a wireless interrogation technique using Normalized Time Domain Reflectometry (NTDR) was proposed. The wireless interrogation setup and sensor node circuitry are demonstrated in Fig 1.4. A light-activated FET device was implemented to switch the load of antenna-sensor between open and short states. The interrogation antenna was connected with a network analyzer to measure the S parameters of the wireless interrogation at both states. The NTDR algorithm was then applied on the collected S parameters to extract antenna-sensor’s resonance information. By subtracting the time domain backscattering signal acquired at the two switch states, the structural backscattering was removed while the antenna backscattering was doubled. Time gate was applied to get the antenna backscattering signal. The gated time domain single was then converted into the frequency domain signal which stands for the resonant spectrum of the antenna-sensor. Therefore, the resonant frequency of the antenna-sensor can be determined at the frequency which has the largest amplitude in the spectrum curve. Another approach to address the self-jamming problem is to modulate the antenna backscattered signal. Xu and Huang [77] presented an amplitude modulation scheme using periodic impedance switching to modulate the amplitude of antenna backscattering. A down conversion mixer was used at the wireless interrogator to demodulate the amplitude modulated (AM) antenna sensing signal. The antenna resonant frequency was determined from the signal spectrum by stepping the interrogation frequency, which achieved much higher frequency resolution than the time-gating technique [71]. Wireless interrogation system that uses the RFID technology has also been published [78] [79] [80] [81] [82] [83]. An RFID chip is integrated into the antenna sensor circuitry and the antenna resonant efficiency is measured from the time it takes to charge the RFID energy harvesting chip. An RFID enabled temperature sensor was demonstrated by Qiao [80] using a 900 MHz patch antenna terminated with a RFID chip. The RFID harvest the energy from the interrogation signal. The antenna-sensor's resonant efficiency was measured from the maximum reading-range which can be calculated from the turn-on power of the RFID chip. Both approaches described, i.e. the frequency-stepping amplitude modulation scheme and the RFID-based interrogation, are suitable only for static sensing due to their inherently very low interrogation speed. Another drawback of those two wireless interrogation mechanisms is that they require electronics in sensor node and those electronics fails in high-temperature environment, which limits its application in harsh environment. Wireless interrogation without electronics for antenna-sensor is also developed.

A near-field interrogation mechanism for antenna-sensor was proposed in [84]. Patch antenna-sensor was considered as a radiative resonator and directly interrogated without using any electronics at a short distance. Time Domain (TD) gating technology was applied to capture the radiating signal form the antenna-sensor to determine its resonance frequency. However, since the patch-antenna has a relative low Quality (Q) factor [47] the maximum wireless interrogation distance of this mechanism is only 5 cm.

1.3 Research objectives and approaches

The Objective of this thesis is to develop high-speed wireless interrogation techniques in harsh environment for passive antenna-sensor.

Analytical models of microstrip rectangular patch antenna were firstly established. The resonant frequency of the antenna was sensitive to two factors: one is the physical dimension of the patch and the other one is the dialectical constant of its substrate. Structure characteristics change the two properties of the antenna-sensor, which results in antenna-sensor's resonant frequency shift. By monitoring this frequency shift the structure characteristic variation can be determined using the analytic model. The detail mathematic derivation of the analytic model of the antenna-sensor is discussed in CHAPTER 2.

Based on the analytical model of the antenna-sensor, patch antenna was implemented as a strain sensor and a dynamic wireless interrogation mechanism of antenna-sensor for vibration measurement was realized using a Frequency Modulated Continue Wave (FMCW) interrogator in room temperature. In [85], we exploited the FMCW radar principle [86] [87] [88] [89] [90] for dynamic wireless interrogation of the antenna-sensor. One of the most common FMCW signals, i.e. the periodic linear chirp, is used as the interrogation signal. By sweeping the interrogation frequency continuously with time, we can determine the antenna resonant frequency from the varying amplitude of the antenna backscattering since it is frequency dependent [65] [66] [67] [68] [91] and thus varies continuously with the interrogation frequency. CHAPTER 3 presents the development of an FMCW-based wireless interrogator with an interrogation rate up to 320

Hz and its demonstration for dynamic vibration measurements.

We also developed a novel far-field (60 cm) interrogation system of antenna-sensor for harsh environment temperature sensing [92]. In this study, a new sensor node was developed without using any electronics. In the sensor node, a patch antenna was used as temperature sensing unit and a RIS based UWB antenna [93] [94] was added as a passive wireless transceiver (Tx/Rx) for the antenna-sensor. Temperature variation shifts antenna-sensor's resonant frequency which can be determined from its reflection coefficient. The reflection coefficient of antenna-sensor was encoded in the reflected interrogation signal which was radiated through the Ultra-Wide Band (UWB) antenna to the interrogator. At the interrogator side, TD gating technology was applied on the reflected signal to separate the sensor mode data from the background clutter, and retrieve the real-time antenna-sensor's resonant frequency from its reflection coefficient. The sensor node design as well as wireless interrogation mechanism will be discussed in CHAPTER 4.

After achieving successful high-speed interrogation using FMCW interrogator in room temperature as well as the static wireless interrogation without electronics in harsh environment, combined technique was investigated. Dynamic wireless interrogation of antenna-sensor for temperature sensing in harsh environment was realized by using the FMCW radar interrogator and non-electronics sensor node. In this study, an interrogation rate of 50 Hz was achieved in high-temperature wireless sensing. The accuracy of the proposed dynamic FMCW interrogator was validated during the temperature testing by comparing the results to those measured from a Vector Network Analyzer (VNA) interrogator. The normalized discrepancy is only 3%. The operation principle, hardware setup and validation testing will be presented in CHAPTER 5.

Compact FMCW interrogator was also developed for foot pressure sensing system [95]. A PCB FMCW synthesizer [96] was developed with a compact dimension and a low power consumption of 160 mw. The proposed potable interrogator can be powered by a fully charged 3.7V battery for 8 hours. The accuracy of this compact interrogation circuit and the antenna-based pressure sensor was validated using a static pressure testing. The operation principle of the antenna pressure sensor, design of the FMCW synthesizer and the validation pressure testing will be discussed in CHAPTER 6.

Finally, in CHAPTER 7, the conclusion will be draw and the future work will be discussed.

CHAPTER 2

ANALYTICAL MODEL OF MICROSTRIP PATCH ANTENNA

The microstrip rectangular patch antenna, as shown in Fig. 2.1, consists of three layers: radiation patch, dielectric substrate, and metallic ground plane. The resonant frequency of a rectangular patch antenna can be calculated as

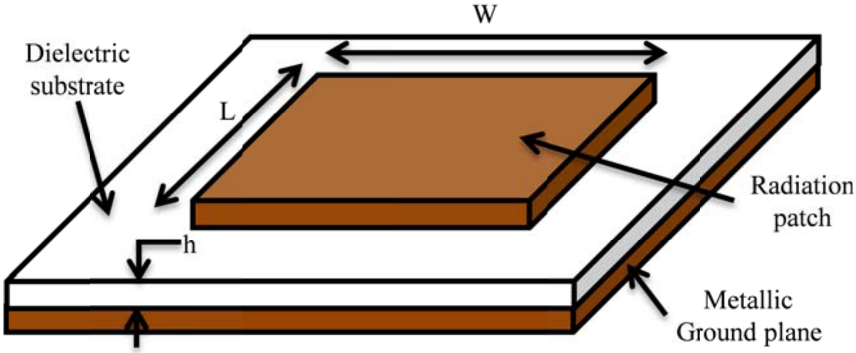

Figure 2.1 Microstrip rectangular patch antenna demonstration

$$f_{mn} = \frac{C}{2\sqrt{\varepsilon_{reff}}}\sqrt{\left(\frac{m\pi}{L}\right)^2 + \left(\frac{n\pi}{W}\right)^2}, \tag{2.1}$$

where C is the speed of the light; L and W are the physical length and width of the radiation patch. (m, n) represents the resonant orders; for an antenna with a rectangular radiation patch, the fundamental (1,0) mode, i.e. the TM_{10} mode, has the current flow along the length direction while the fundamental (0,1) mode, i.e. the TM_{01} mode, has the current flow along the width direction. Since Equation (2.1) for the TM_{10} and TM_{01} mode is almost identical, we will focus on the TM_{10} mode in the following derivations. The resonant frequency of the TM_{10} mode can be simplified from equation (2.1) as:

$$f_{10} = \frac{C}{2\sqrt{\varepsilon_{reff}}}\frac{1}{L}. \tag{2.2}$$

ε_{reff} is effective dielectric constant [97] which can be calculated from the dielectric constant of the substrate ε_r, the substrate thickness h, and the width of the radiation patch W as:

$$\varepsilon_{reff} = \frac{\varepsilon_r + 1}{2} + \frac{\varepsilon_r - 1}{2\sqrt{1 + 10h/W}}. \tag{2.3}$$

When the substrate thickness h is much smaller than the dimensions of the radiation patch, $h<<W$ and $h<<L$, the effective dielectric constant can be approximated as the dielectric constant of the substrate, i.e. $\varepsilon_{reff} \approx \varepsilon_r$. As a results, (2.3) can be simplified to

$$f_{10} = \frac{C}{2\sqrt{\varepsilon_r}}\frac{1}{L}. \tag{2.4}$$

The resonant frequency variation δf_{10} can then be expressed in terms of the changes in the substrate dielectric constant ε_r and the patch length L, i.e.

$$\delta f_{10} = \frac{\partial f_{10}}{\partial \varepsilon_r}\delta\varepsilon_r + \frac{\partial f_{10}}{\partial L_e}\delta L. \tag{2.5}$$

From equation (2.4) we can also derive that

$$\frac{\partial f_{10}}{\partial \varepsilon_r} = \left(-\frac{1}{2\varepsilon_r}\right) f_{10} \tag{2.6}$$

and

$$\frac{\partial f_{10}}{\partial L_e} = \left(-\frac{1}{L_e}\right) f_{10}. \tag{2.7}$$

Substituting equations (2.6) and (2.7) into (2.5) and normalizing the shift of resonant frequency with the antenna's initial resonant frequency, we obtain

$$\frac{\partial f_{10}}{f_{10}} = -\frac{1}{2}\frac{\partial \varepsilon_r}{\partial \varepsilon_r} - \frac{\partial L}{L}. \tag{2.8}$$

Equation (2.8) serves as the theoretical foundation of the antenna-sensor. The first term represents the sensitivity of the antenna resonant frequency to the effective dielectric constant changes of the antenna, which can be exploited for environment (e.g. temperature, moisture, gas etc.) and bio-chemical sensing. The second term represents the sensitivity of the antenna resonant frequency to the dimension change of the radiation patch, which can be related to strain, crack, and temperature changes.

CHAPTER 3

REAL-TIME VIBRATORY STRAIN SENSING USING PASSIVE WIRELESS ANTENNA-SENSOR

3.1 Operation principle

The wireless vibratory strain sensing system can be separated into two subsystems, as shown in Fig. 3.1; a wireless interrogator and a wireless passive strain sensor. The wireless interrogator consists of a transmitter that sends interrogation signal, a receiver/demodulator that processes the backscattered signal, and a Data Acquisition (DAQ) to facilitate digital signal processing. A horn antenna is utilized in the wireless interrogator, and the transmitted and received signals are separated using an RF circulator. The wireless passive strain sensor consists of a microstrip patch antenna and an AM modulator with energy harvesting capability. The microstrip patch is designed to function as both a dynamic strain sensor as well as a wireless communication antenna. Mechanical tensile strain changes the dimensions of the antenna sensor, which in turn changes the antenna resonant frequency [65]. Thus, the strain on the patch antenna can be estimated from the resonant frequency shift in the backscattered signal of the antenna. To improve detection of sensor node backscattered signal, i.e. avoiding self-jamming, the load of the antenna-sensor is periodically switched at frequency f_m between high-impedance (open-circuit) and matched-load, thus effectively amplitude modulate the backscattered signal. The switching circuit (AM modulator) consists of an oscillator, microwave switch and a 50Ω load. For passive sensor node operation, energy harvesting circuit is used to power the modulator; a solar-powered modulator is used in this study. By controlling the switch using solar-powered oscillator, the amplitude of the antenna-sensor backscattering is modulated at the set oscillator frequency f_m.

The frequency of the antenna-sensor backscattered signal is therefore offset by the modulation frequency f_m and thus is separated from the much stronger interrogation signal in the frequency domain [48]. The antenna-sensor's resonance information is encoded in the amplitude of the modulated backscattered signal. The amplitude of the backscattered signal is maximum when the interrogation frequency matches the resonant frequency antenna-sensor, and it decreases as the interrogation frequency moves away from the antenna-sensor resonant frequency.

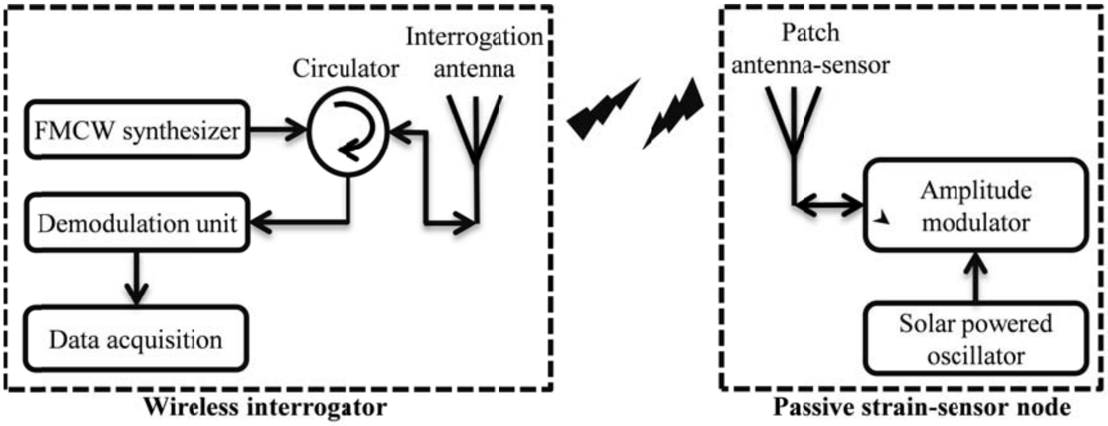

Figure 3.1 Block diagram of the wireless vibratory strain sensing system

In order to measure the antenna-sensor resonant frequency dynamically, as required in a vibratory environment, the wireless interrogator must have capabilities for fast signal acquisition and processing. In this study, a combined FMCW and envelope detection technique is utilized for the wireless interrogator. The FMCW interrogation signal is generated using an FMCW synthesizer and envelope detection is implemented in the signal demodulator (as shown in Fig. 3.1).The interrogation signal frequency generated by the FMCW synthesizer is a periodic linear function of time, and the corresponding antenna-sensor backscattered signal, whose amplitude changes with the interrogation frequency, also varies with time. To demodulate the antenna-sensor backscattering from the received signal, which consists of background clutter and antenna backscattering, the received signal is first directed to the demodulation unit by the RF circulator.

The demodulation unit recovers the envelope of the received signal using an envelope detector. Since the demodulated antenna-sensor backscattered signal has frequency f_m (due to AM modulation at the sensor), a band pass filter with a narrow bandwidth centered at f_m can then be applied to the demodulated signal to extract the antenna-sensor information and to remove the background clutter and additive noise. After acquiring the filtered envelop signal using a Data Acquisition (DAQ) device, a Digital Signal Processing (DSP) algorithm can be applied to track the time-varying amplitude of the acquired antenna-sensor backscattered signal. By synchronizing the demodulated antenna-sensor backscattered signal with the input of the FMCW synthesizer (i.e. the low-pass periodic signal and for linear FMCW a saw tooth signal) the antenna resonant frequency shift can be estimated from the amplitude changes of the acquired signal, from which the strain variation can be determined.

3.2 Hardware implementation

3.2.1 Design of passive strain-sensor node

3.2.1.1 Design of antenna-sensor for strain sensing

In this study, a rectangular patch antenna was used to monitor the mechanical strain alone its length direction. The antenna-sensor was designed using Rogers RT/duroid® 5880 Laminates [98]. The dielectric constant of the substrate material is 2.2 and the thickness is 0.787 mm. Antenna-sensor's physical dimension is shown in Fig. 3.2 and the simulated S11 curve was represented in Fig. 3.3. As seen from fig. 3.2, the feeding point of the antenna-sensor was set in the middle of the bottom edge to eliminate the resonant frequency of TM_{01} mode. From Fig 3.3 we can see that the simulated TM_{10} mode resonant frequency of the designed antenna-sensor is 5.39 GHz. Since this antenna-sensor is designed for strain sensing in a stable room temperature we assume that the dielectric constant of the subtract material is a constant. Thus, the equation

(2.8) can be simplified as

$$\frac{\partial f_{10}}{f_{10}} = -\frac{\partial L}{L} = K_S \varepsilon_L. \tag{3.1}$$

In equation (3.1), $\frac{\partial L}{L}$ is defined as the mechanical strain which is along antenna-sensor's length direction. K_S is defined as the strain sensitivity of the normalized frequency shift. In this case, the theoretical K_S can be calculated as -1 ppm/με.

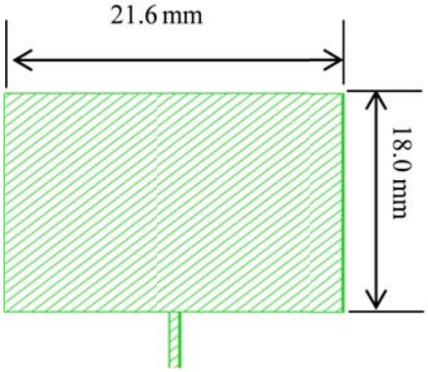

Figure 3.2 Physical dimension of the designed patch antenna-sensor

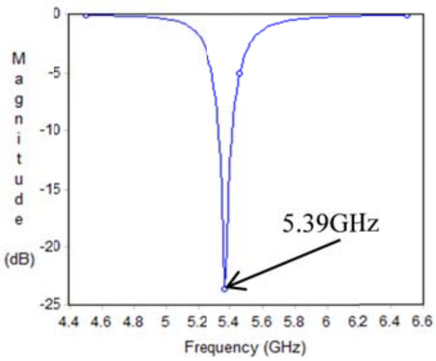

Figure 3.3 Simulated reflection coefficient of the designed antenna-sensor

3.2.1.2 Sensor node circuitry design for amplitude modulation

The circuit diagram of the passive strain-sensor node that includes the patch antenna sensor and a light-powered amplitude modulator is shown in Fig. 3.4. An impedance switch was implemented using a pseudomorphic High Electron Mobility Transistor (pHEMT) [99] [100]. The gate of the pHEMT is connected to the oscillator with an oscillating frequency f_m = 32.78 kHz. When the gate voltage V_C is high, the switch is turned "ON" and the patch antenna is connected to the matching load (e.g. a 50 Ω resistor). At this state, most of the interrogation signal received by the patch antenna is absorbed by the matching load. As a result, almost no RF signal is backscattered by the antenna-sensor node. When the gate voltage is low, the switch is "OFF" and the path between the patch antenna and the matching load is cut off. As such, the patch antenna is effectively terminated with an open circuit (high impedance) and most of the received interrogation-signal is reflected back. The periodic switching of the pHEMT therefore results in an amplitude modulated antenna backscattering.

The hardware implementation of the passive strain-sensor node is shown in Fig. 3.5. The patch antenna sensor was fabricated on the dielectric substrate using a chemical etching technique and bonded on an aluminum specimen with super glue. A microstrip transmission line for impedance matching was implemented to connect the antenna patch to the pHEMT, which was soldered to the microstrip transmission lines. A 50 W terminator was connected to the source terminal of the pHEMT through a SMA connector and a microstrip transmission line. The gate terminal of the pHEMT was connected to the output of the oscillator that was powered by a small solar cell.

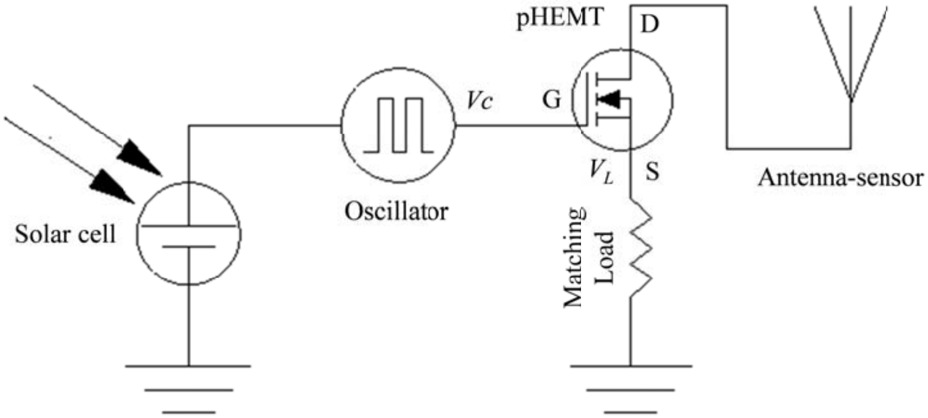

Figure 3.4 Diagram of wireless antenna strain sensor node

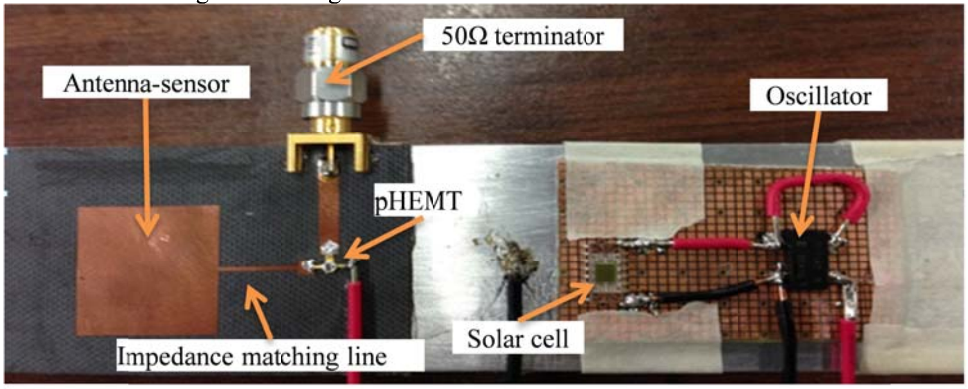

Figure 3.5 Hardware implementation of the passive strain-sensor node

Both the oscillator and the solar cell were soldered on a printed circuit prototype board placed at a location close to the antenna sensor.

To validate the amplitude modulation circuit, a 5.45 GHz signal was broadcasted to the sensor node though an interrogation horn antenna. The matching load was replaced by an oscilloscope with a 50 Ω coupling. As such, the oscilloscope measurement is the reciprocal of the antenna backscattering. Fig 3.6(a) shows the measured waveform of the gate control voltage V_C (i.e. the oscillator output) while the associated RF signal V_L measured by the oscilloscope is shown in Fig. 3.6(b). It is evident that the signal acquired by the oscilloscope is amplitude modulated in response to the control gate voltage V_C. However, the pHEMT switch was not complete cut-off at the "OFF" state. Assuming the received power is completely absorbed by the matching load, we can calculate the insertion losses of the antenna sensor at the two switching states based on

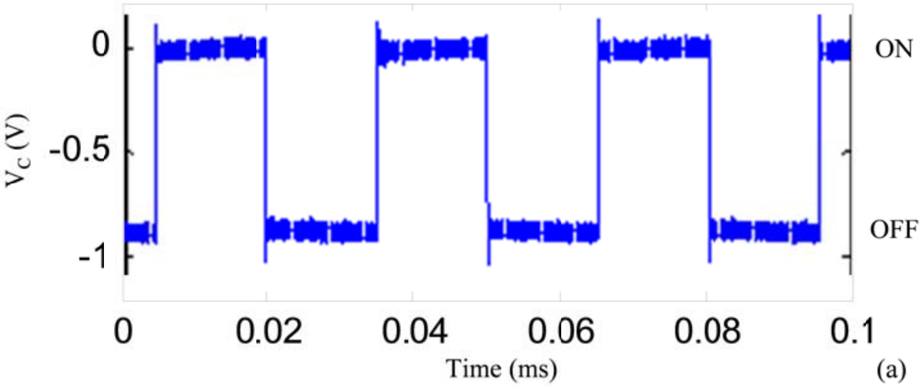

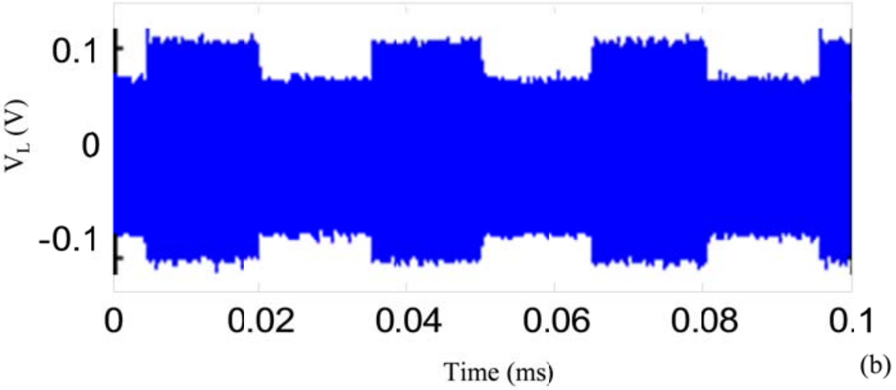

Figure 3.6 Gate control voltage and normalized RF signal at matching load

the signal shown in Fig. 3.6(b). The power received by the patch antenna P_r can be calculated to be 0.149 mW using Friis equation [101] [102], i.e.

$$P_r = P_t G_r G_t \left(\frac{\lambda}{4\pi d}\right)^2, \tag{3.2}$$

where the transmitted power P_t is 20 dBm, the interrogation distance d is 90 cm, the wavelength is 55 mm, and the gains of interrogation antenna Gt and antenna sensor G_r are 12 dBi and 6 dBi, respectively. The signal shown in Figure 7(b) has an amplitude of 0.1 V at the "ON" state and an amplitude of 0.07 V at the "OFF" state. Therefore, the power received by the 50 Ω load is 0.1 mW at the "ON" state and is 0.05 mW at the "OFF" state. The insertion losses of the sensor node can thus be calculated as -4.8 dB and -1.75 dB for the "ON" and "OFF" states, respectively.

The power consumption of the entire sensor-node circuit was measured to be 0.63 mW and was provided by a 3.2 mm* 2.5 mm solar cell illuminated by a 134 lm light-emitting-diode (LED). The illumination light was focused on the photocell using a magnifying lens. It was discovered that the modulation circuit is powered up when the focused spot is about the same size as the solar cell. Therefore, the illumination intensity can be estimated to be 134 lm / (0.0032m*0.0025m) = 16,750,000 lux, which is around 170 times larger than that of the sunlight, assuming the intensity of the sunlight is 98,000 lux. Accordingly, the area of the solar cell should be increased by 170 times in order to power the sensor node by direct sunlight. In other words, the sensor node can be powered by direct sunlight using a square solar cell with a length and width of 37.0 mm. As long as the interrogator is implemented with a light source, the sensor node can be interrogated at any time and location even though there is no direct sunlight.

3.2.2 Design of dynamic wireless interrogator

3.2.2.1 FMCW generator

The block diagram and implementation of the FMCW synthesizer is shown in Fig 3.7 and 3.8, respectively. A periodic linear chirp is implemented by using a Voltage Control Oscillator (VCO) controlled by a "saw tooth" signal. As such, the instantaneous frequency of the chirp is swept through a frequency range continuously during each period of the "saw tooth" signal. The sweeping rate and the frequency range of the chirp signal can be adjusted by changing the frequency and the amplitude of the "saw tooth" control signal. Since the resonant frequency of the sensor node circuit is 5.45 GHz, a frequency multiplier was used to double the frequency of the VCO output so that the interrogation signal frequency can be swept from 5.42 GHz to 5.47 GHz. The multiplier output is amplified by a microwave amplifier that has a gain of 30 dB to reach the desired amplitude of 25 dbm.

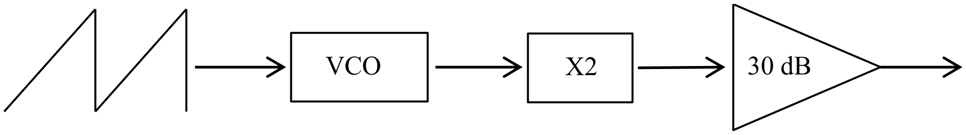

Figure 3.7 Block diagram of VCO-based FMCW synthesizer

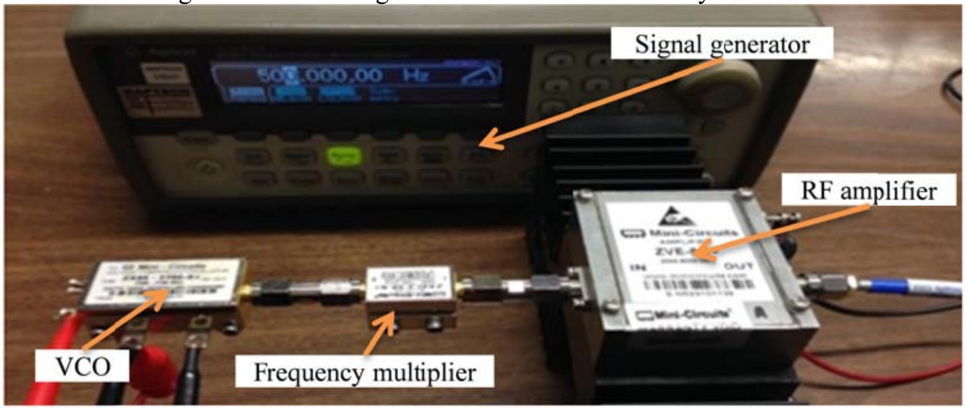

Figure 3.8 Hardware implementation of FMCW synthesizer

3.2.2.2 Demodulation unit

The circuit diagram and the hardware implementation of the demodulation unit are shown in Fig. 3.9 and Fig. 3.10, respectively. The demodulation unit was constructed by using two commercially available devices: a prototype board for an RF envelope detector chip and a band pass filter with a built-in amplifier.

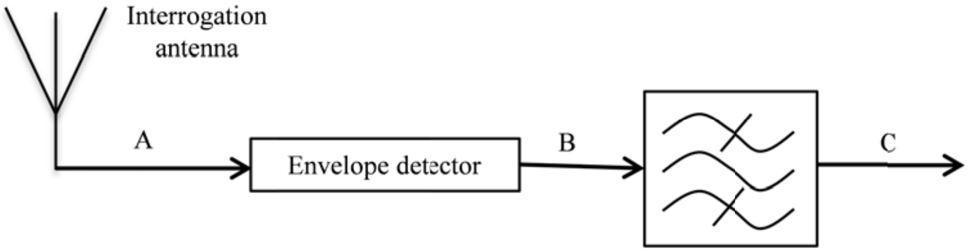

Figure 3.9 Block diagram of VCO-based FMCW synthesizer

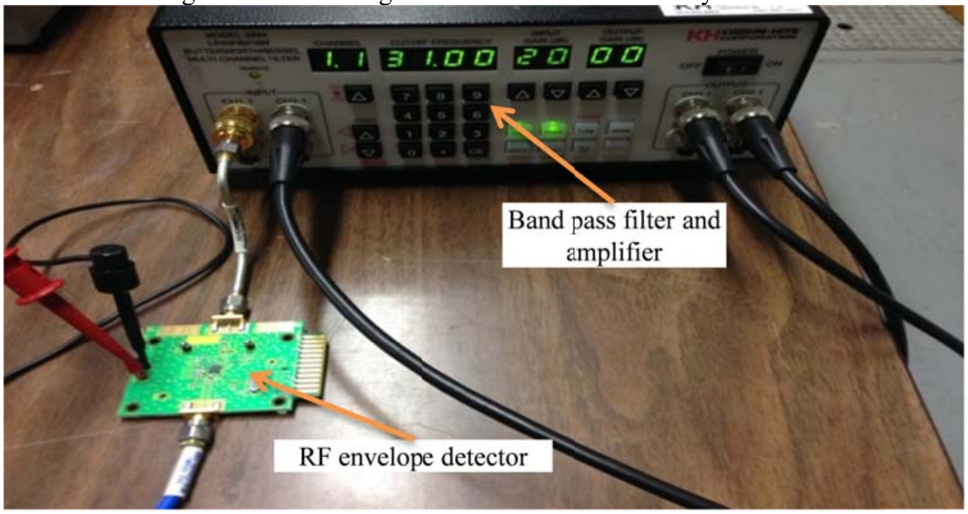

Figure 3.10 Hardware implementation of demodulation unit

The signals at three stages, i.e. as received by the interrogation antenna (signal A), at the output of the envelope detector (signal B), and at the output of the band pass filter (signal C), are illustrated in Fig. 3.11. Signal A contains both the antenna-sensor backscattering and the background clutter. The slight amplitude variation of this signal is contributed by the amplitude modulation of the antenna backscattering. Passing signal A through the envelope detector produces signal B, which represents the envelope of signal A. Since the amplitude modulation was achieved by switching the impedance of the antenna load, the resulting envelope is a square wave having the same frequency as the impedance-switching frequency f_m. Therefore, a narrow band pass filter centered at f_m can be applied to remove the noise and to facilitate easy detection of the time-varying amplitude. As shown in Fig. 3.11, the output of the band pass filter, i.e.

signal C, is a sinusoidal signal with continuously varying amplitude. Since signal C has a relatively low frequency, it can be directly acquired using a DAQ device for digital data processing.

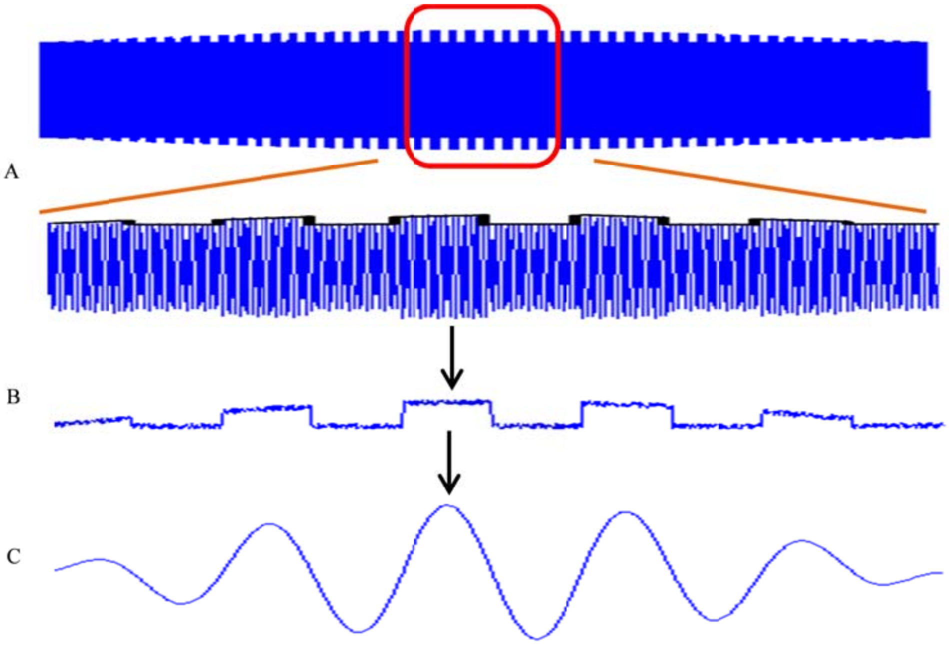

Figure 3.11 Signals at different demodulation stages

The maximum interrogation distance depends on the detection sensitivity of the demodulation unit, the transmission losses between the interrogator and the sensor antennas, and the insertion losses of the antenna sensor at the two switching states. Since the backscattered signal was sent to the RF envelop detector without any amplification, the minimum amplitude that can be sensed by the envelope detector then becomes the sensitivity of the demodulation unit. For the envelope detector we used, the sensitivity was calibrated to be 100 mV, which means the amplitude change of the signal shown in Fig. 3.11(a) has to be larger than 100 mV to be detected. The amplitude of the backscattered signal can be expressed as

$$V_{BS}^{(m)} = \sqrt{2P_{BS}^{(m)}R}, \tag{3.3}$$

in which *(m)* represents the impedance switching state, i.e. “ON” or “OFF”, and R is the input impedance of the envelope detection, which is 50 W. $P_{BS}^{(m)}$ is the power of the backscattered signal and can be calculated as

$$P_{BS}^{(m)} = P_t + 2L_{path} + L_{insertion,}^{(m)} \tag{3.4}$$

where P_t is the transmitted power, $L_{insertion}^{(m)}$ is the insertion loss of the sensor node calculated in section III.A, and L_{path} is the transmission loss between the interrogator and sensor antennas, which can be calculated from equation (2) as

$$L_{path} = G_t G_r \left(\frac{\lambda}{4\pi d}\right)^2. \tag{3.5}$$

In equation (4), the transmission path loss is doubled because of the round-trip transmission between the interrogator and sensor. Finally, the envelope amplitude of the backscattered signal can be calculated as

$$V_{AM} = \frac{V_{BS}^{(off)} - V_{BS}^{(on)}}{2}. \tag{3.6}$$

Based on equations (3)-(6), the relationship between the envelope amplitude V_{AM} and the interrogation distance d can be calculated and is plotted in Fig. 3.12, using P_t = 25 dBm and the parameters given in section 3.2.1. The maximum interrogation distance is then estimated to be 2.87 m based on the envelope detector sensitivity of 100 mV. Larger interrogation distances can be achieved using a higher transmission power, a higher gain interrogation antenna or a better impedance switch at the sensor node. For example, according to the Federal Communications Commission (FCC) regulation, the transmitted power can be increased to 30 dBm and the gain of the interrogation antenna can be increased to 23 dBi. These increases will increase the interrogation distance to 13.6 m. In the idea case of $L_{insertion}^{(off)} = 0\,dB$, P_t = 30 dBm, and G_t = 23 dBi, the maximum interrogation distance that can be achieved is 18 m.

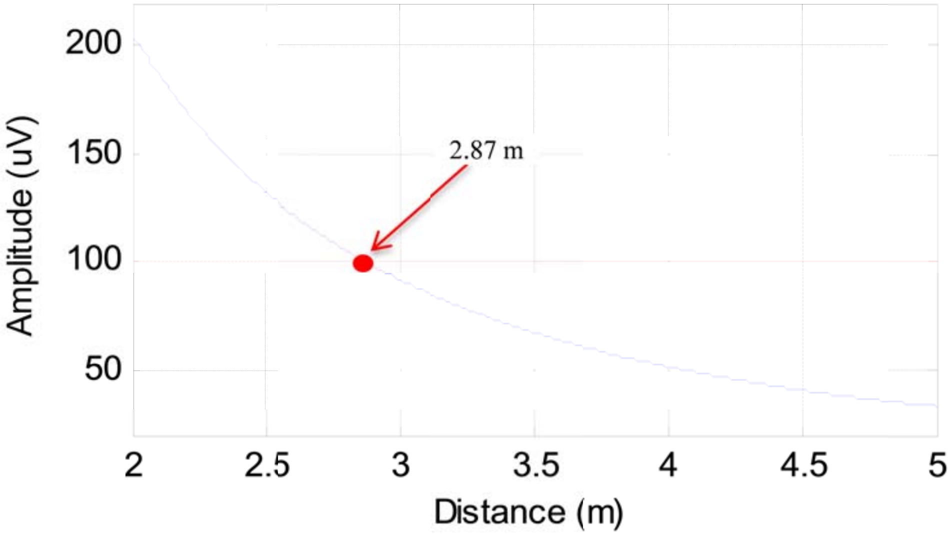

Figure 3.12 Relationship between the amplitude of the modulated square wave and the wireless transmission distance

3.2.2.3 Real-time digital signal processing

The flow chart of the DSP algorithm is shown in Fig. 3.13(a) and the signals corresponding to each block are shown sequentially in Fig. 3.13(b). Firstly, the acquired signal, i.e. signal C, is segmented into data arrays with each array corresponding to one FMCW period. A digital envelope detector is then applied to extract the time-varying amplitude of each array. These amplitude data are filtered using a second order Butterworth low pass filter with a cutoff frequency of 2 kHz to remove the high frequency noise. To account for the amplitude variations, the amplitude data are normalized with respect to the maximum value in each data array. The time scale can then be converted to the frequency scale based on the calibrated time-frequency relationship of the FMCW synthesizer so that the resonant frequency shift of the antenna sensor can be determined. The frequency shift of the normalized amplitude signals between two consecutive FMCW periods is determined from the frequencies of the amplitude signals at a selected reference value. Finally, the strain experienced by the antenna sensor is calculated from the measured frequency shift based on equation (3.1).

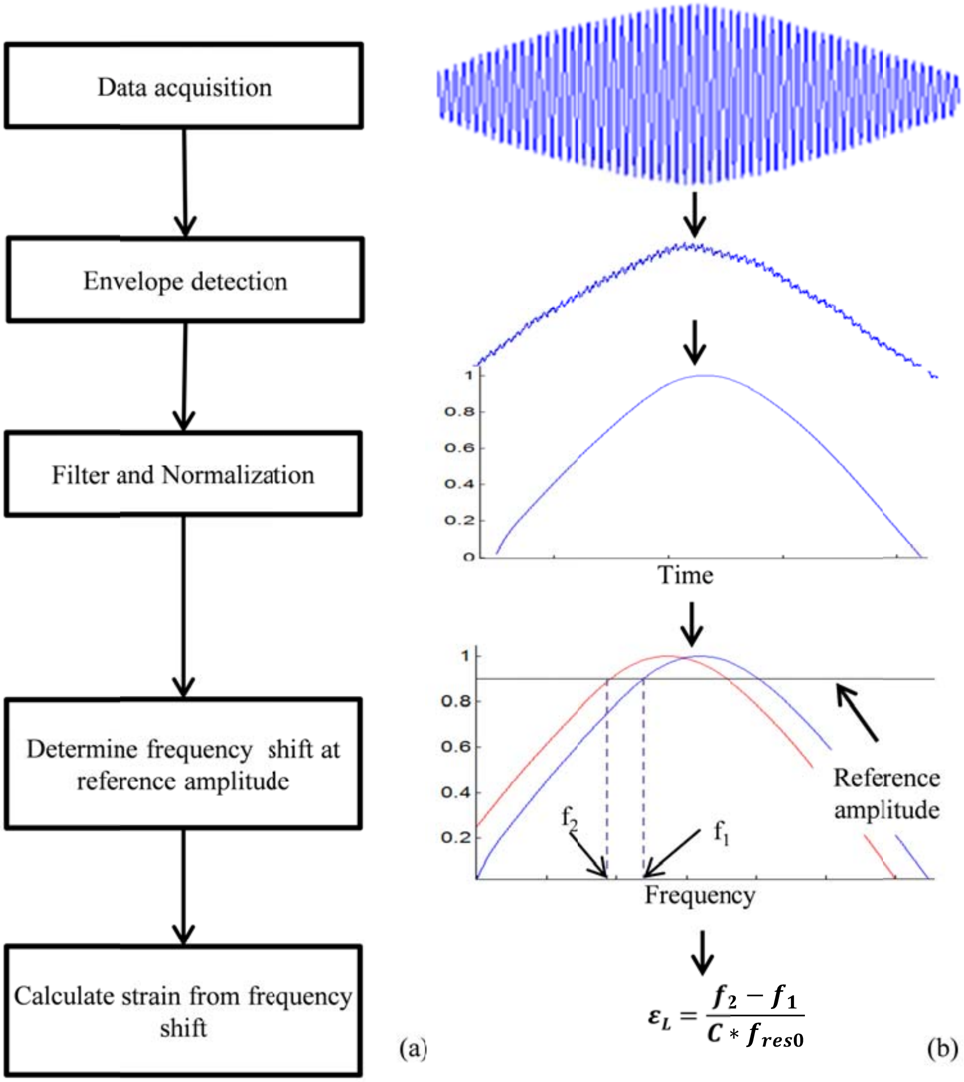

Figure 3.13 Illustration of digital signal processing algorithm; (a) flow diagram; (b) signals corresponding to processing blocks

The sampling rate of the dynamic interrogator is limited by several factors: the Q factor of the microstrip antenna, the sweeping rate of the FMCW synthesizer, the amplitude modulation frequency f_m, and the DSP algorithm. The Q factor of the fabricated patch antenna was measured to be around 100, which means it has a time delay constant of around 6 ns. Therefore, the sampling rate is limited to be less than 167 MHz in order to ensure that the resonance of the antenna sensor has died down before starting the next interrogation cycle. On the other hand, the antenna resonant frequency was detected based on the time-varying amplitude of every FMCW period. As such, there should be multiple amplitude modulation cycles for each FMCW period. Our tests have shown that 10 amplitude modulation cycles in one FMCW period is sufficient for extracting the antenna resonant frequency. Since the modulation frequency f_m is fixed at 32.78 kHz, the maximum sampling rate is therefore limited to be 3.2 kHz. When we increased the modulation frequency to 800 kHz, however, we were able to achieve a sampling rate of 78 kHz. In this case, the sampling rate is limited by the scan rate of the FMCW synthesizer. The above tests were conducted under the condition that a stable amplitude modulated signal, i.e. the signal shown in Fig. 3.11(c), is obtained by the oscilloscope. The antenna resonant frequency, however, was extracted from this signal using the DSP algorithm shown in Fig. 3.13. Compared to the other three factors mentioned above, the DSP algorithm takes a much longer time to execute since it is implemented using the built-in MATLAB program of the oscilloscope. For each array data, it took the algorithm 12.5 ms to process, which limits the sampling rate to 1/12.5 ms = 320 Hz. To increase the sampling rate, we could implement some of the functions described in Fig. 3.13, such as the envelope detection, using analog circuits and implementing the program in a real-time digital signal processor.

3.3 Experiment and data analysis

3.3.1 System setup

In order to evaluate the strain-tracking performance of this wireless strain monitoring system both static and dynamic tensile tests were performed. The experimental setup is shown in Fig. 3.14. An Instron tensile machine was used to apply axial loads to the aluminum specimen. An RF horn antenna was set up to face the microstrip patch as an interrogation antenna. Due to the space limitation the distance between the interrogation horn antenna and the patch antenna sensor was set as 90 cm. Solar light was emitted by a 134 lm LED which was located next to the horn antenna and focused on the photocell by using a magnifying lens. A high-speed oscilloscope was used as the DAQ receiver where the sampling rate was set at 500 kHz and 1000 samples were collected in each data array within one FMCW period. Since the frequency sweeping range is 50 MHz, the frequency resolution of the DAQ system is therefore $50*10^6/1000 = 50$ kHz, resulting in a relative frequency resolution of 9.26 ppm for a 5.45 GHz patch antenna.

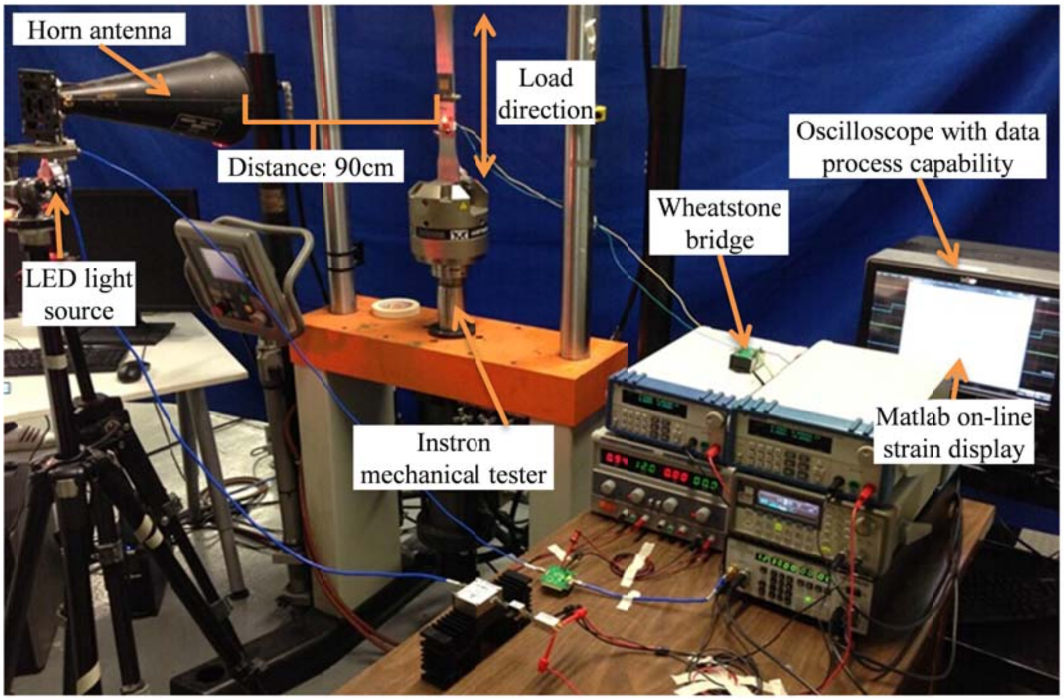

Figure 3.14 Experiment setup for static and dynamic tests of wireless antenna strain sensor

For validation and data comparison, the strains applied on the specimen were directly measured by a resistive foil strain gauge, which was attached on the back side of the aluminum beam. A ¼-bridge Wheatstone bridge was connected with the strain gauge to convert the mechanical strain ε into an electrical output V_{out}. The strain ε was calculated from the output voltage of the Wheatstone bridge V_{out}, the excitation voltage V_{ex}, and the gauge factor of the strain gauge GF as

$$\varepsilon = \frac{4V_{out}}{GF \cdot V_{ex}}, \tag{3.7}$$

in which V_{ex} = 10V and GF = 2.13.

Both static and dynamic tensile tests were performed to evaluate the performance of the wireless strain monitoring system. Static tensile tests were conducted to calibrate the sensitivity of the antenna sensor. Static axial loads, ranging from 500 lb to 3500 lb with an increment of 500 lb, were applied on the aluminum beam. Vibratory strain tests were carried out to evaluate the dynamic response of the strain sensing system. A sinusoidal tensile load, varying from a minimum of 500 lb to a maximum of 3500 lb, was applied to the specimen at different loading frequencies.

3.3.2 Testing results and discussion

3.3.2.1 Calibration of antenna sensor for static tensile test

The normalized envelopes of the demodulated signal at different static loads are shown in Fig. 3.15. It is evident that the antenna resonant frequency decreases as the load increases. To correlate the frequency shift to the applied strain, the normalized amplitude of 0.99 was selected as the reference amplitude. The frequency shifts at different loads were measured and normalized with respect to the antenna resonant frequency at zero loading. The actual tensile strains which are applied on the specimen at different loads are also calculated from the bridge output and equation (3.7). Therefore, the experimental relationship between the normalized resonant frequency shift and the mechanical tensile strain on the specimen is achieved. The comparison between the experimental relationship and the theoretical one which shown in the equation (3.1) is represented in Fig. 3.16. The experimental curve displayed a high degree of linearity (coefficient of determination R^2 = 0.9995), but the strain sensitivity of the normalized frequency shift, i.e. the slope of the measured strain-frequency shift relationship, is only -0.717 ppm/με.,which is lower than the theoretical value of -1 ppm/με.. This result is consistent with our previous observations [4]. Two factors could contribute to the lower sensitivity; first, the strain of the specimen may not be transferred to the antenna sensor due to the shear lag effect of

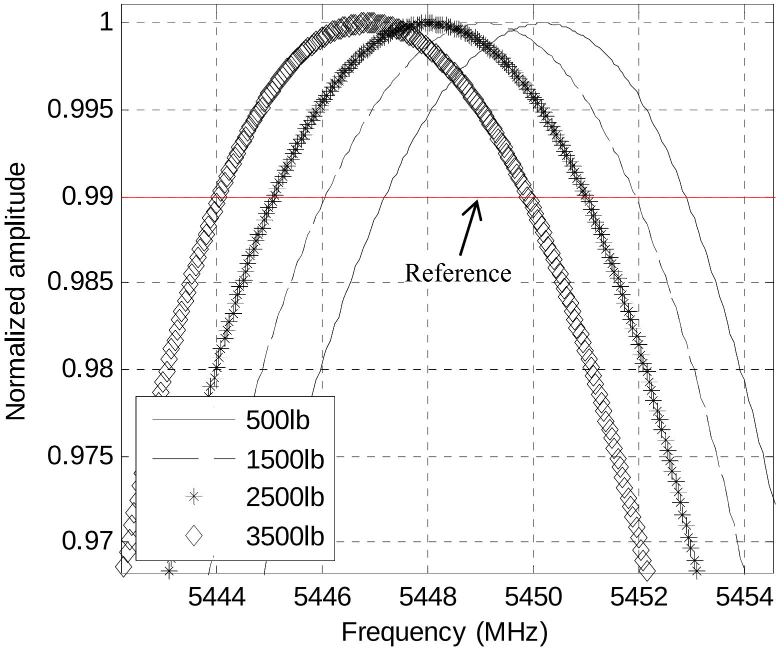

Figure 3.15 Normalized envelopes of demodulated signal at different loads

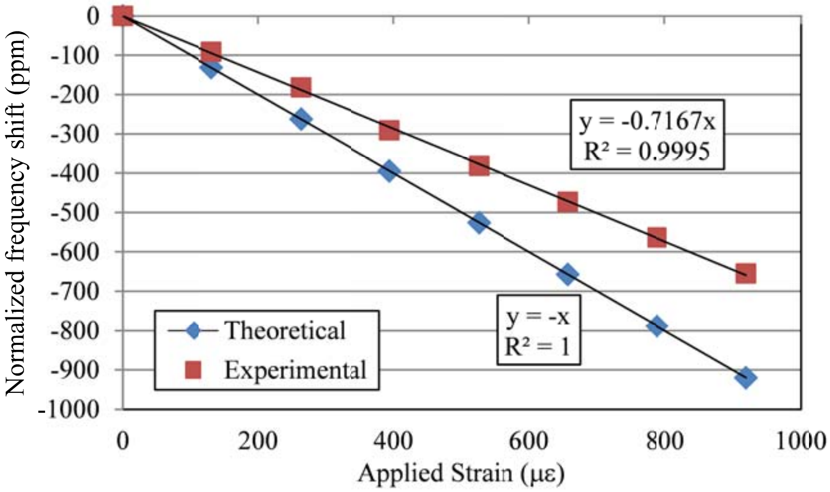

Figure 3.16 Comparison between the measured and theoretical relationship between the normalized antenna resonant frequency shifts and the applied strains

the bonding material; secondly, the dielectric constant of the substrate material may decrease as the test sample is strained. If we use 0.717 ppm/με for the strain sensitivity K_S and calculate the strains from the measured antenna resonant shifts, we found that the normalized measurement errors, i.e. the differences between the strains measured from the antenna sensor and the strain gauge, when normalized with respect to the strain gauge measurements, are within ±1%, as shown in Fig. 3.17. These small measurement errors indicate that we can achieve accurate strain measurements using the antenna sensor as long as the sensitivity of the antenna sensor is calibrated properly.

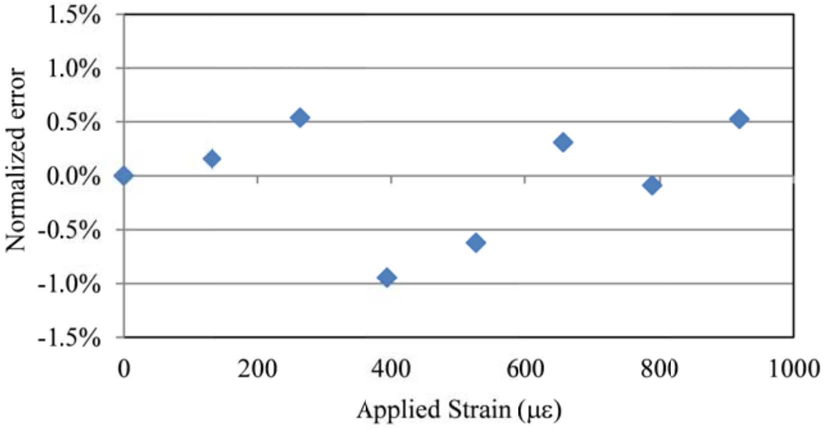

Figure 3.17 Normalized differences between the calibrated antenna sensor readings and strain gauge measurements

3.3.2.2 Dynamic tensile test

To evaluate the dynamic responses of the antenna sensor and the wireless interrogator, the specimen was tested at different vibratory frequencies ranging from 1 Hz to 8 Hz. The time-varying strains measured from the antenna sensor and the strain gauge, at the loading frequencies of 1 Hz and 8 Hz, are plotted in Fig. 3.18 to 3.19, respectively. For a vibratory frequency of 1 Hz, these two sets of measurement matched very well. However, there are observable discrepancies between the measurements when the load frequency was increased to 8 Hz.

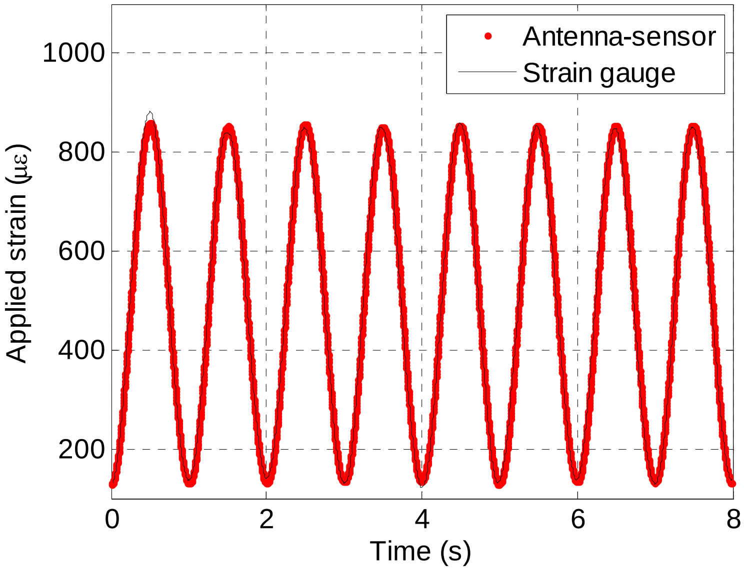

Figure 3.18 Time-domain vibratory strains measured by the antenna-sensor and strain gauge at 1 Hz

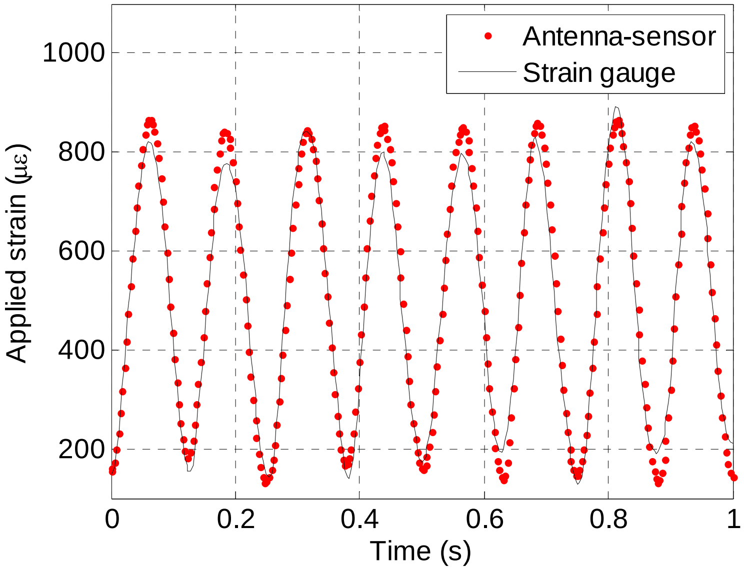

Figure 3.19 Time-domain vibratory strains measured by the antenna-sensor and strain gauge at 8 Hz

We suspect that the increased discrepancies at higher vibratory frequencies are due to the substrate material. Since the substrate material RT/duroid® 5880 is a Polytetrafluoroethylene (PTFE) composite reinforced with glass fibers, it may not have the same dynamic response as the metallic specimen. To test this hypothesis, a strain gauge was bonded on top of the substrate material so that the substrate strains, i.e. the strains measured from the strain gauge bonded on the substrate, can be compared with the specimen strains, i.e. the strains measured from the strain gauge bonded on the specimen. In Table 3.1, the differences between the strains measured on the specimen and from the antenna sensor are given in the second column while the differences between the strains measured on the specimen and the substrate are given in the third column. Both sets of differences were normalized with respect to the maximum specimen strains. For both cases, the normalized differences increase with the vibratory frequency. Therefore, we can conclude that the observed discrepancy between the antenna sensor and strain gauge measurements at high vibratory frequencies are due to the non-ideal dynamic response of the substrate material. In the future, we will evaluate the dynamic responses of other substrate materials in order to identify a substrate material that is more suitable for high frequency dynamic strain measurements.

Table 3.1 Discrepancy analysis at different vibratory frequencies

Loading Freq. (Hz)	$\frac{\lvert\varepsilon_{specimen}-\varepsilon_{antenna}\rvert}{\max(\varepsilon_{specimen})}$	$\frac{\lvert\varepsilon_{specimen}-\varepsilon_{substrate}\rvert}{\max(\varepsilon_{specimen})}$
1	1.19%	1.27%
2	1.68%	1.67%
3	1.90%	1.82%
4	2.40%	1.93%
5	2.51%	2.23%
6	2.72%	2.30%
7	2.96%	2.48%
8	3.70%	2.85%

3.4 Conclusions

The design, implementation, and validation of a novel wireless vibratory strain sensing system are presented. A frequency resolution of 9.26 ppm and an interrogation frequency of up to 320 Hz were achieved. The accuracy of the wireless strain measurement system was validated using in-situ strain gauge measurements. Static test results confirmed that the antenna resonant-frequency shift is a linear function of the strain it experienced while the normalized differences between the calibrated antenna sensor and strain gauge measurements are less than 1%. Real-time measurement of vibratory strains was demonstrated through dynamic tests. We discovered that the differences between the strains measured from the antenna sensor and the strain gauge bonded on the specimen increased with the vibratory frequency. The frequency dependent discrepancies were found to be contributed by the non-ideal dynamic response of the substrate material. In the future, a substrate material with fast dynamic response should be selected to achieve dynamic measurements at higher frequencies.

CHAPTER 4

FAR-FIELD ANTENNA INTERROGATION FOR TEMPERATURE SENSING WITHOUT USING ELECTRONICS

4.1 Operation principle

The block diagram of the proposed interrogation system is shown in Fig. 4.1. The wireless temperature sensing system can be separated into two parts: a wireless interrogator and a passive sensor node. The sensor node circuitry consists of a patch antenna-sensor and a UWB Tx/Rx antenna. Temperature variation changes antenna-sensor's resonant frequency which can be determined by its reflection coefficient. The Tx/Rx antenna is used to receive the wide band interrogation signal from the interrogator and re-broadcast antenna-sensor's reflected signal back to wireless interrogator. To avoid the self-jamming problem [64], a microstrip delay line was used to connect the Tx/Rx antenna and the antenna-sensor. Due to the round-trip transmission on the delay line, the antenna backscattering corresponding to the signal reflected by the antenna sensor has a specific time delay. Therefore, it can be easily distinguished from the background

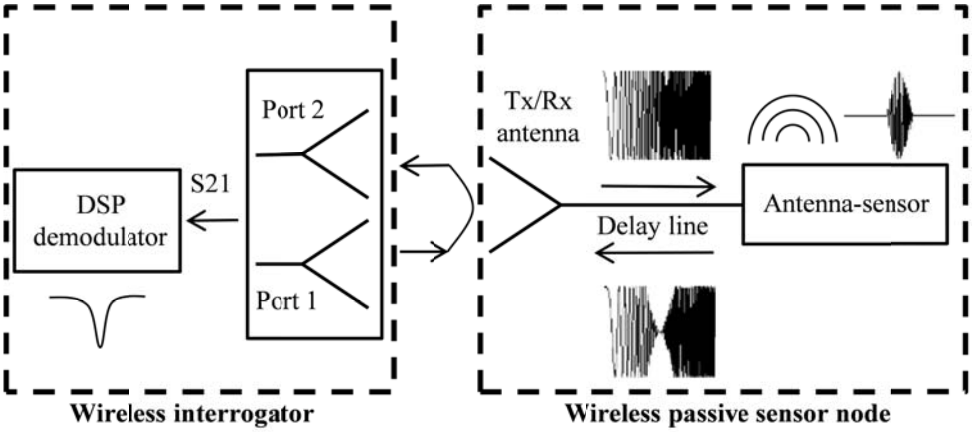

Figure 4.1 Block diagram of the wireless interrogation system without using electronics

clutter in time domain.

The wireless interrogator measures the two-port Scattering (S) parameter, i.e. S21, of the wireless interrogation. Then the S21 parameter is sent to a DSP demodulator to decode the sensing information. First of all, linear chirp interrogation signal was generated and broadcasted to passive sensor node from wireless interrogator. Once the interrogation signal is received by the UWB Tx/Rx antenna it is then transmitted to the antenna-sensor via the microstrip delay line. Upon received by the antenna-sensor, the portion of the FMCW signal that matches the antenna resonant frequency is received and radiated by the antenna-sensor. The remaining interrogation signal is reflected back to Tx/Rx antenna by flowing along the transmission line and re-broadcast back to the interrogator via the Tx/Rx antenna. As such, the reflection coefficient of the antenna-sensor is encoded into the Tx/Rx antenna backscattering. The reflected power of Tx/Rx antenna backscattering received by the interrogator can be calculated using Friis equation:

$$P_r = P_t G_{tt} G_{tr} {G_r}^2 \left(\frac{\lambda}{4\pi d}\right) S_{11} L_d, \tag{4.1}$$

where P_t is the transmit power of the interrogation signal; d is the distance between the wireless interrogator and the Tx/Rx antenna; G_{tt} and G_{tr} are the radiation gains of the transmitter (Tx) receiver (Rx) of the interrogator; respectively; G_r is the radiation gain of the UWB Tx/Rx antenna; λ is the wavelength of the transmission electromagnetic (EM) wave; $S11$ is the reflection coefficient of the antenna-sensor and L_d is the loss caused by the delay line. The minimum detectable power of the wireless interrogator can be expressed as [73]:

$$P_{rmin} = E \cdot B \cdot F \cdot SNR, \tag{4.2}$$

where E is the thermal energy; B is the bandwidth of the receiver; F is the noise figure of the interrogator receiver and SNR is the required signal to noise ratio for this system. Substituting (4.1) into (4.2), the theoretical maximum interrogation distance can be calculated as

$$d_{max} = \frac{\lambda}{4\pi d}\left(\frac{P_t G_{tt} G_{tr} {G_r}^2 S_{11} L_d}{E \cdot B \cdot F \cdot SNR}\right). \tag{4.3}$$

Based on equation (4.3), the maximum interrogation distance is estimated to be 2.25 m assuming a transmitted power of 10 dBm, *E* = 4 x 10-21 J, *B* = 0.8 GHz, *SNR* = 20 dB, *Git* = 12 dBi, *Gir* = 12 dBi, *Gr* = 4 dBi, *Ld* = -1 dB, S11 = -10 dB, *F* = 1 dB, and a wavelength of 0.12 m.

Once Tx/Rx antenna backscattering as well as the background clutter is received by the interrogator the transmission S21 is determined respect to the transmitting power and sent to DSP demodulator. In DSP modulator, TD gate was applied on the reflected mixture signal to separate the 0antenna backscattering from the background clutter. And Fast Fourier Transform (FFT) was used to convert the gated time domain signal into frequency domain to demodulate the reflection coefficient of the antenna-sensor. The real-time resonant frequency of the antenna-sensor can be determined at the frequency which has the lowest reflection coefficient.

4.2 Sensor node implementation

4.2.1 Design of temperature antenna-sensor

Rogers RO3210 [103] was selected as the substrate material for the wireless sensor because of its high thermal coefficient of dielectric constant a_ε, which is -459 ppm/°C in the temperature range from 0°C to 100°C. Compare to a_ε, the thermal expansion coefficient a_T of 13 ppm/°C is much smaller and thus can be ignored in this study. Therefore, equation (6) can be simplified as:

$$\frac{\partial f_{10}}{f_{10}} = -\frac{1}{2}\alpha_\varepsilon \delta T = K_T \delta T. \tag{4.4}$$

Based on equation (4.4), the theoretical temperature sensitivity of the normalized frequency shift K_T is calculated to be 225.9 ppm/°C.

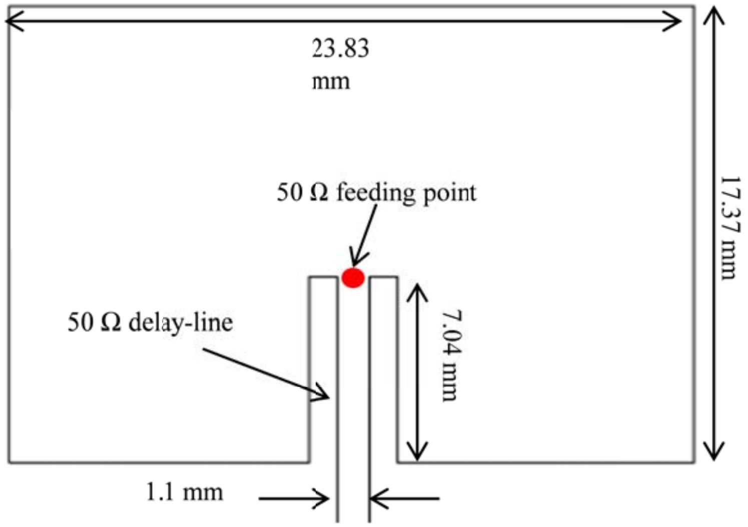

Figure 4.2 Physical dimension and feeding structure of designed microstrip antenna-sensor for temperature sensing

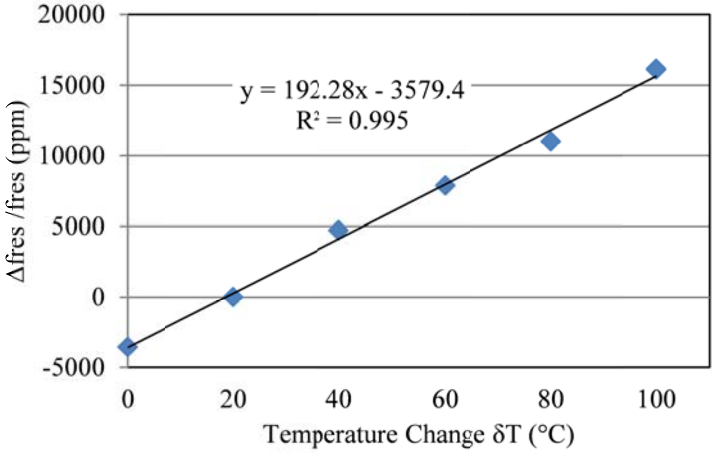

Figure 4.3 Simulated relationship between the antenna-sensor's normalized resonant frequency shift and the temperature change

The radiation patch of an antenna-sensor with a designed frequency of 2.5 GHz is shown in Fig. 4.2. The radiation patch is fed with a 50 Ω microstrip transmission line to excite the fundamental radiation mode along the width direction. In order to obtain a good impedance matching between the transmission line and the radiation patch, the inset fed structure was used. The 50 Ω feeding point was calculated at the position of 7.04 mm above the bottom edge of the radiation patch. The length of the transmission line was selected to be 200 mm to ensure sufficient separation between the Tx/Rx antenna and the antenna sensor. To confirm the antenna design, a 3 Dimension (3D) model of the designed antenna-sensor was developed in High Frequency Structure Simulator (HFSS). For a substrate dielectric constant of 10.8 at room temperature (20°C), every 20°C increase in temperature will reduce the dielectric constant by 10.8 * 459 ppm/°C * 20°C = 0.1. Thus, the substrate dielectric constant of the simulation model was varied from 10.9 to 10.4 with a step of -0.1, which corresponds to temperature changes from 0°C to 100°C. The simulated resonant frequencies are normalized with respect to the frequency at room temperature and are plotted versus the temperature in Fig. 4.3. The simulated curve displays a high degree of linearity (coefficient of determination R^2 = 0.995) and the resulting temperature sensitivity K_T, i.e. the slope of the trend line, is 192.28 ppm/°C which is slightly lower than the value of 225.9 ppm/°C calculated from the transmission line model.

In order to delay the antenna backscattering a 200 mm microstrip delay line was implemented to feed the antenna-sensor. The antenna-sensor and delay line were fabricated using a chemical etching technique, as shown in Fig. 4.4. In order to characterize the time delay caused by the delay line a 50 Ω SMA connector was soldered on the end of delay line. The S11 of the fabricated antenna-sensor was firstly measured using a VNA. Then the S11 parameter was converted into time domain response which is represented in Fig. 4.5. As seen from the figure,

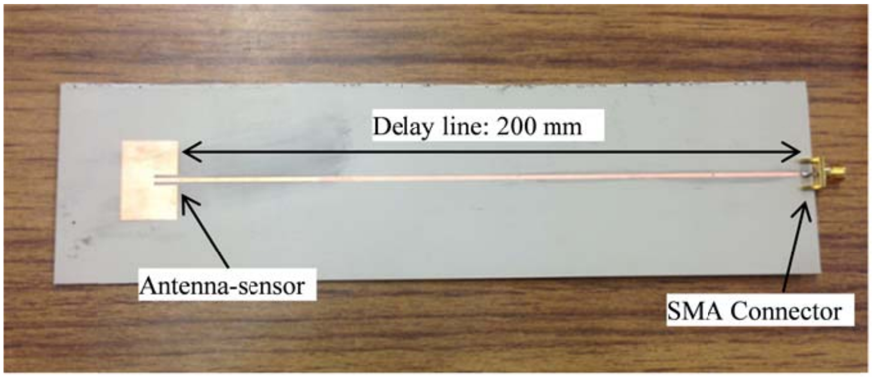

Figure 4.4 Fabricated antenna-senor with microstrip delay line

the reflected signal peak from the antenna-sensor starts at 3.5 ns, which means the round-trip time delay caused by the 200 mm microstrip delay line is 3.5 ns.

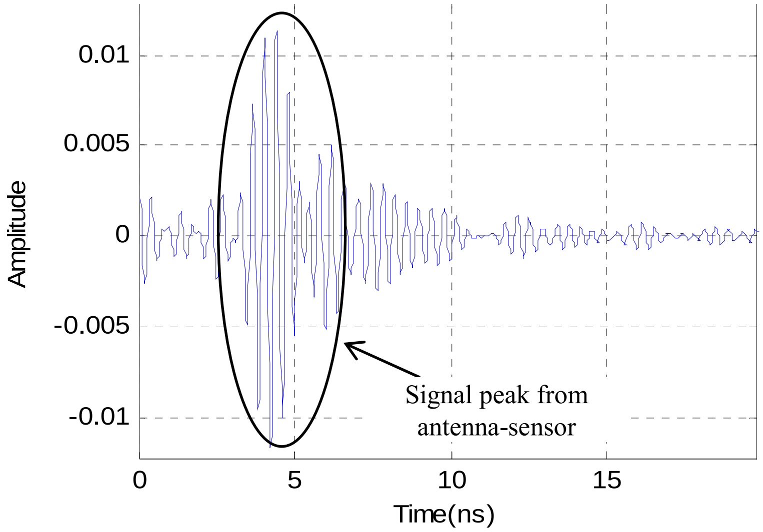

Figure 4.5 Time domain signal converted from measured S11 parameter of the fabricated antenna-sensor with delay line

4.2.2 Design of UWB Tx/Rx microstrip antenna

To implement the entire sensor node on printed circuit boards, the UWB Tx/Rx antenna was developed based on a one-layer substrate patch antenna. The radiation patch is a conventional rectangular patch fed at the bottom edge using a 50 Ω microstrip transmission line, as shown in Fig. 6(a). The ground plane, on the other hand, has a grid pattern with periodically cross gaps that divide the metallic ground into small square patches (see Fig. 6(b)). The patterned ground plane and the rectangular radiation patch can be considered as a type of metamaterial, namely a RIS structure that acts like a parallel LC resonant circuit [94]. The resonant frequency f_{RIS} of the LC circuit can be determined when it has the largest impedance. The impedance of the LC circuit can be expressed by the impedance of the equivalent inductor X_L and capacitor X_C, i.e.

$$Z_{LC} = j\frac{X_L X_C}{X_C - X_L}. \tag{4.5}$$

Where X_L and X_C can be calculated as:

$$X_L = Z_d \tan(kd) \tag{4.6}$$

and

$$X_C = \frac{K\left(\frac{Z_1}{Z_2}\right)}{2\pi K\left(\sqrt{1-\left(\frac{Z_1}{Z_2}\right)^2}\right)(Z_2 - Z_1)}, \tag{4.7}$$

In which, Z_d and k are the wave impedance and the propagation constant of the substrate material, respectively; d is the substrate thickness; Z_1 and Z_2, as shown in Fig. 4.6(b), define the vertical coordinates of the strip edges; the function *K( )* is a complete elliptic integral which is defined in

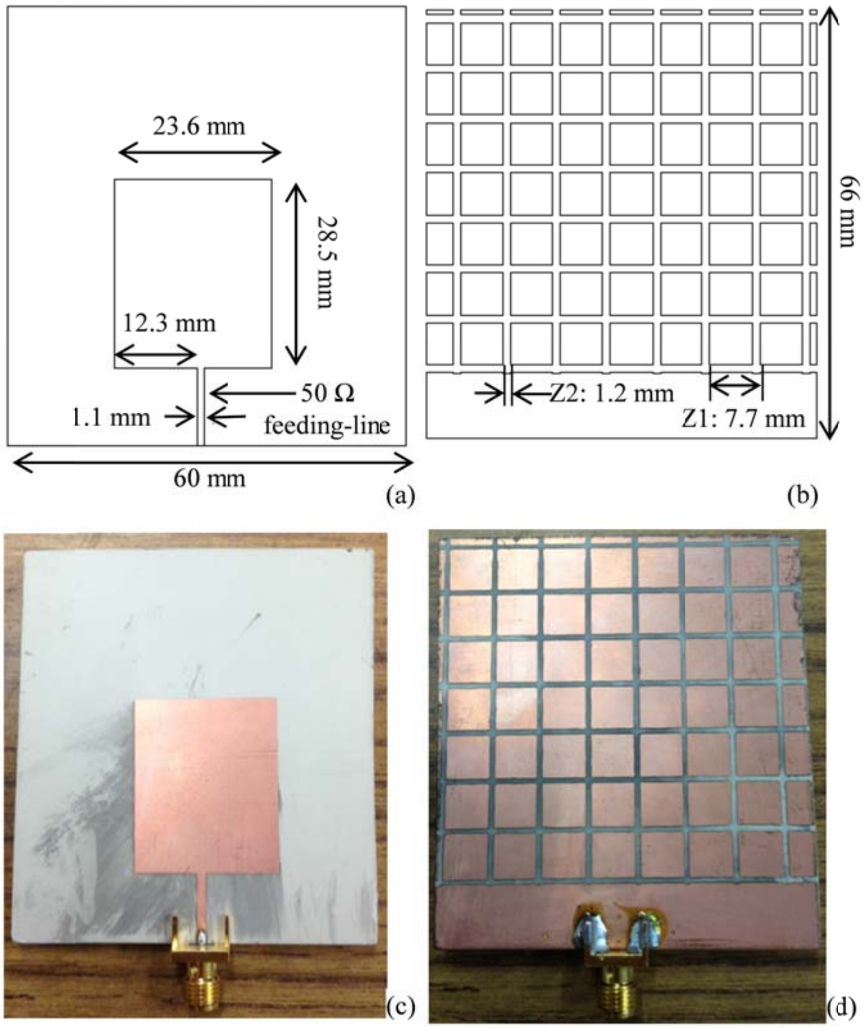

Figure 4.6 UWB Tx/Rx antenna (a) dimension of the front side (b) dimension of the back side (c) front side of the fabricated antenna (d) back side of the fabricated antenna

[93]. The RIS structure is inductive at frequencies below f_{RIS} while the radiation patch becomes capacitive below its resonant frequency f_{patch}. Therefore, by setting f_{RIS} higher than f_{patch}, the magnetic energy stored in the RIS structure can compensate for the electrical energy stored in the near field of the patch antenna, which results in additional resonances at lower frequencies and thus broaden the bandwidth of the antenna [94].

The design of the UWB Tx/Rx antenna started with a conventional patch antenna having a perfect ground plane. The resonant frequency of the conventional patch antenna f_{patch} was chosen to be at 3.8 GHz and the resonant frequency of the RIS structure f_{RIS} was selected as 4.2 GHz, which is slightly higher than f_{patch}. Base on the properties of the substrate material and the selected f_{RIS}, the dimensions of the patterned ground, i.e. $Z1$ and $Z2$, can be calculated to be 1.2 mm and 7.7 mm, respectively, using equation (10), (11) and (12). The pictures of the radiation patch and the patterned ground plane of the UWB Tx/Rx antenna, fabricated using the chemical etching technique, are shown in Fig. 4.6(c) and 4.6(d). The S11 parameter of the fabricated

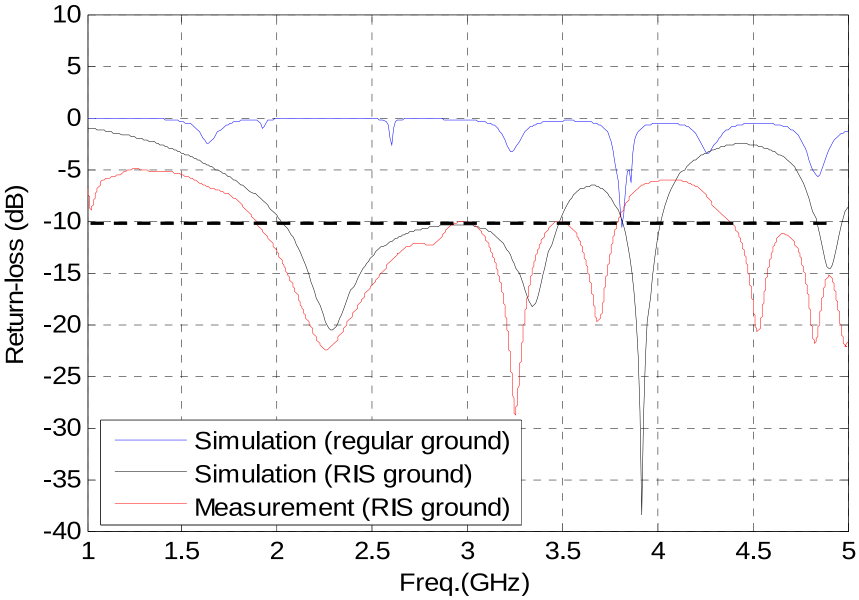

Figure 4.7 Comparison between the simulated and measured S11 of the Tx/Rx antenna

antenna was measured and compared with the simulation results in Fig. 4.7. The bandwidth of the UWB Tx/Rx antenna, determined at the -10 reflection coefficient, is 1.6 GHz (i.e. from 1.9 to 3.5 GHz), which matches with the simulation very well. Compare to the conventional patch antenna, the -10 dB operation bandwidth of the metamaterial antenna increases by more than 100 times. The gain of the Tx/Rx antenna, measured using a two-port transmission test, is shown in Fig. 4.8. The antenna displayed a relatively flat gain, varying from 3.3 to 4 dBi in frequencies ranging from 2.2 GHz to 3 GHz. Due to its flat gain and wide bandwidth, the temperature sensitivity of the Tx/Rx antenna will have very little effect on the measurement of the antenna sensor resonant frequency.

After validating the performances of the antenna sensor and the Tx/Rx antenna separately using SMA connectors, both antennas were integrated on one RO3210 laminate by connecting them using a 200 mm microstrip transmission line. The entire sensor node was fabricated using chemical etching and the pictures of its front and back surfaces are shown in Fig. 4.9.

4.3 Instrumentation and Experimental Setup

The experimental setup for validating temperature sensing capability of the antenna sensor as well as its wireless interrogation is showed in Fig. 4.10. The sensor node package was placed inside an oven so that the environment temperature can be varied. For wireless interrogation, the metal panel of the oven door was removed but the insulation element was kept in place to prevent heat convention and maintain a stable temperature inside the oven. The insulation element of the oven is made of polymer material, which has a dielectric constant similar to air. Therefore, the insulation material will not introduce any changes on the phase or amplitude of the interrogation signal. The wireless interrogator was realized by using a VNA and two interrogation horn antennas. The horn antennas were placed at an interrogation distance of 60 cm in front of the temperature oven facing the Tx/Rx antenna. The S21 parameter between these two interrogation antennas was measured using the VNA, which was connected to the interrogation antennas using co-axial cables. The VNA was calibrated up to the feeding points of the interrogation antennas, which is 30 cm from the aperture of the interrogation antenna. Therefore, the wireless transmission distance between the feeding points of the integration antennas and the antenna sensor is 90 cm.

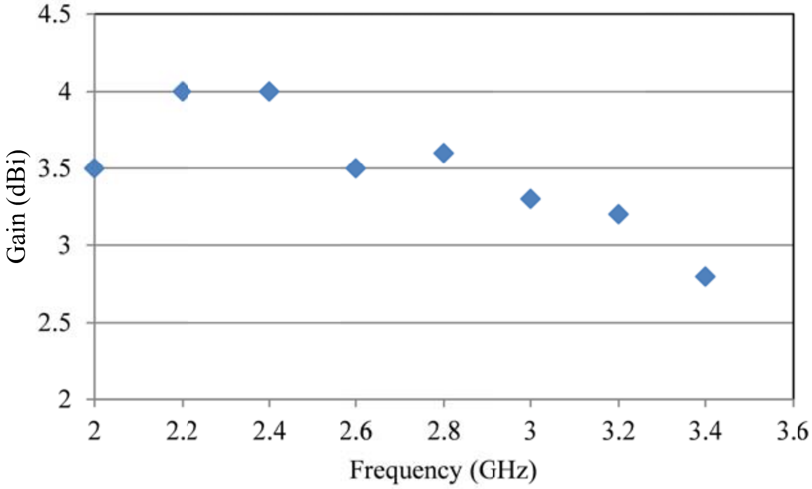

Figure 4.8 Measured radiation gain of the fabricated Tx/Rx antenna

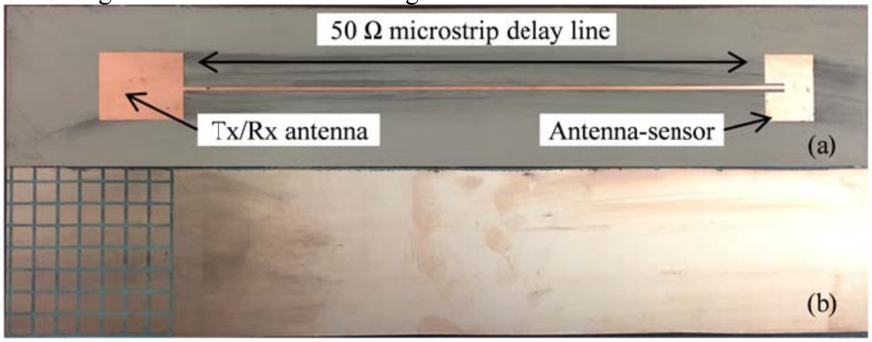

Figure 4.9 Fabricated sensor node package for harsh environment testing (a) front side (b) back side

The sensor package placed near the entrance of the temperature oven is shown in Fig. 4.11. A T-type thermocouple was installed adjacent to the antenna-sensor to obtain the reference temperature of the temperature oven. The thermocouple measurements were acquired using a National Instruments (NI) thermocouple module. Both the NI thermocouple module and the

VNA were connected to a laptop. The communication between the laptop and the VNA was achieved via a wired local-area-network (LAN) connection, while the communication between the computer and the NI module was achieved via Universal Serial Bus (USB) connection. A LabVIEW program was developed to control the VNA and the NI module. The VNA was programmed to acquire the S21 parameters with a frequency resolution of 200 kHz over a specified frequency range of 2.2 to 3 GHz using a 10 dbm interrogation power. The S21 parameters were recorded every 2.3 seconds. At the meantime, the thermocouple readings were

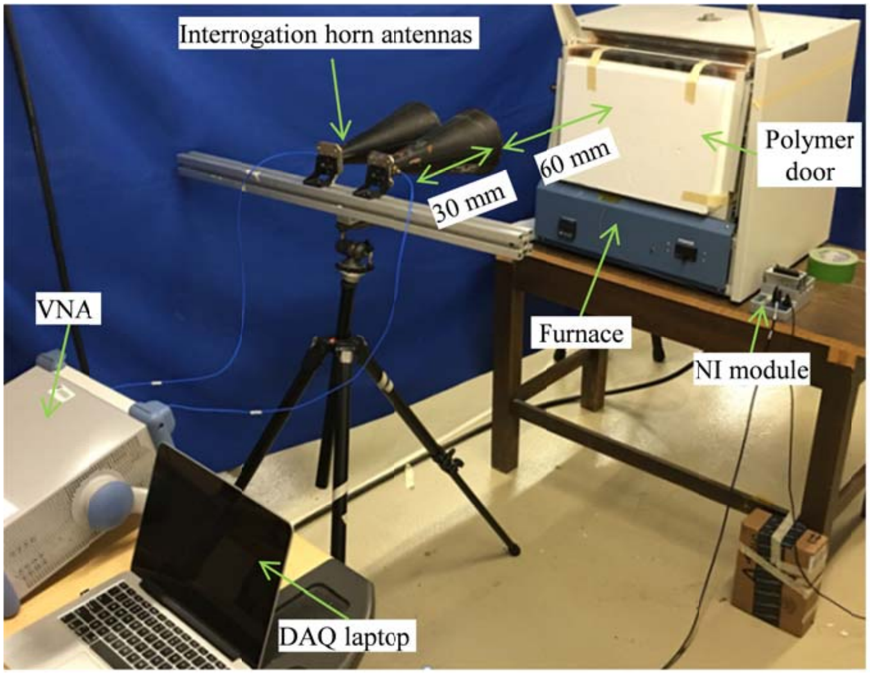

Figure 4.10 Experimental setup for temperature testing

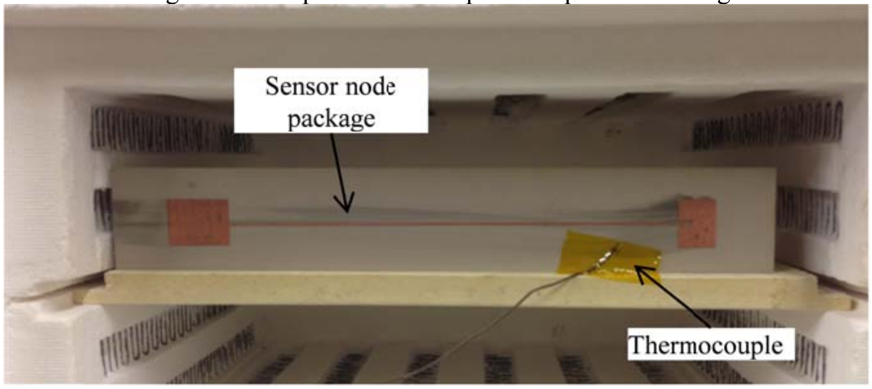

Figure 4.11 Wireless sensor node placed at the entrance of the oven

recorded every 0.1 second. Both recorded data were time stamped for easily correlation between the temperature readings and the extracted resonant frequency from the S21 parameters.

4.4 Digital signal processing

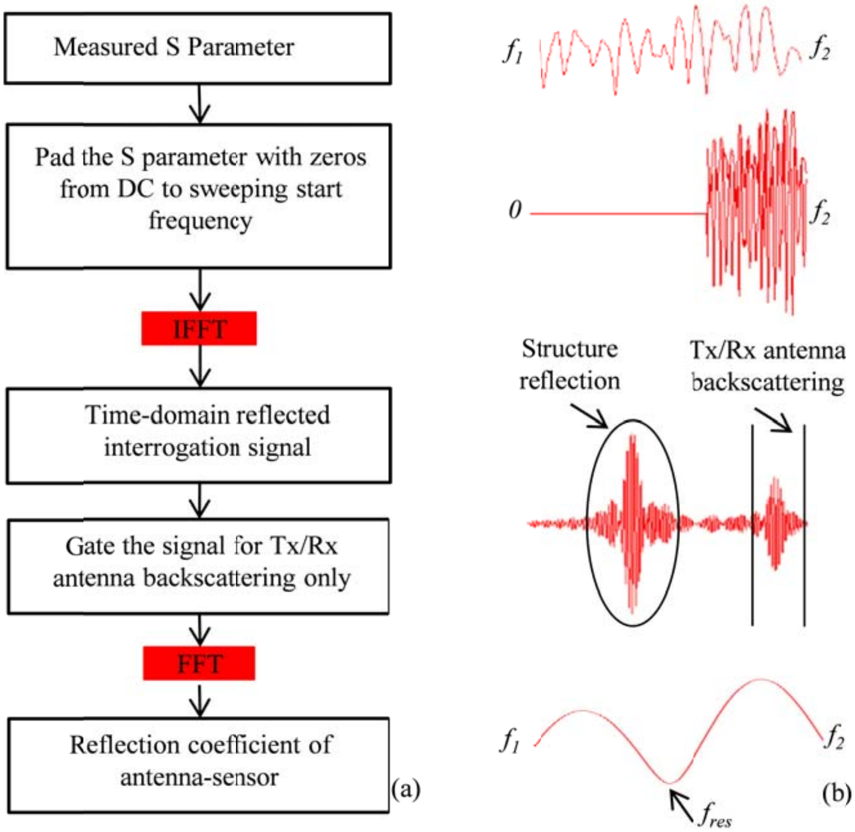

Figure 4.12 Digital signal processing algorithm; (a) flow diagram; (b) signals corresponding to processing blocks

A DSP algorithm was developed to extract the resonant frequency of the antenna-sensor from the measured S21 parameters. The flow chart of the DSP algorithm is shown in Fig. 4.12(a) and the signals corresponding to each block are shown sequentially in Fig. 4.12(b). First, the acquired S21 parameter, which has a frequency range from f_1 to f_2, is zero padded from the Direct Current (DC) frequency (i.e. 0 Hz) to f_2. The zero-padded S parameter is then converted to a time-domain signal using Inverse Fast Fourier Transform (IFFT) [104]. As shown in Fig. 4.12(b), the resulting time-domain signal displays two major wave packets that correspond to the structural backscattering and the antenna sensor backscattering. Both wave packets have small side lobes, which can be reduced by windowing before the IFFT. Nonetheless, the presents of the side lobes will not have an effect on determining the frequency of the antenna sensor backscattering. Even though the signals backscattered by the Tx/Rx antenna and the surrounding structures usually have the largest amplitude, they appear at a different time span from that of the antenna sensor backscattering. Therefore, a gating window can be applied to the time domain signal to extract the antenna sensor signal. Since the time-gated signal will only contain signals that are reflected at or near the feeding point of the antenna sensor, the time gating process also eliminate reflections at other locations along the transmission delay line due to temperature gradient, etc. Subsequently, the gated signal is converted back to the frequency domain using Fast Fourier Transform (FFT) and the resonant frequency of the antenna-sensor can be determined as the frequency at which the reflection coefficient has the lowest value.

4.5 Results and discussions

The time-domain representation of a typical S21 parameter is shown in Fig. 4.13. Time “0” corresponds to the feeding point of the transmitting interrogation signal. The first wave packet arrives at around 2 ns, which corresponding to a round trip distance of 0.3 m. This distance coincides with the distance between the feeding point of the interrogation antenna and the antenna aperture. Therefore, we can conclude that this wave packet is due to the coupling between the two interrogation horn antennas. The second wave package arrives at around 6 ns, which corresponds to a round-trip distance of 0.9 m and thus is the structure mode backscattering generated by the antenna sensor and the temperature oven. Due to the time delay introduced by the microstrip delay line, the antenna mode backscattering occurs at 3.5 ns after the structure mode backscattering. We can then extract the antenna mode backscattering by time gating the transmission signal from 9.5 ns to 12.5 ns. The resonant frequency of the antenna sensor can then be determined by performing FFT of the time-gated signal. The frequency spectra of the time gated signal at different temperatures are shown in Fig. 4.14. The resonant frequency of the

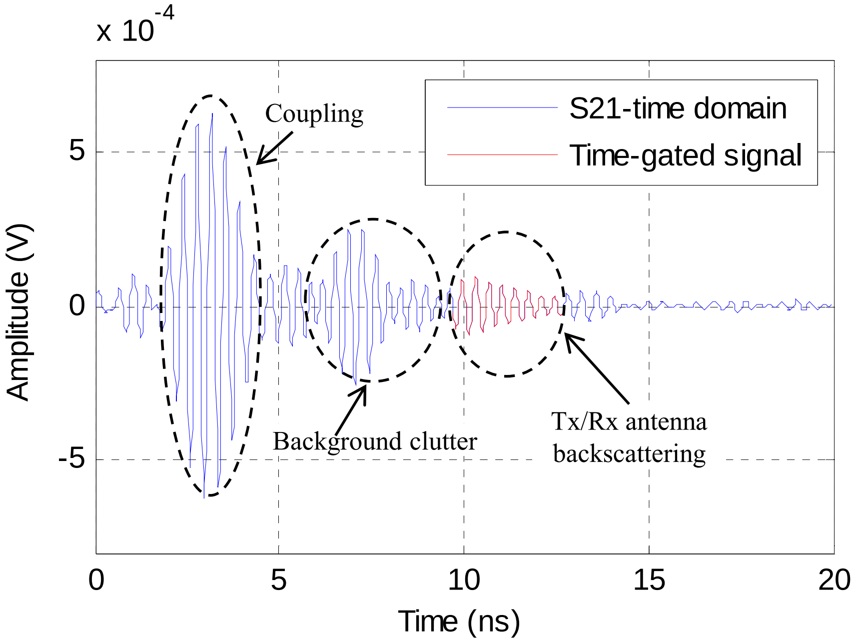

Figure 4.13 Time domain reflection signal converted from measured S21 parameter at room temperature

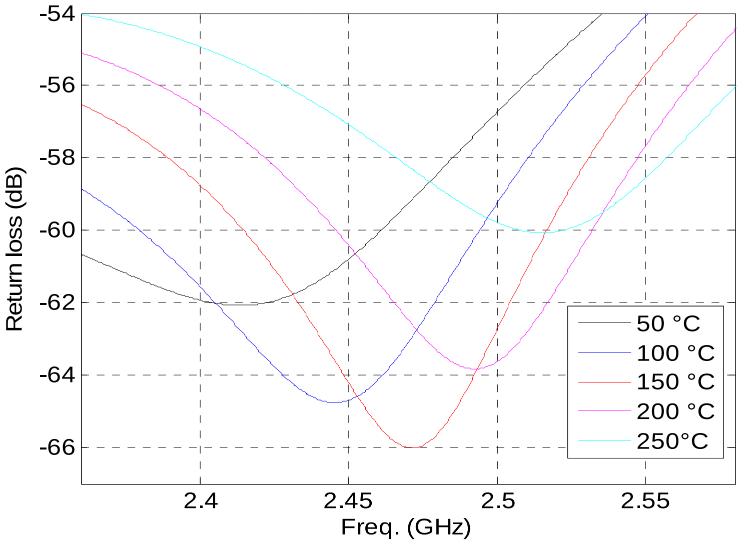

Figure 4.14 FFT of gated TD signal at different temperatures

antenna sensor is determined as the frequencies at which the frequency spectrum has the lowest amplitude. The frequency shifts at different temperatures were normalized with respect to the resonant frequency of the antenna-sensor at room temperature. The measured normalized frequency shifts are plotted versus the temperature change measured from the thermocouple in Fig. 4.15. The measurement data display a high degree of linearity (R^2 = 0.9972). The slope of the trend line is 195.13 ppm/°C, which is slightly higher than the theoretical K_T value of 192.45 ppm/°C. The normalized deviation between the simulated and experimental K_T is 1.39%.

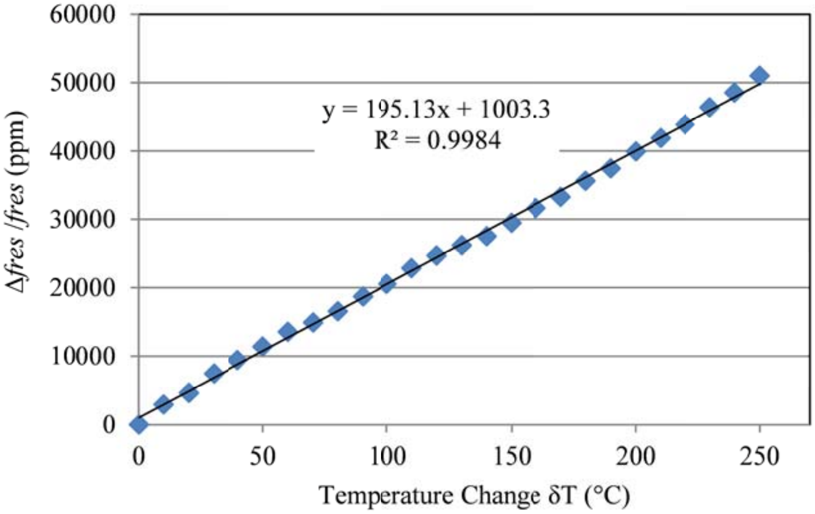

Figure 4.15 Measured relationship between the antenna-sensor's normalized resonant frequency shift and the temperature change from temperature testing

4.6 Conclusions

In this study, a wireless temperature sensor consisting of only microstrip circuit elements and without any electronic components is demonstrated. A wireless interrogation system that is capable of acquire sensing signal in the far field of the wireless antenna sensor was developed. Temperature testing (up to 280 °C) was conducted to validate the functionalities of the wireless sensor and interrogation system. The measured temperature sensitivity is 195.13 ppm/°C which matched very well with the theoretical value. In future works, a low-cost FMCW-based wireless interrogator will be investigated to reduce the cost of the interrogator and to increase the interrogation speed. In addition, we will explore high-temperature PCB material to increase the operation temperature of the wireless antenna sensor.

CHAPTER 5

WIRELESS ANTENNA SENSOR INTERROGATION USING FMCW BASED TIME-GATING TECHNIQUE

5.1 Operation principle

In this study, we continue integrate the time-gating technique and the FMCW radar method to realize FMCW time-gating interrogation technique which can be used in high-temperature harsh environment. The advantage of such an approach is that the time gating is performed in the frequency domain instead of the time domain. As a result, substantial improvement on the interrogation speed can be achieved. Non-electronics sensor node package mentioned in CHAPTER 4 will still be used in this research. Thus, the proposed high-speed interrogation mechanism can be implemented in high-temperature environment. Compare to the setup in CHAPTER 4, the VNA interrogator was replaced by the proposed FMCW interrogator, the block diagram of the system setup is shown in Fig. 5.1. In the FMCW interrogator, a delay line was added to increase the beat frequency of backscattered sensing signal. Thus, after bandpass filter,

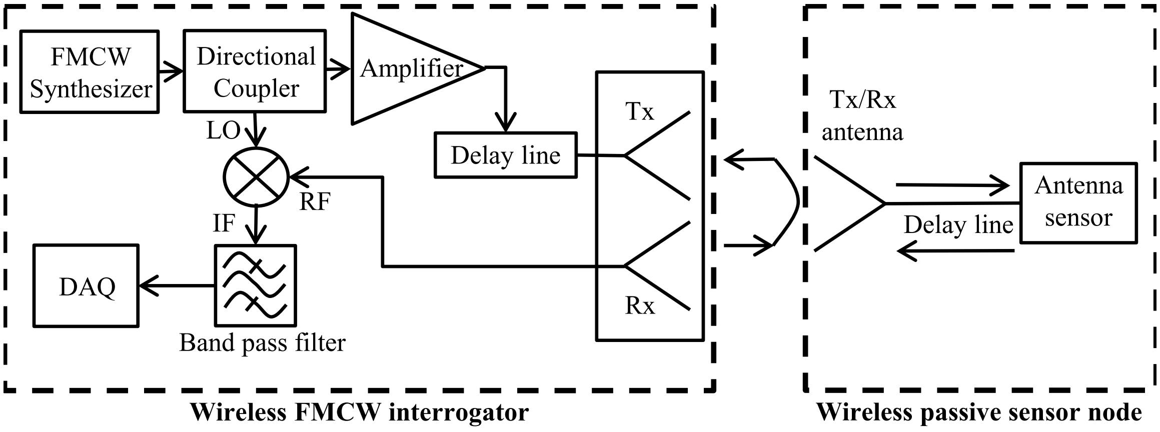

Figure 5.1 Proposed antenna-sensor wireless interrogation using FMCW time-gating technique

the frequency of the sensing signal will be much higher than the sweeping frequency of the FMCW interrogation signal so that a stable amplitude envelop of the sensing signal can be achieved in a single FMCW period.

The FMCW synthesizer generates a linear chirp signal whose frequency is a linear function of time. As a result, the frequencies of the backscattered sensing signal as well as the background clutter also vary linearly with time (see Fig. 5.2). At a given time t, the frequency generated by the FMCW synthesizer is f_1. The signal was sent to the Local Oscillation (LO) port of the down-convention mixer through a directional coupler. In the meantime, the interrogation Rx antenna receives the background clutter (f_2) as well as the backscattered sensing signal (f_3) and the mixture signal will be sent to Radio Frequency (RF) port of the mixer. The frequency of the reflected background clutter f_2 can be calculated based on the time delay caused by the delay line d_{delay} and the wireless transmission d_{trans}:

$$f_2 = f_1 - \frac{W}{T}\left(d_{delay} + d_{trans}\right), \tag{5.1}$$

where W is the frequency sweeping range of the FMCW signal; T is the period of FMCW signal. Since there is a microstrip delay line implemented in the sensor package, the backscattered sensing signal has an additional delay d_{sensor} thus, at time t, the frequency of reflected sensing signal f_3 can be expressed as:

$$f_3 = f_1 - \frac{W}{T}\left(d_{delay} + d_{trans} + d_{sensor}\right). \tag{5.2}$$

Therefore, after down-conversion, the output of mixer IF port has two beat frequency components: (f_2 - f_1) for background structure backscattering and (f_3 - f_1) for sensor node component. Due to the time delay d_{sensor}, the sensor node signal is separated from the background structure backscattering in frequency domain and the frequency difference between those two backscattering can be calculated as:

$$(f_3 - f_1) - (f_2 - f_1) = f_3 - f_2 = \frac{W \cdot d_{sensor}}{T}. \tag{5.3}$$

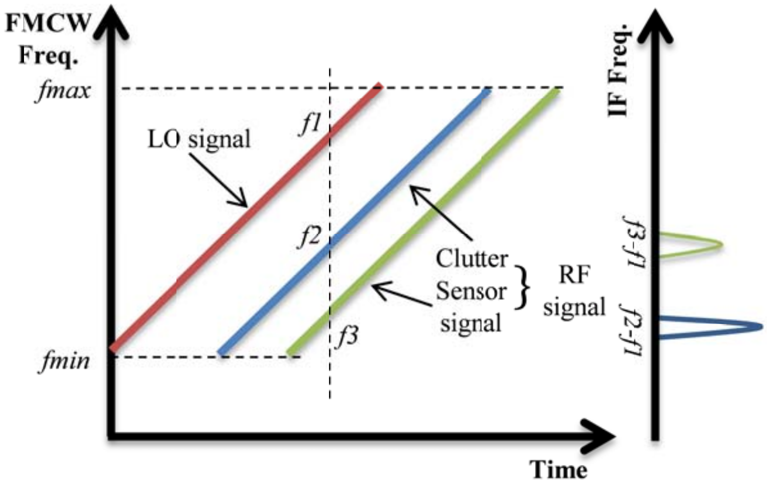

Figure 5.2 Separation of the sensing signal and background clutter in frequency domain

Then mixer Intermediate Frequency (IF) output signal will be sent to a band pass filter to filter the background clutter and maintain the frequency component of sensor signal. Filtering the IF signal using a band-pass filter therefore is equivalent to time-gating the sensor signal. Performing the time-gating in frequency domain using analog devices will drastically enhance the interrogation speed and frequency resolution of the wireless receiver. Due to the sweeping of the interrogation frequency using the FMCW synthesizer, the power of the IF sensing signal is directly proportional to the reflection coefficient S_{11} of the antenna sensor and it can be calculated based on equation (4.1):

$$P_S = P_t G_{tt} G_{tr} {G_r}^2 \left(\frac{\lambda}{4\pi d}\right) S_{11} L_d L_{mixer}, \tag{5.4}$$

where L_{mixer} is the down-conversion loss caused by the RF mixer. After filtering, the sensor node signal will be sent to a Data Acquisition (DAQ) system which has an input impedance of 50 Ω and the real-time amplitude collected by the DAQ system is expressed as:

$$A_s = \sqrt{50 \cdot P_s} = \sqrt{50 \cdot P_t G_{tt} G_{tr} {G_r}^2 \left(\frac{\lambda}{4\pi d}\right) S_{11} L_d L_{mixer}}. \tag{5.5}$$

In each FMCW period, when the interrogation frequency matches with the resonant frequency of the antenna-sensor the antenna-sensor will have the lowest reflection coefficient S_{11} thus the corresponding real-time amplitude A_S collected by the DAQ system will be the smallest. Therefore, by correlating the lowest amplitude of collected signal in each FMCW period to the corresponding FMCW interrogation frequency, the resonant frequency of the antenna-sensor can be determined. The flow chart of the DSP algorithm in DAQ system is shown in Fig. 5.3(a) and the signals corresponding to each block are shown sequentially in Fig. 5.3(b). First of all, the envelope of input signal was detected for each FMCW period. This envelope stands for the real-time reflection coefficient of the antenna-sensor in the FMCW frequency sweeping range, which is from f_{min} to f_{max}. Then resonant frequency of the antenna-sensor can be determined at the frequency which has the lowest reflection coefficient. The resonant frequency of antenna-sensor will be updated every FMCW period. Therefore, if we increase the FMCW frequency high-speed wireless interrogation of antenna-sensor can be achieved. Temperature testing will be performed to validate the proposed wireless interrogation mechanism.

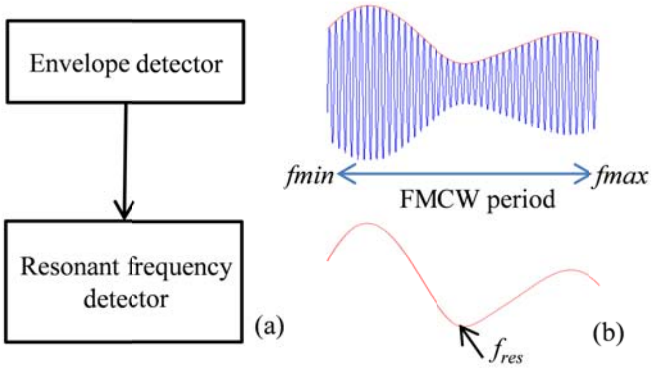

Figure 5.3 Illustration of digital signal processing algorithm in DAQ (a) flow diagram; (b) signals corresponding to processing blocks

5.2 Hardware implementation of FMCW interrogator

The hardware setup of the FMCW interrogator is shown in Fig. 5.4. The FMCW synthesizer is realized by a periodic saw-tooth wave generator and a VCO circuit. The calibrated relationship between the VCO input voltage and output RF frequency is represented in Fig. 5.5. As can be seen in the figure, the measured voltage-frequency curve has a good linearity (coefficient of determination $R^2 = 0.9998$). Based on the calibration results, in order to sweep the FMCW frequency from 2.2 to 3 GHz, the amplitude of the input saw-tooth wave should vary from 2.8 to 8.8 V. The frequency of the saw-tooth wave was set as 1 kHz. Therefore, in this study, the interrogation FMCW signal sweeps from 2.2 to 3 GHz with an interrogation rate of 1 kHz. The signal was then sent to a RF amplifier with a 25 dB gain. Consider the typical output power from VCO is 5 dBm, the amplitude of FMCW signal is around 30 dBm after amplification. The amplified signal was sent to the delay line through a directional coupler.

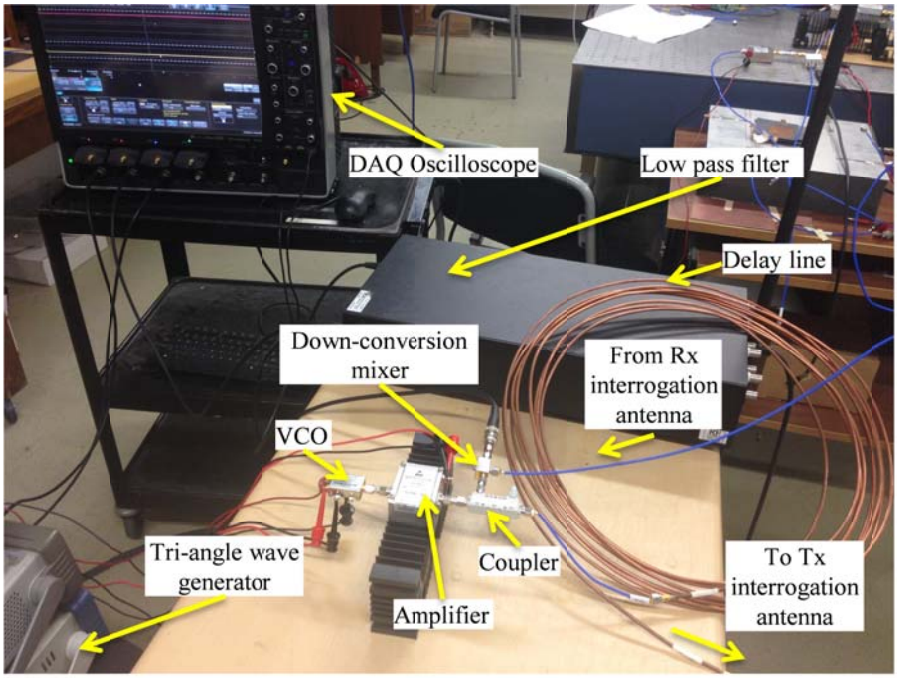

Figure 5.4 Hardware implementation of FMCW interrogator

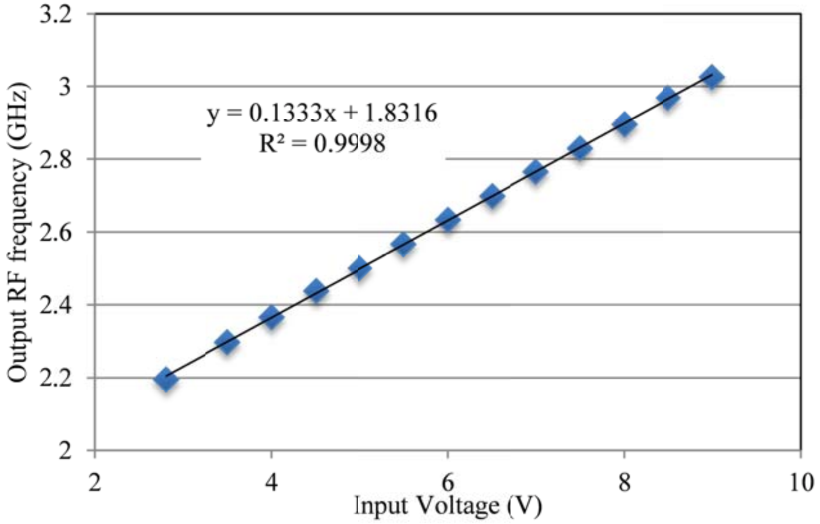

Figure 5.5 Calibrated relationship between VCO input voltage and output frequency

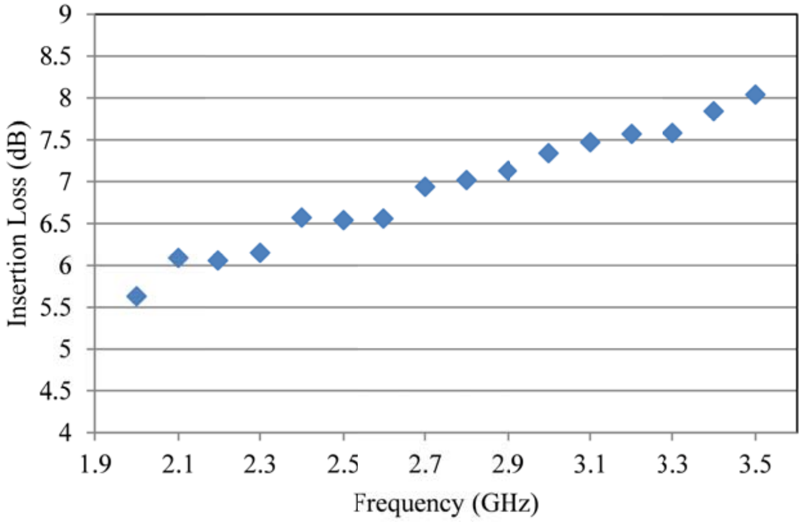

Figure 5.6 Calibrated insertion loss caused by the delay line at different frequencies

The insertion loss of the delay line was calibrated. The experimental insertion loss values of the delay line at different frequencies are shown in Fig. 5.5. The calibrated insertion loss increases as frequency increasing. In the FMCW frequency range, i.e. 2.2 to 3 GHz, the insertion loss caused by the delay line starts from 6 to 7.3 dB. Another important property of delay line is the time delay it causes. The experimental time delay is measured using the S parameter measurement and time-domain analysis which are mentioned in Chapter 4. The block diagrams of the testing setup are shown in the Fig. 5.7. As shown in Fig. 5.7, a VNA was used as the wireless interrogator and two 24-inch coaxial cable was selected to connect the VNA ports and

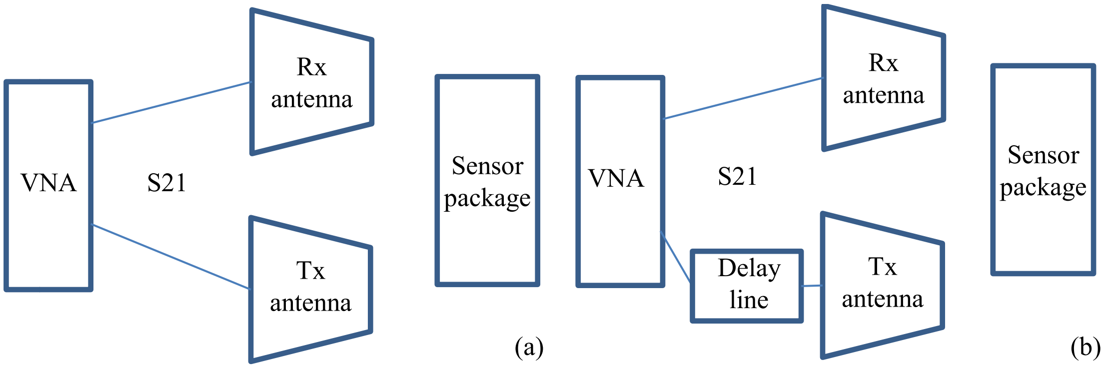

Figure 5.7 Block diagram of the system setups for delay line time delay calibration (a) without delay line (b) with delay line

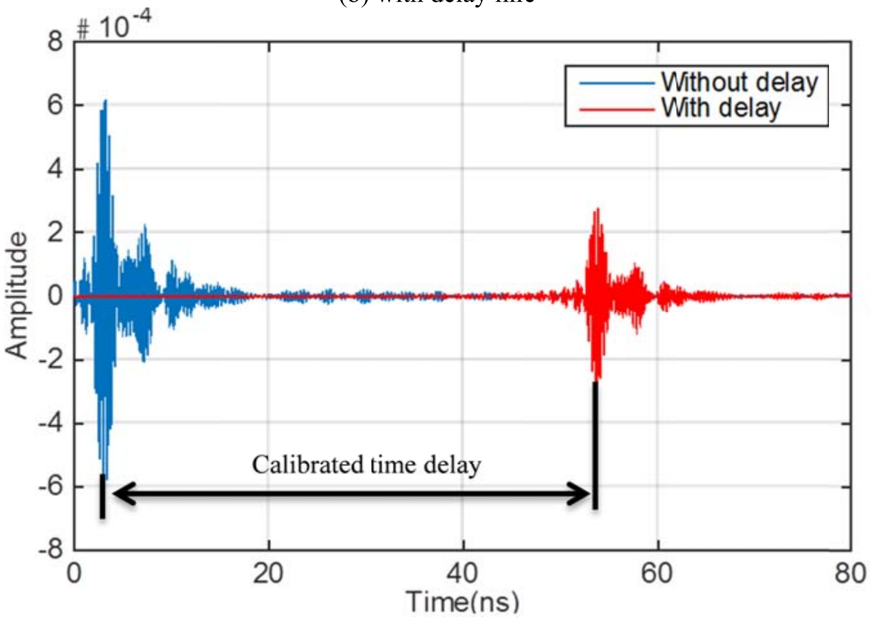

Figure 5.8 Time domain signals converted from S21 parameters

interrogation Tx and Rx antennas. VNA was calibrated to the end of the coaxial cable so that the propagation of EM wave in coaxial cable will not consider as part of the wireless communication. S21 of the wireless interrogation without delay line was firstly recorded. Another S21 was measured by adding the delay line. Both S21 parameters were converted into time domain signal using the DSP algorithm which is presented in Fig. 4.10. The converted time-domain signals are represented in Fig. 5.7. The experimental time delay of the delay line can be measured as the arrival time difference between the first peaks of those two time domain signals. From the figure, the experimental time delay of the delay line was measured as 50.8 ns.

The reflected signal received from the Rx interrogation antenna was applied to a down-conversion mixer. The mixer IF output contains two frequency components: background structure backscattering (f_2 - f_1) and sensor node backscattering (f_2 - f_1). A low-pass filter was implemented right after the IF port in order to filter the high frequency noise of the mixer output. The filtered signal was collected by a high speed oscilloscope. The sampling rate of the oscilloscope was set as 2.5 MHz. Since the period of FMCW interrogation signal is 1 ms, every FMCW period 2500 sample points were collected. Consider the interrogation frequency sweeps from 2.2 to 3 GHz each FMCW period, the frequency detection resolution can be calculated as 0.8 GHz/2500 = 320 kHz for this sensing system. In order get stable signal, an average of 20 FMCW period signals were calculated as the signal of single FMCW period. Since the interrogation rate of the FMCW signal is 1 kHz the interrogation rate of this sensing system is 1 kHz/20 = 50 Hz.

A DSP algorithm was developed in Matlab to process the data recorded from the oscilloscope. The purpose of this data process is to separate the sensor node backscattering from background structure backscattering for each interrogation period and determine the resonant frequency from the frequency spectrum of the sensor node signal. The flow chart of the DSP algorithm is shown in Fig. 5.9(a) and the signals corresponding to each block are shown sequentially in Fig. 5.9(b). First of all, the acquired signal is segmented into data arrays with each array corresponding to one FMCW period. Both time-domain and frequency spectrum of the collected signal are shown in Fig 5.9(b). In the frequency spectrum, there are three main frequency components which stand for coupling between the interrogation antennas, background clutter and sensor node signal, respectively. A Butterworth digital band-pass filter was then applied on the data array to separate the sensor node signal from the other two. After filtering we get the time domain signal for the sensor node and the time scale is converted to the frequency scale based on the time-frequency relationship of the FMCW synthesizer. As mentioned in equation 5.5, the amplitude of this filtered signal is proportional to the reflection coefficient of the antenna-sensor. Therefore, an envelope detection algorithm is then applied on the filtered sensor signal to track its amplitude in the FMCW sweeping frequency range. Finally, the resonant frequency of the antenna-sensor can be determined at the frequency which has the lowest amplitude in the envelope curve.

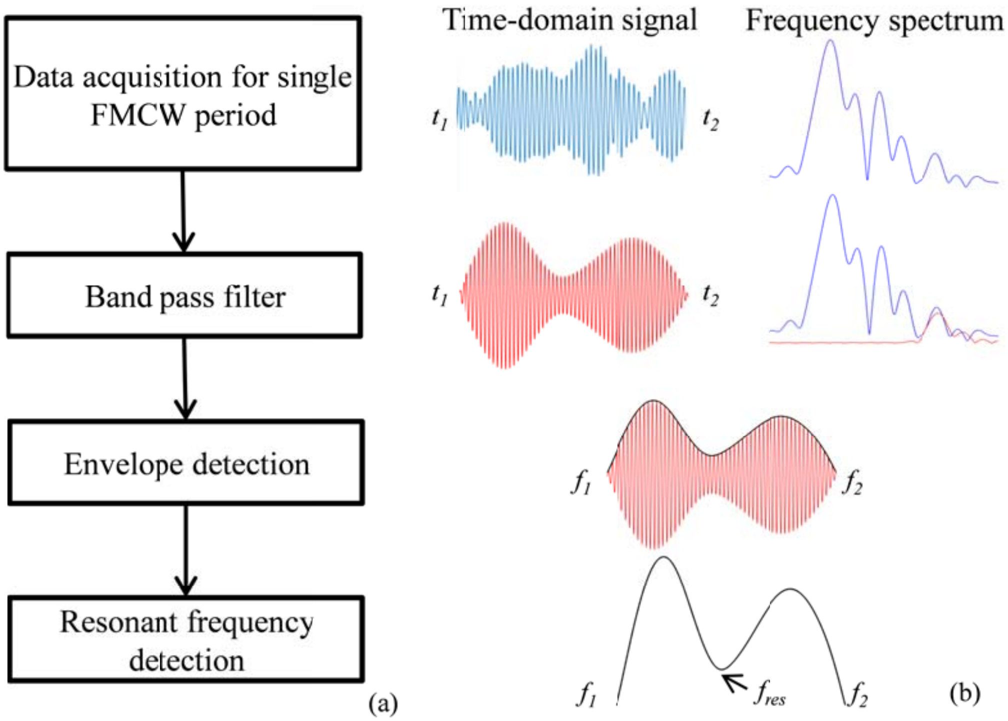

Figure 5.9 Illustration of Matlab DSP algorithm; (a) flow diagram; (b) signals corresponding to processing blocks

5.3 Temperature validation testing and data analysis

A temperature testing was performed to validate the accuracy of the FMCW interrogation system. The experimental setup, including the interrogation horn antennas, the sensor package and the temperature oven was the same as that in Chapter 4. The wireless interrogation distance was set as 60 cm and the testing temperature starts form 25 to 170 °C. For comparison, VNA interrogator was firstly used to monitor the frequency variation of the antenna-sensor at different testing temperatures. The block diagram of the experimental setup is shown in Fig 5.10.

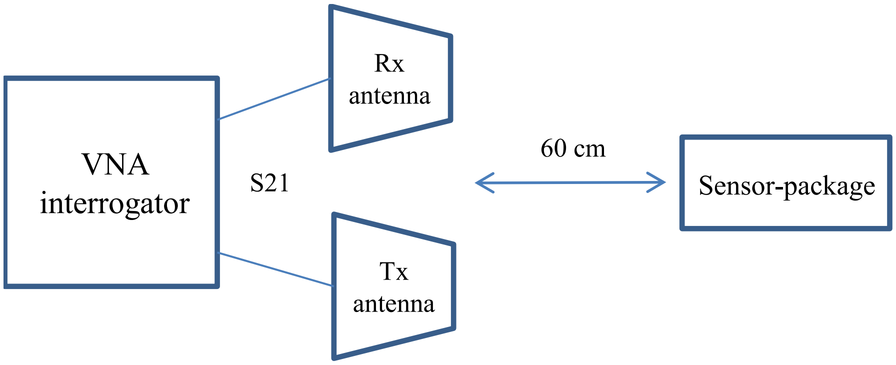

Figure 5.10 Block diagram of the wireless temperature sensing system using VNA interrogator

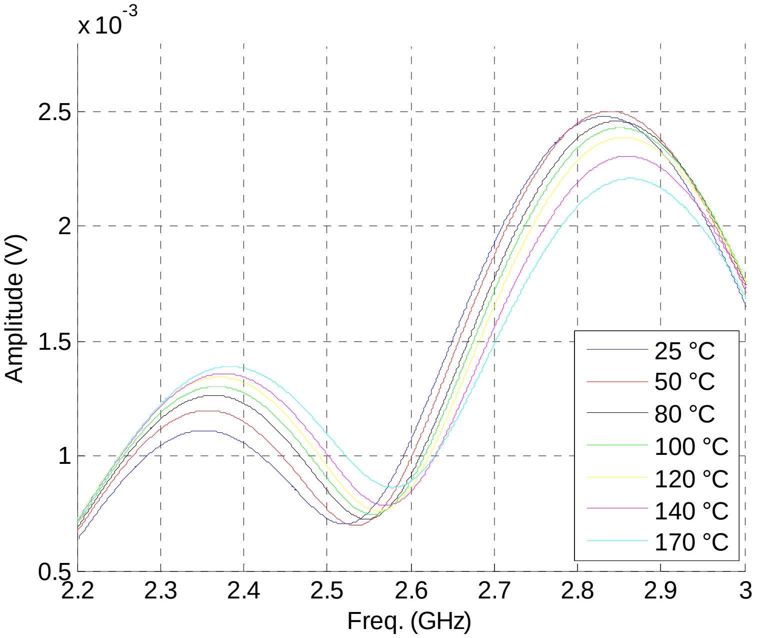

Figure 5.11 Measured antenna-sensor's reflection coefficients at different temperatures using VNA interrogator

DSP algorithm which is shown in Fig.4.10 was applied on the recorded S21 parameters to calculate the reflected amplitude of the antenna-sensor. The measured antenna-sensor's reflected amplitude curves at different temperatures are represented in Fig. 5.11. From the figure we can see that the resonant frequency of the antenna-sensor increases as temperature increasing, which matches the results from Chapter 4.

The FMCW interrogator was then implemented to replace the VNA. The testing setup is shown in Fig. 5.12. The mixer output of a single FMCW period was collected by the oscilloscope at a rate of 50 Hz and processed off-line using the DSP algorithm shown in Fig. 5.9. The reflected amplitudes of the antenna-sensor at different temperatures were calculated and some of them are plotted in Fig. 5.13. The resonant frequencies can be determined at the frequency which has the lowest amplitude in the amplitude curve. The measured frequency

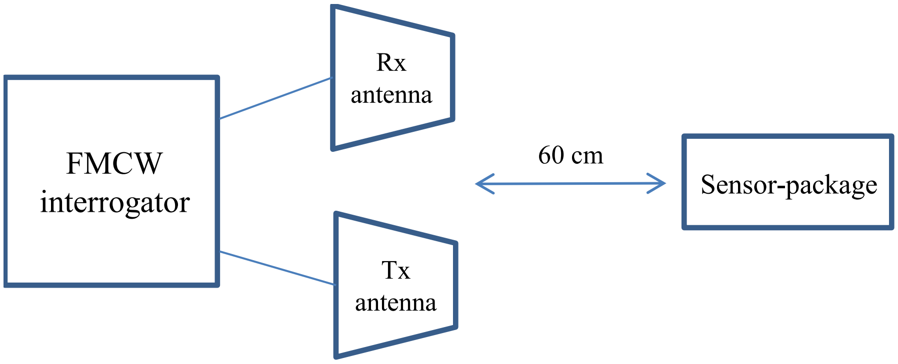

Figure 5.12 Block diagram of the wireless temperature sensing system using FMCW interrogator

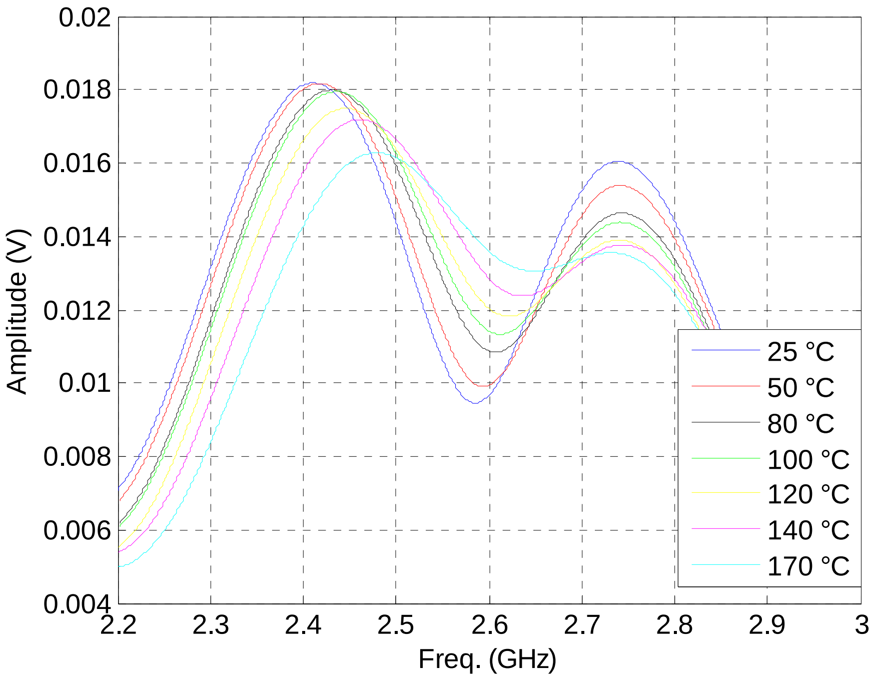

Figure 5.13 Measured antenna-sensor's reflection coefficients at different temperatures using FMCW interrogator

increases as temperature increasing as well, which matches the results from VNA interrogator. Since the insertion loss of the delay line goes higher at larger frequency, the reflected amplitude at high frequency is lower than that at low frequency when using VNA interrogator.

The frequency shifts at different temperatures were normalized with respect to the resonant frequency of the antenna-sensor at room temperature (25 °C). The measured relationship between the normalized frequency shifts and the temperature change is plotted in Fig. 5.13 and the reference relationship which is measured using VNA interrogator is also represented in the same figure. The curve measured using FMCW interrogator has a good linearity and the temperature detection resolution (the slope of the curve) matches with that of the reference curve very well. The normalized discrepancy of the detection resolution is only 3%, which proves the accuracy of the FMCW interrogator.

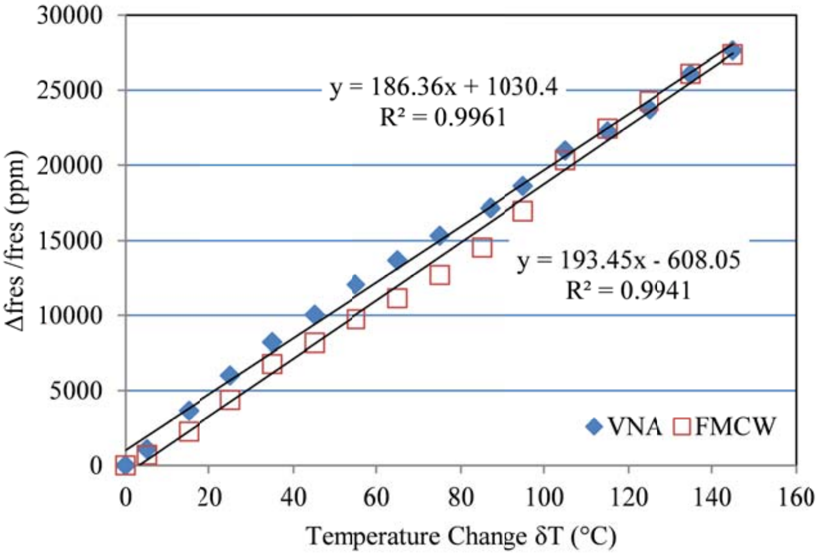

Figure 5.14 Comparison between the frequency shift-temperature variation measured from VNA interrogator and FMCW interrogator

5.4 Conclusions

In this study, a high-speed wireless interrogation technique for antenna-sensor in harsh environment was presented. FMCW based antenna-sensor interrogator was developed to perform the time-gating perform in the frequency domain instead of the time domain. Therefore, a higher interrogation rate of 50 Hz was achieved in the proposed temperature sensing system. The accuracy of the FMCW interrogator was also validated during the temperature testing. The experimental relationship between antenna-sensor's frequency shift and temperature variation matches very well with the reference one which is measured by VNA interrogator. The normalized discrepancy is only 3%. In the future, a portable PCB FMCW synthesizer will be developed to reduce the size and power consumption of the FMCW interrogator and multiple antenna-sensors will be implemented to achieve wireless sensing network.

CHAPTER 6

A COMPACT FMCW INTERROGATOR OF MICROSTRIP ANTENNA FOR FOOT PRESSURE SENSING

6.1 Operation Principle

6.1.1 Patch antenna based pressure sensor

The pressure sensor consists of a microstrip patch antenna and a metal reflection plate, as shown in Fig 6.1. The reflection plate is placed above the antenna. The RF signal that is radiated by the antenna will be partially reflected back by the metal plate and this reflected signal will slightly change the resonant frequency of the antenna sensor. The relative distance between the patch and the metal plate determines the amount of the reflected signal. Therefore, the microstrip antenna will have different resonant frequencies when the reflection plate is at different heights. A pressure applied on the reflection plate will change its relative distance to the antenna sensor.

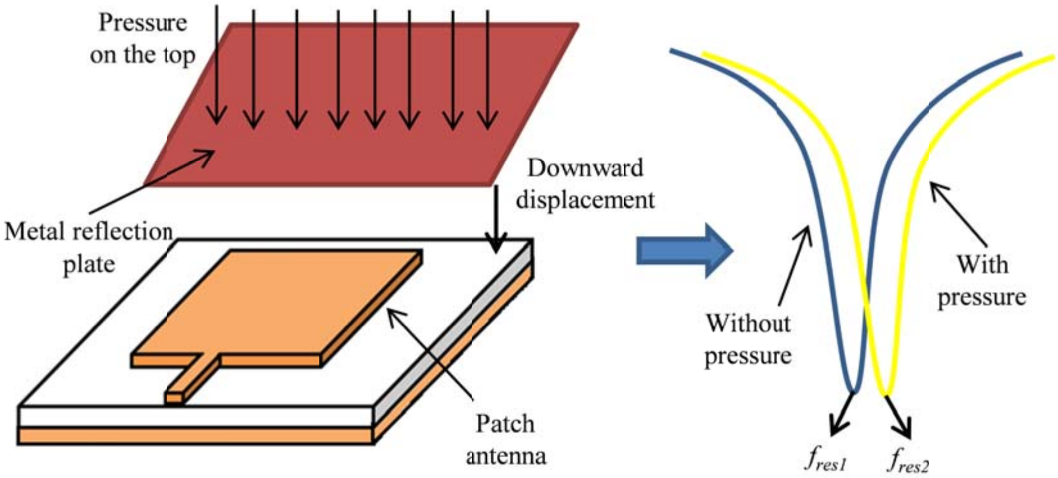

Figure 6.1 Antenna-based pressure sensor demonstration

By detecting the shift of the antenna's resonant frequency, the change of the relative distance can be determined. Furthermore, the metal reflection plate also isolates the interference from its upper side, thus makes the sensor more stable.

6.1.2 Portable FMCW interrogation circuit

In order to detect the frequency shift of the antenna pressure sensor a FMCW interrogation circuit was designed. The circuit consists of a PCB-based FMCW synthesizer, a RF circulator and a RF power detector. The diagram of the interrogation circuit is shown in Figure 6.2. First of all, linear chip signal which has a carrier frequency sweeping from f_1 to f_2 is generated by the FMCW synthesizer. The signal is sent to port 1 of the circulator and interrogates the antenna senor though port 2. Then the antenna reflected signal goes from port 2 to port 3 as the input of the RF power detector. The power detector converts the received RF power into DC voltage. The lower power it receives the high DC voltage it generates. If the interrogation frequency matches antenna's resonant frequency the reflected RF signal will has the smallest power. Thus, the RF power detector outputs the largest DC voltage. So by detecting the position of power detector's peak output the resonant frequency of the antenna sensor can be achieved.

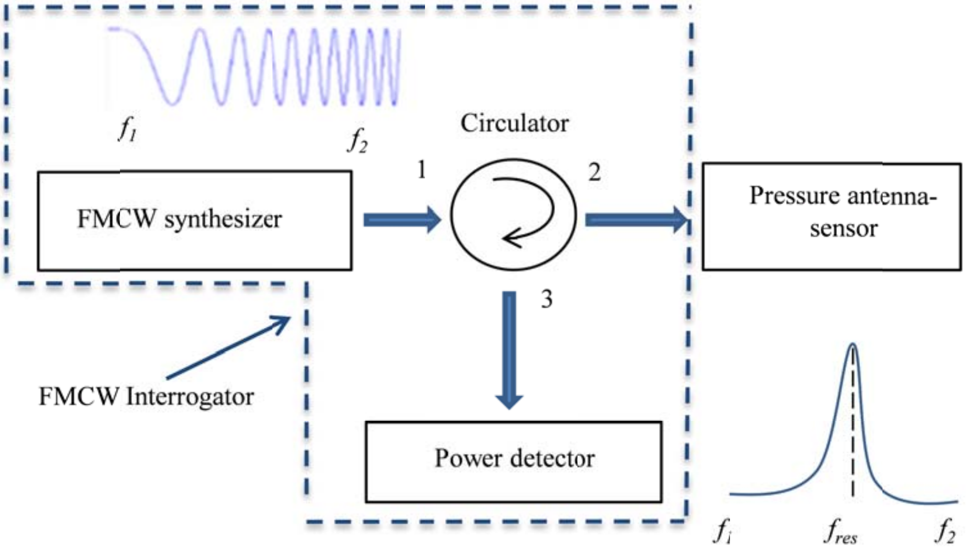

Figure 6.2 Block diagram of the FMCW interrogation circuit

6.2 Design of pressure sensor node

6.2.1 Sensor packaging and deformation characterization

A testing apparatus was designed for the integration of the antenna sensor and the reflection plate. The 3D model of the sensor package that was created using SolidWorks is shown in Fig. 6.3(a). The sensor package consists of two plates separated using soft spacers. There are two wide slots in the plates so that the reflection plate and antenna can be held in place; the upper slot is for the metal reflection plate and the lower slot is for the antenna sensor. The sensor package was fabricated by a 3D printer and a picture of the fabricated sensor is shown in Fig. 6.3(b). The

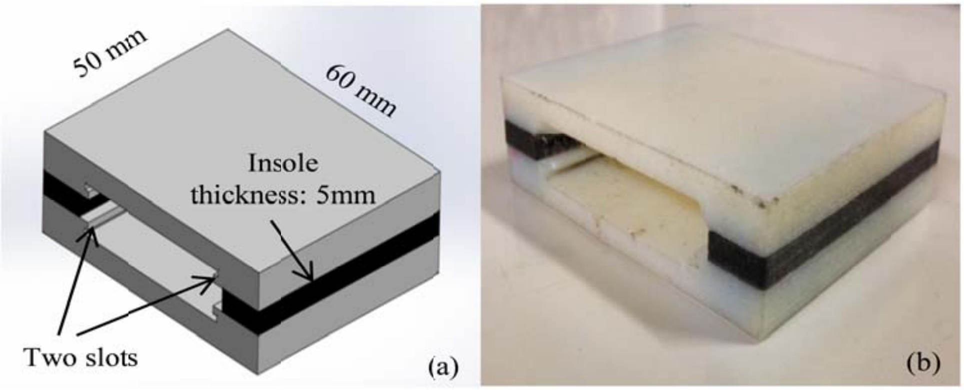

Figure 6.3 Antenna pressure sensor package: (a) SolidWorks model (b) fabricated sensor package

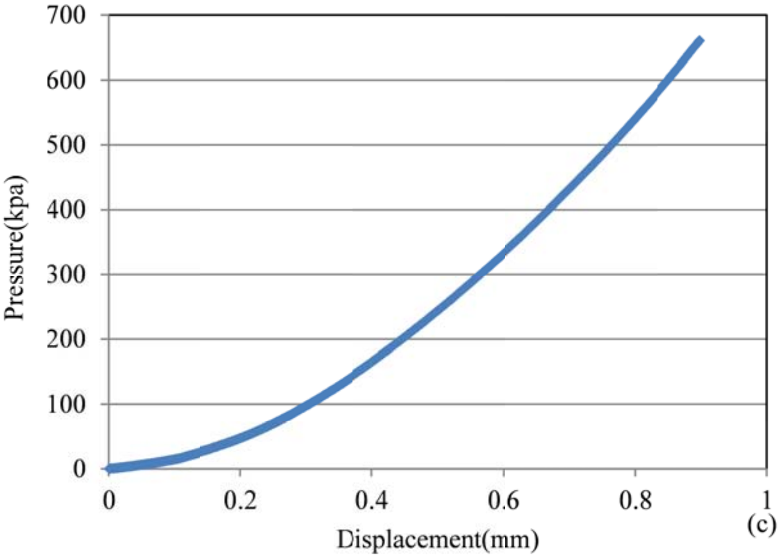

Figure 6.4 Measured relationship between the applied pressure and the displacement of the up-cover

upper and lower plates (white) are made of Acrylonitrile Butadiene Styrene (ABS) plastic and the spacers (black) are made of normal shoe insole material. In order to characterize the relationship between the applied pressures and the displacements of the reflection plate, pressure tests were performed using a MTS compression machine. During the tests, the applied pressure was varied from 0 kPa to 720 kPa at an increment of 1.5 kPa. The experimental pressure-displacement is plotted in Fig 6.4. Since the spacer material is a plastic foam material, it displaced a slightly nonlinear pressure-displacement relationship. As long as this relationship is repeatable, we can use the calibrated relationship to determine the applied pressure from the displacement measurements.

6.2.2 Antenna design and HFSS simulation

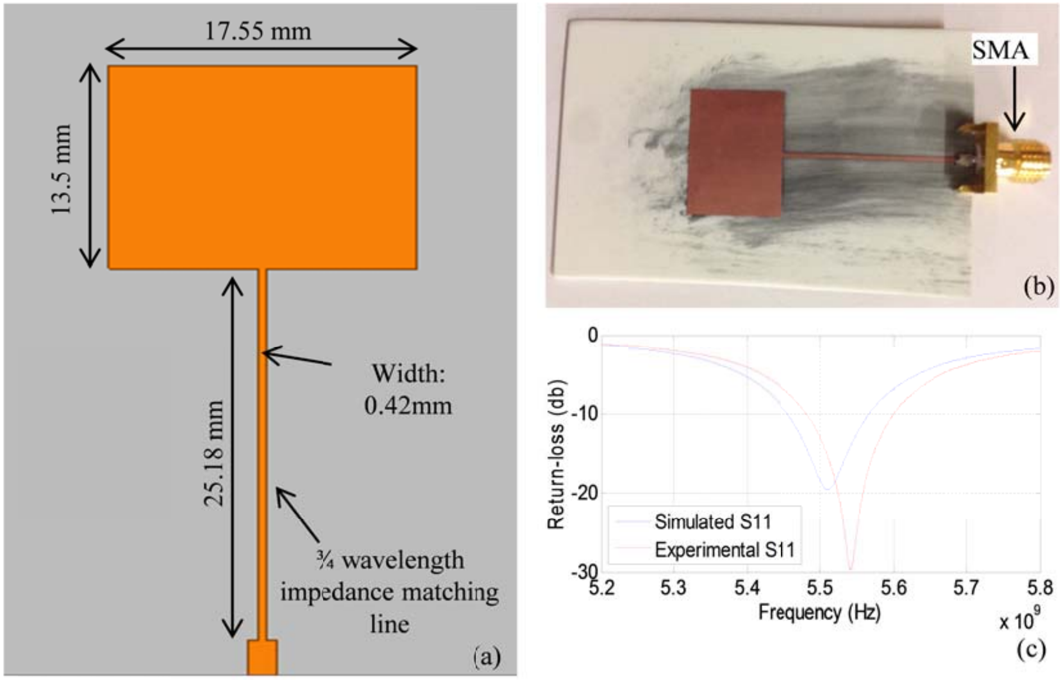

Figure 6.5 Antenna design and simulation: (a) physical dimensions (b) fabricated antenna (c) comparison between the experimental and simulated return-loss of the designed patch antenna

A microstrip patch antenna was designed using a high frequency laminate (RO4350b). The physical dimension of the antenna is shown in Fig 6.5(a). A ¾ wavelength transmission line was added to match the impedance of antenna's feeding point at 50 Ω. The microstrip antenna was then fabricated using chemical etching technology and a 50 Ω SMA connector was soldered onto its feeding point, as shown in Fig 6.5(b). The return-loss S11 curve of the fabricated antenna was measured using a VNA. The experimental S11 curve was compared with the one simulated using an EM software-HFSS and both curves are demonstrated in Fig 6.5(c). The measured S11 curve indicates that the patch antenna has a distinguished resonant frequency at 5.54 GHz which matches with the simulated frequency, i.e. 5.51 GHz, very well.

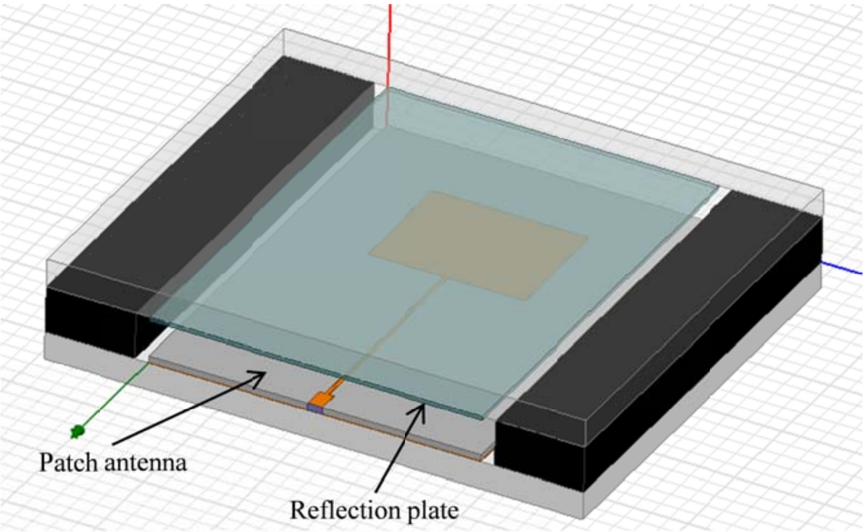

Figure 6.6 3-D simulation model of the pressure sensor

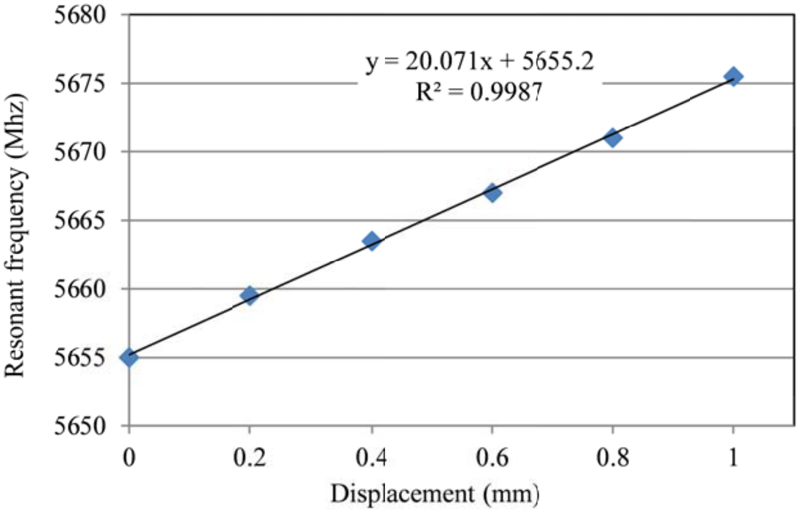

Figure 6.7 Simulated relationship between the resonant frequency shift of the antenna-sensor and the displacement of the mental reflector

A 3D model of the pressure antenna senor was also created in HFSS, as shown in Fig. 6.6. The antenna testing apparatus was also created using the simulation software, keeping the same dimensions as previously mentioned; the material of the reflection plate is aluminum. In order to understand how the plate's downward displacement affects the resonant frequency of the antenna, simulations were conducted by varying the downward displacement of the reflection plate and the upper plastic cover from 0 mm to 1 mm with a step of 0.2 mm. The S11 curve was calculated at every displacement and the resonant frequencies were determined from the simulated S11 curves. As shown in Fig. 6.7, the antenna resonant frequency increases with the displacement increases. Furthermore, the relationship between the variation of the resonant frequency and the downward displacement have a very good linearity (coefficient of the determination $R^2 = 0.9987$).

6.3 Design of the FMCW synthesizer

In the FMCW generator, a periodic linear chirp is implemented by using a VCO controlled by a periodic triangle signal. As such, the instantaneous frequency of the chirp is swept through a frequency range continuously during each period of the triangle signal. The sweep rate and the frequency range of the chirp signal can be adjusted by changing the frequency and the amplitude of the triangle control signal. First of all, a triangle wave generator was designed and simulated by using a 555 timer (TLC555). The SPICE simulation schematic of the generator is shown in Fig. 6.8 and the simulation results are demonstrated in Fig. 6.8(a). The simulated saw tooth wave varies from 1.32 V to 3.3 V at a frequency of 52.8 Hz. Then the circuit was fabricated and the output was measured to validate the simulation results. As shown in Fig 6.8(c), the measured saw tooth wave is from 1.4V to 3.6 V with a frequency of 52.1 Hz, which matches the simulated curve very well. The slight discrepancy is due to the tolerance of the lump components.

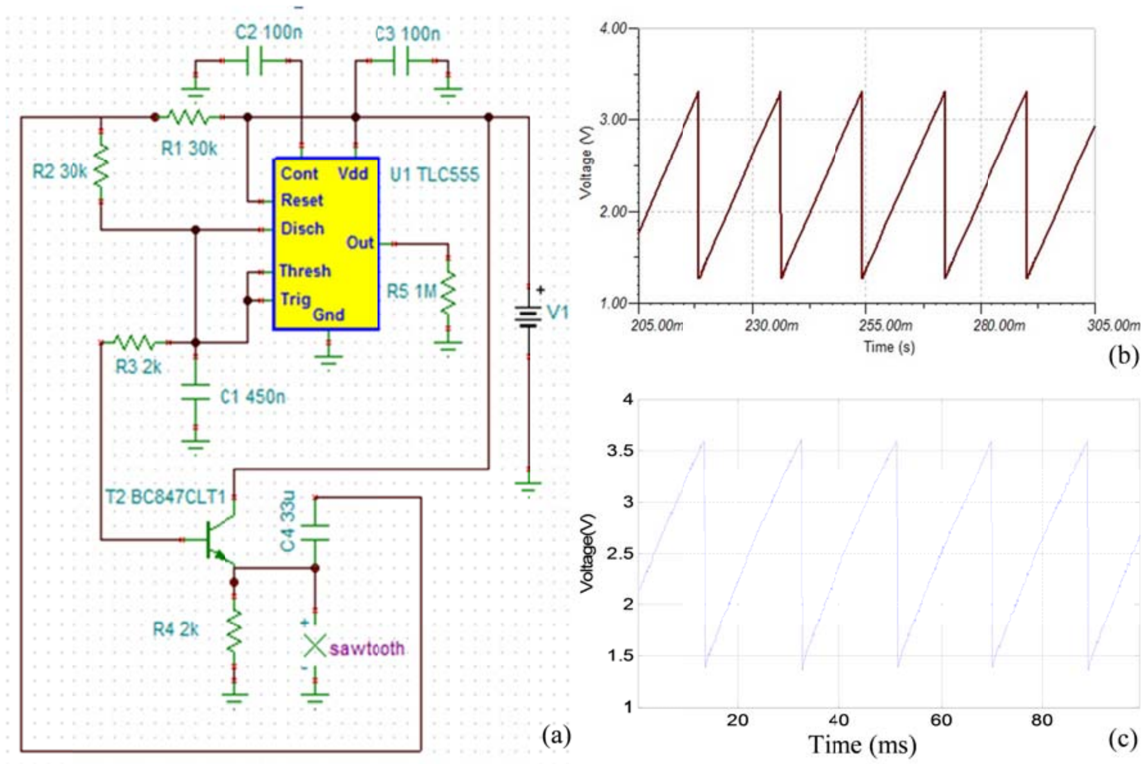

Figure 6.8 Saw tooth generator simulation and validation: (a). simulation schematic (b). simulated saw tooth wave (c) experimental saw tooth wave

In this study, a VCO (CVCO55BHS-5600-5800) chip was used. In order to achieve accurate frequency sweeping range the relationship between VCO input control voltage and output RF frequency was calibrated. A DC power supply is used to send the control voltage from 0.2 V to 6 V with a step of 0.2 V to the VCO. The VCO output was collected using a high frequency oscilloscope and the scope's built-in FFT function was used to determine the dominant frequencies of the received RF signal at different input voltages. The experimental frequency-voltage curve is represented in Fig 6.9. As expected, the experimental curve has a high degree of linearity (coefficient of the determination $R^2 = 0.999$). Base on the calibrated frequency-voltage relationship (as seen from the linear equation of the trend line), the frequency sweeping range of the VCO output is from 5.643 to 5.735 GHz if the input triangle voltage ranges from 1.4 to 3.6V. Since the VCO input impedance is only 50 Ω which does not match the output impedance of the triangle wave generator there will be a big voltage drop during signal transmission. In order to

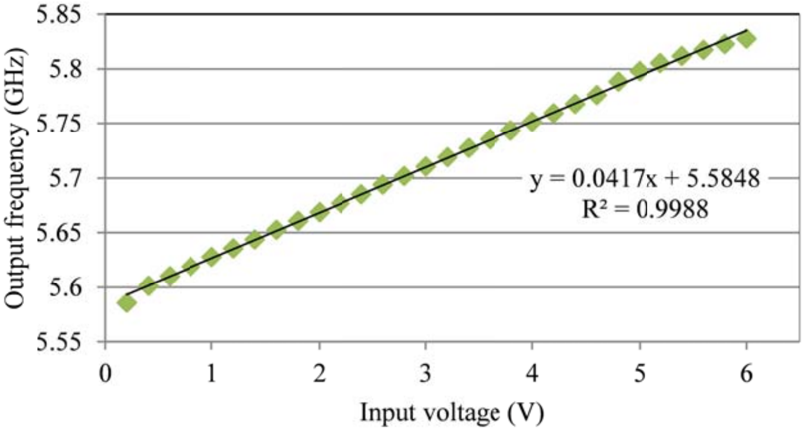

Figure 6.9 Calibrated relationship between the input voltage and the output frequency of the VCO

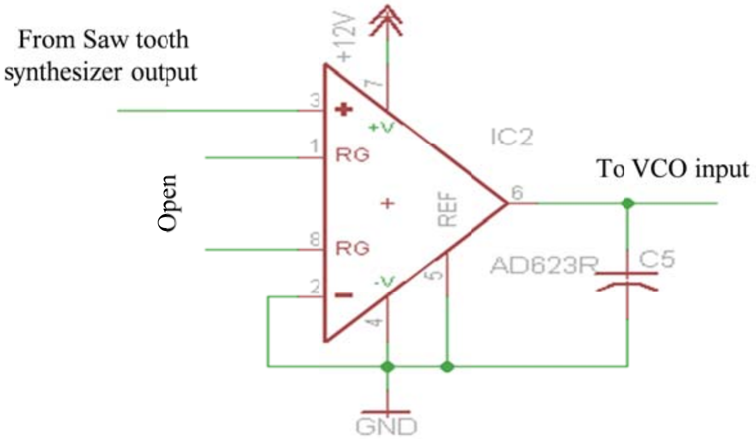

Figure 6.10 Schematic of the Voltage follower

solve this problem a voltage follower was developed which placed between the triangle wave generator and the VCO. The circuit schematic of the follower is shown in Fig 6.10. In the design, an AD623 op-amp was implemented and servers as unity gain voltage follower.

In order to make the FMCW synthesizer fit in the shoe all the electrical components are surface mounted and soldered on the PCB board. RT/duroid® 5880 Laminates are selected as the PCB material because of its low dissipation factor. The PCB layout is represented in Fig 6.11 and the fabricated circuit is shown in Fig 6.12. The dimension of the PCB circuit is 5 mm*4 mm. In the circuit there are two DC sources: 5 V and 12 V. The 5 V DC source provides the power for the triangle wave generator and the VCO. The 12 V one powers the voltage follower. Both of the two DC sources can be powered by a 3.7 V battery. The power consumption of the whole interrogation circuit is around 160 mW.

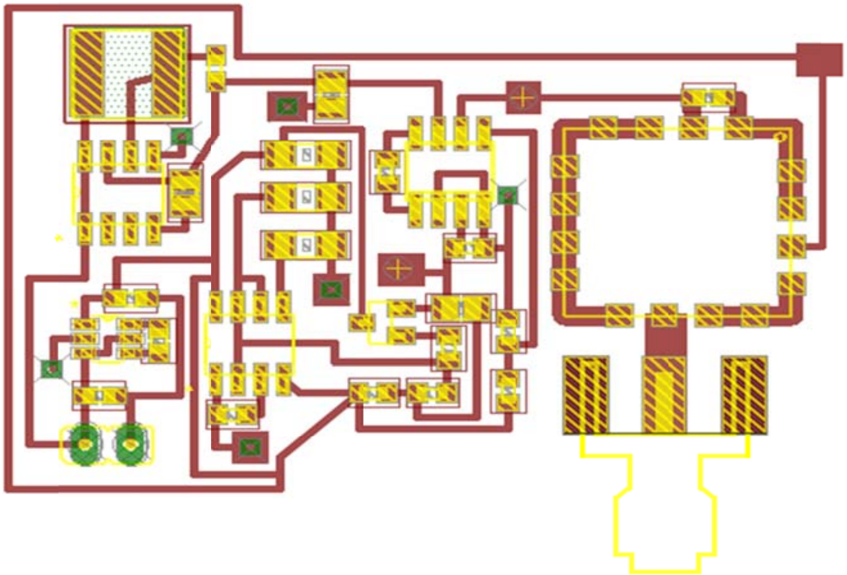

Figure 6.11 PCB layout of FMCW synthesizer

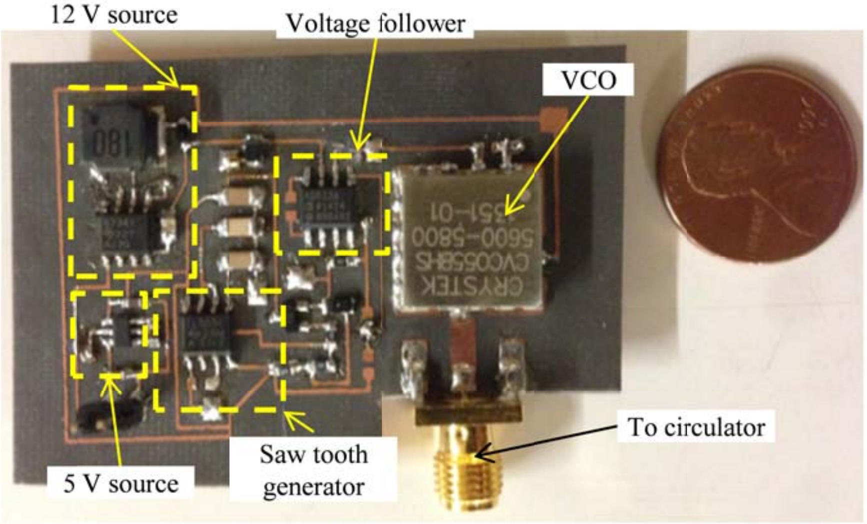

Figure 6.12 Fabricated FMCW synthesizer

6.4 Pressure testing and data analysis

Static pressure tests from 50 kpa to 550 kpa with a step of 100 kpa were conducted to characterize the pressure antenna sensor and FMCW generator circuit. First of all, the performance of the pressure sensor was validated using a VNA. As shown in Fig 6.13, the pressure sensor was clamped using the MTS compression machine and connected to the VNA

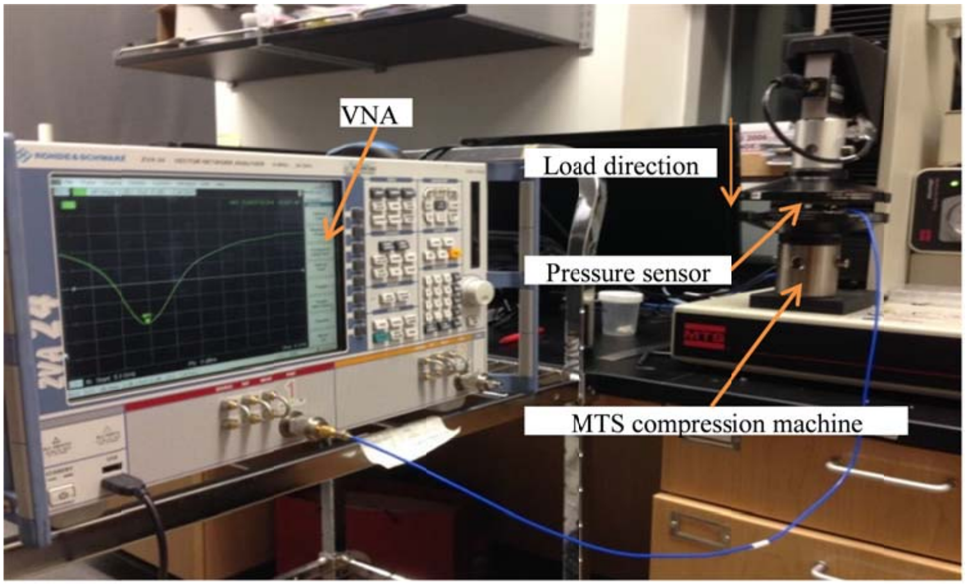

Figure 6.13 Experimental setup for static pressure tests using VNA

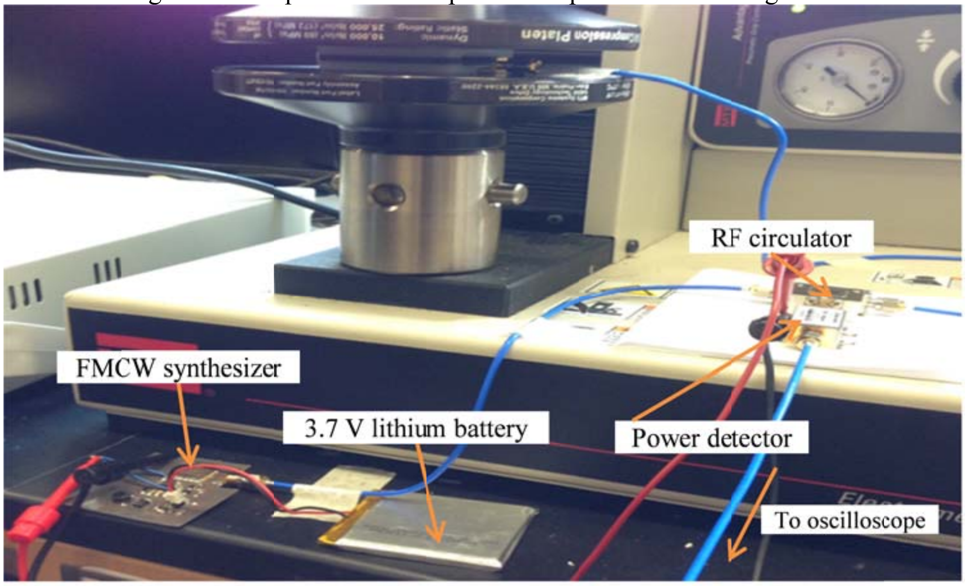

Figure 6.14 Experimental setup for static pressure tests using FMCW interrogator

using a coaxial cable. The frequency sweeping range of the VNA was set form 5.5 GHz to 6 GHz. Return-loss S11 curves were recorded every static pressure levels. Then the FMCW interrogation circuit was implemented to replace the VNA. The system setup was demonstrated in Fig 6.14. The PCB-based FMCW synthesizer was powered by a 3.7 V lithium battery. A RF circulator and a power detector were used for RF signal transmission and antenna return-loss measurement. The DC outputs of the power detector were collected by a high frequency oscilloscope at different pressure levels. The sampling rate of the oscilloscope was set as 50

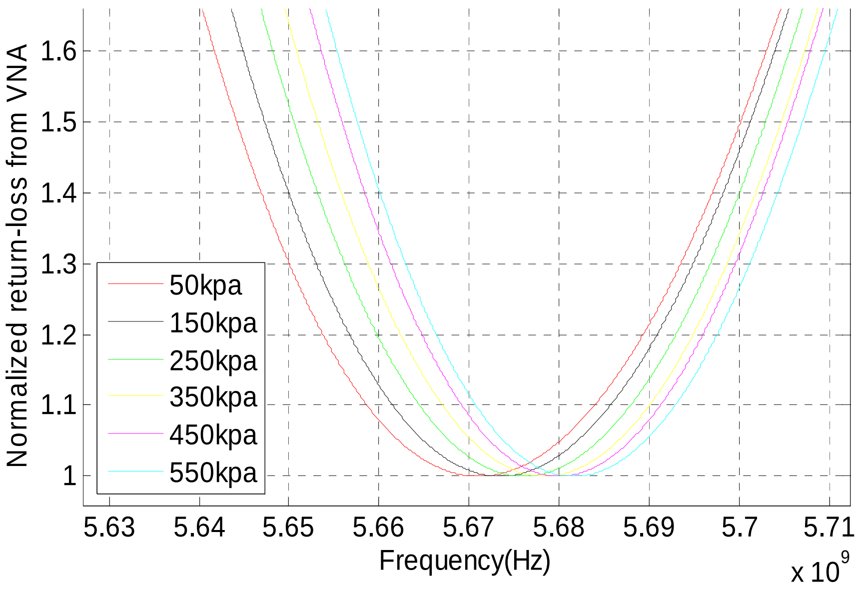

Figure 6.15 Normalized S11 return-loss measured from VNA

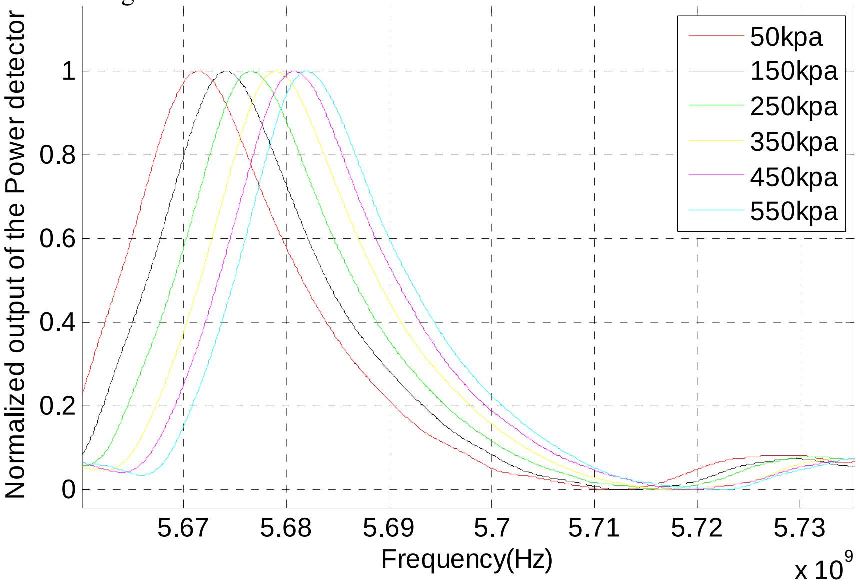

Figure 6.16 Normalized output from power detector

KHz. Since the frequency of the FMCW signal is 52.1 Hz and the carrier frequency sweeping range is from 5.65 GHz to 5.735 GHz the frequency resolution is (5.735-5.64)e6/(50000/52.1) = 98.99 kHz.

The VNA measured return-loss curves which are normalized respect to the minimum value are represented in Fig. 6.15. It is clearly indicated that the vertical pressure shifts the curve to the right. It means that the resonant frequency of the pressure senor increases when the pressure is higher. Similar to the VNA measurements, the normalized output of the power detector shift to the right through the increasing pressure. In Fig. 6.16, each curve represents the DC output in one FMCW period and all curves are normalized respect to their maximum voltages.

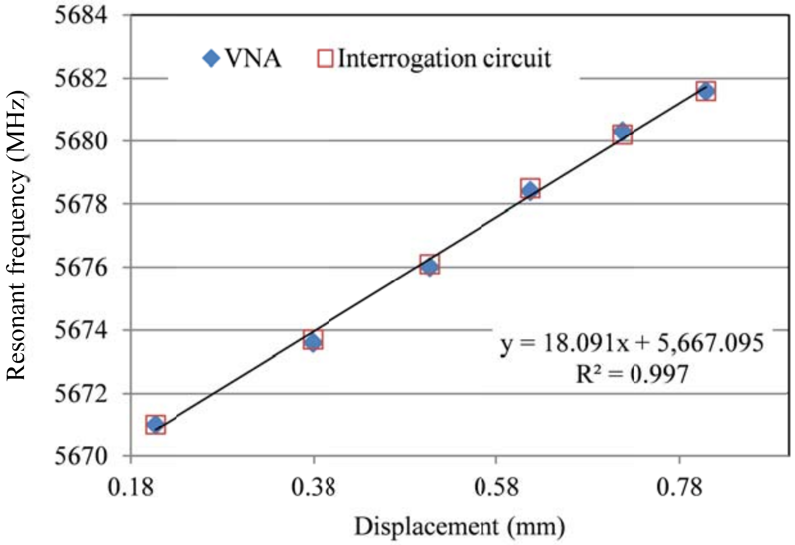

Figure 6.17 Experimental relationship between the resonant frequency and the downward displacement of the metal reflection plate

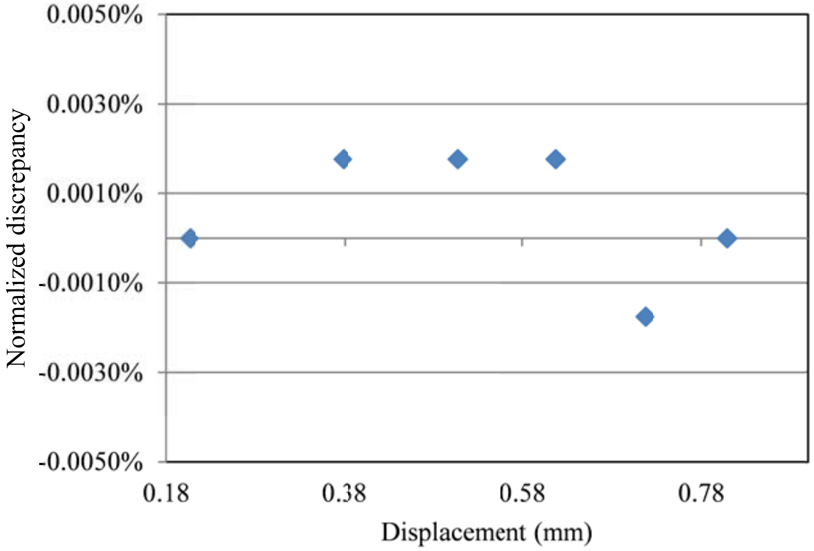

Figure 6.18 Normalized discrepancy of the resonant frequencies measured by VNA and FMCW interrogation circuit

From Fig.15 and 6.16, sensor's resonant frequencies, which measured by both VNA and FMCW interrogation circuit, under different pressures are achieved at the normalized amplitude "1" and plotted in Fig 6.17. In order to compare to the simulation results, the pressure scale is covered into the displacement scale based on the calibrated pressure-displacement relationship which is shown in Fig. 6.4. The experimental curves have a high degree of linearity (coefficient of the determination $R^2 = 0.997$), which validates the simulation results. Furthermore, the resonant frequencies measured using FMCW interrogation circuit and VNA match every with each other. The discrepancies which are normalized respected to the VNA readings are shown in Fig. 6.18. The discrepancies are very small which are within $\pm$ 0.002%. It proves that the designed FMCW interrogation circuit is accurate enough for pressure antenna sensor interrogation and resonant frequency detection.

6.5 Conclusions

In this study, a compact FMCW interrogation circuit for antenna pressure sensor was demonstrated. The interrogation circuit can realize a dynamic interrogation up to 52 Hz with a frequency resolution of 96 kHz. The accuracy of the proposed interrogation circuit was also validated using static pressure testing. The normalized discrepancies between the measurements of FMCW interrogator and VNA interrogator are within $\pm$ 0.002%. In future, Bluetooth function will be added into the interrogation circuit. Thus, wireless interrogation of the antenna pressure-sensor can be achieved.

CONCLUSIONS AND FUTURE WORKS

Wireless passive sensing technology is developing quickly for SMH in the past decade. Different passive sensors have been invented for wireless SMH, such as SAW sensor, inductive coupled sensor and RFID enabled sensor. All those sensors have their own advantages and drawbacks. Since SAW sensor is a passive sensor its lifetime is not limited by the battery. But in order to low maintain low propagation loss, the operation frequency of the SAW sensor is limited to tens of megahertz. And this frequency limitation makes the miniaturization of the passive antenna extremely difficult. Inductive coupled sensor can be implemented in harsh environment. However, the wireless interrogation of this sensor is a kind of near-field communication; the wireless interrogation distance is only a few centimeters. RFID sensor is a pass sensor which can be wirelessly interrogated with a long distance. But since it requires electronics in the sensor node it cannot be applied in the harsh environment.

Microstrip antenna-sensor is considered as a promising wireless sensor due to its compact size, passive operation and multi-modality sensitivity. Different wireless interrogation techniques of antenna-sensor were also developed to isolate the antenna backscattering from the background clutter and solve the self-jamming problem during the wireless communication. NTDR interrogation mechanism removes the background clutter by subtracting the reflected time domain signal acquired at both antenna termination states. However, since this method has low detection resolution of antenna-sensor's resonant frequency it cannot be used for wireless sensing system. Another wireless antenna-sensor interrogation mechanism was developed using step-frequency interrogation and antenna backscattering modulation for strain sensing. But, this mechanism can only be used for static testing due to the low stepping speed of the interrogation signal. Wireless interrogation mechanism for harsh environment was also developed. In this mechanism, antenna-sensor was considered as a resonator and there is no other electronics implemented in the sensor node.

However, the short wireless sensing distance limits the application of this interrogation mechanism. The goal of this thesis is developing a high-speed antenna-sensor interrogation mechanism which can be used in high-temperature harsh environment. First of all, a dynamic wireless interrogation mechanism was proposed using FMCW interrogation signal and antenna-backscattering modulation. A frequency resolution of 9.26 ppm and an interrogation rate up to 320 Hz were achieved. The accuracy of the wireless strain measurement system was validated using in-situ strain gauge measurements. The normalized differences between the calibrated antenna sensor and strain gauge measurements are less than 1% during the static stress testing, which proves the accuracy of the this interrogation mechanism. Vibration testing validated the proposed sensing system has good dynamic stress tracking ability up to 8 Hz.

Static wireless interrogation of antenna-sensor for high-temperature harsh environment application was also developed using time-gating technique and a new sensor node which has no electronics. Temperature testing (up to 280 °C) was conducted to validate the functionalities of the wireless sensor and interrogation system. The measured temperature sensitivity is 195.13 ppm/°C which matched very well with the theoretical value.

Dynamic interrogation mechanism of antenna-sensor for harsh environment was also realized by combining the FMCW interrogator and non-electronics sensor node. Due to antenna backscattering and background clutter have different beat frequencies, time gating can be applied on the frequency domain instead of the time domain to extract the antenna backscattering. As a result, substantial improvement on the interrogation speed can be achieved. In our study, an interrogation rate of 50 Hz was achieved for the proposed temperature sensing system. During the temperature testing, the measured resonant frequencies at different temperatures were compared to those measured from static VNA interrogator. The normalized discrepancy is only 3%, which proves its accuracy.

Further researches were done to reduce the size of the FMCW interrogator for foot pressure sensing system. A compact PCB FMCW synthesizer which has a dimension of 4 * 5 cm was developed. It can be powered by a 3.7 V lithium battery and the power consumption is only 160 mW. The normalized discrepancies between the measurements of compact FMCW interrogator and VNA interrogator are within ± 0.002%.

In the future, the research will focus on the antenna-sensor design using ceramic substrate and metallic material which have high-temperature limitation. Therefore, the new antenna-sensor can be used to measure the temperature up to 1200 °C. Techniques of designing, developing, and characterizing flexible dielectric substrate with controlled dielectric and mechanical properties will also be investigated to improve the antenna-sensor fabrication procedure.

Antenna-sensor with dual-sensitivity will also be developed for both mechanical stress and temperature measurement. In this study, resonant frequencies of antenna-sensor for both TM_{10} and TM_{01} mode will be used and decoupling data analysis algorithms will be generated to determine the sensing information form the frequency spectrum of the antenna-sensor.

Finally, multiple sensors will be placed on the sensor node to achieve wireless sensing network. Microstrip delay lines with different lengths will be added to connect different sensors. Due to the unique time delay caused by the delay line sensing information of each sensor can be separated from others' by using time gating technique. Real-time DAQ algorithms will be developed to extract the sensing information from each sensor from the mixed antenna-backscattering signals.

REFERENCE

[1] H. Sohn, C. R. Farrar, F. M. Hemez, D. D. Shunk, D. W. Stinemates, B. R. Nadler and J. J. Czarnecki, "A review of structural health monitoring literature: 1996-2001," *Los Alamos National Laboratory, USA*, 2003.

[2] C. R. Farrar and K. Worden. "An introduction to structural health monitoring." *Philos. Trans. A. Math. Phys. Eng. Sci. 365(1851),* pp. 303-315. 2007.

[3] J. P. Lynch and K. J. Loh. "A summary review of wireless sensors and sensor networks for structural health monitoring." *Shock Vib Dig 38(2)*, pp. 91-130. 2006.

[4] D. Li, S.-C. M. Ho, G. Song, L. Ren, and H. Li. "A review of damage detection methods for wind turbine blades." *Smart Mater. Struct.*, vol. 24, no. 3, p. 033001, 2015

[5] A. A. Khan, S. Zafar, N. S. Khan, and Z. Mehmood. “History, current status and challenges to Structural Health Monitoring System Aviation Field.” *J. Sp. Technol.*, vol. 4, no. 1, pp. 67–74, 2014.

[6] W. Staszewski, C. Boller, and G. Tomlinson,."Health Monitoring of Aerospace Structures. West Sussex, UK: John Wiley & Sons, 2003.

[7] V. Giurgiutiu, *Structural Health Monitoring with Piezoelectric Wafer Active Sensors*, Boston: Elsevier, 2008.

[8] P. Childs, J. Greenwood and C. Long. Review of temperature measurement. *Rev. Sci. Instrum. 71(8),* pp. 2959-2978. 2000.

[9] D. Bloomquist and S. Sheffield, "Thermocouple temperature measurements in shock-compressed solids," *J. Appl. Phys. 51(10),* pp. 5260-5266. 1980.

[10] K. Shannon and B. Butler. "A review of error associated with thermocouple temperature

measurement in fire environments," *Presented at Proceedings of the 2nd Fire Ecology Congress,* 2003.

[11] R. F. Wolffenbuttel and A. R. Schekkerman, "Integrated instrumentation amplifier for the phase readout of piezoresistive strain gauges," *Instrumentation and Measurement, IEEE Transactions on 43(6),* pp. 906-911. 1994.

[12] S. Kon, K. Oldham and R. Horowitz,. "Piezoresistive and piezoelectric MEMS strain sensors for vibration detection," *Presented at The 14th International Symposium on: Smart Structures and Materials & Nondestructive Evaluation and Health Monitoring*. 2007.

[13] R. Sakaguchi, C. Sasik, M. Bunczak and W. Douglas, "Strain gauge method for measuring polymerization contraction of composite restoratives," *J. Dent. 19(5),* pp. 312-316. 1991.

[14] S. M. Melle, A. T. Alavie, S. Karr, T. Coroy, K. Liu and R. M. Measures. "A bragg grating-tuned fiber laser strain sensor system." *Photonics Technology Letters, IEEE 5(2),* pp. 263-266. 1993.

[15] M. Davis and A. Kersey, "Application of a fiber fourier transform spectrometer to the detection of wavelength-encoded signals from bragg grating sensors," *Lightwave Technology, Journal of 13(7),* pp. 1289-1295. 1995.

[16] K. T. Grattan and B. Meggitt, *Optical Fiber Sensor Technology,* 1995

[17] T. G. Giallorenzi, J. A. Bucaro, A. Dandridge, G. Sigel, J. H. Cole, S. C. Rashleigh and R. G. Priest. "Optical fiber sensor technology." *IEEE Trans. Microwave Theory Tech. 30(4),* pp. 472-511. 1982.

[18] D. Estrin, L. Girod, G. Pottie and M. Srivastava. Instrumenting the world with wireless sensor networks. Presented at Acoustics, Speech, and Signal Processing, 2001.

Proceedings.(ICASSP'01). 2001 IEEE International Conference on. 2001.

[19] K. Romer and F. Mattern, "The design space of wireless sensor networks," *IEEE Wireless Communications 11(6),* pp. 54-61. 2004.

[20] Q. Tan, T. Wei, X. Chen, T. Luo, G. Wu, C. Li and J. Xiong. Antenna-resonator integrated wireless passive temperature sensor based on low-temperature co-fired ceramic for harsh environment. Sensors and Actuators A: Physical 236pp. 299-308. 2015.

[21] V. C. Gungor and G. P. Hancke. "Industrial wireless sensor networks: Challenges, design principles, and technical approaches." *Industrial Electronics, IEEE Transactions on 56(10),* pp. 4258-4265. 2009.

[22] I. F. Akyildiz, W. Su, Y. Sankarasubramaniam and E. Cayirci. Wireless sensor networks: A survey. *Computer Networks 38(4),* pp. 393-422. 2002.

[23] J. Yick, B. Mukherjee and D. Ghosal, "Wireless sensor network survey," *Computer Networks 52(12),* pp. 2292-2330. 2008.

[24] L. Zhang and Z. Wang, "Integration of RFID into wireless sensor networks: Architectures, opportunities and challenging problems," *Presented at 2006 Fifth International Conference on Grid and Cooperative Computing Workshops*, 2006.

[25] M. Kohvakka, M. Hännikäinen and T. D. Hämäläinen. Ultra low energy wireless temperature sensor network implementation. Presented at Personal, Indoor and Mobile Radio Communications, 2005. PIMRC 2005. IEEE 16th International Symposium on. 2005.

[26] J. M. Reason and J. M. Rabaey. A study of energy consumption and reliability in a multi-hop sensor network. *ACM SIGMOBILE Mobile Computing and Communications Review*

8(1), pp. 84-97. 2004.

[27] J. Polastre, R. Szewczyk and D. Culler, "Telos: Enabling ultra-low power wireless research," *IPSN 2005. Fourth International Symposium on Information Processing in Sensor Networks,* 2005.

[28] M. Ruiz-Sandoval, T. Nagayama and B. Spencer Jr,. "Sensor development using berkeley mote platform," *J. Earthquake Eng. 10(2),* pp. 289-309. 2006.

[29] B. F. Spencer, M. E. Ruiz-Sandoval and N. Kurata, "Smart sensing technology: Opportunities and challenges," *Structural Control and Health Monitoring 11(4),* pp. 349-368. 2004.

[30] Y. Lin, D. Sylvester and D. Blaauw, "An ultra low power 1V, 220nW temperature sensor for passive wireless applications," *Presented at 2008 IEEE Custom Integrated Circuits Conference*, 2008.

[31] V. Chawla and D. S. Ha, "An overview of passive RFID," *IEEE Communications Magazine 45(9),* pp. 11-17. 2007.

[32] R. Weinstein, "RFID: A technical overview and its application to the enterprise," *IT Professional 7(3),* pp. 27-33. 2005.

[33] L. Simson, A. Juels and R. Pappu, "RFID privacy: An overview of problems and proposed solutions," *Presented at IEEE Symposium on Security & Privacy*. 2005.

[34] A. P. Sample, D. J. Yeager, P. S. Powledge, A. V. Mamishev and J. R. Smith. Design of an RFID-based battery-free programmable sensing platform. *Instrumentation and Measurement, IEEE Transactions on 57(11),* pp. 2608-2615. 2008.

[35] M. Buettner, R. Prasad, M. Philipose and D. Wetherall. Recognizing daily activities with

RFID-based sensors. Presented at Proceedings of the 11th International Conference on Ubiquitous Computing. 2009.

[36] S. He, J. Chen, F. Jiang, D. K. Yau, G. Xing and Y. Sun. Energy provisioning in wireless rechargeable sensor networks. *Mobile Computing, IEEE Transactions on 12(10),* pp. 1931-1942. 2013.

[37] S. Sudevalayam and P. Kulkarni. Energy harvesting sensor nodes: Survey and implications. *Communications Surveys & Tutorials, IEEE 13(3),* pp. 443-461. 2011.

[38] F. Kocer and M. P. Flynn. An RF-powered, wireless CMOS temperature sensor. *Sensors Journal, IEEE 6(3),* pp. 557-564. 2006.

[39] M. K. Law, A. Bermak and H. C. Luong. A sub-μmW embedded CMOS temperature sensor for RFID food monitoring application. *IEEE J Solid State Circuits 45(6),* pp. 1246. 2010.

[40] N. C. Karmakar. *Handbook of Smart Antennas for RFID Systems* 2010.

[41] S. Shrestha, M. Balachandran, M. Agarwal, V. V. Phoha and K. Varahramyan, "A chipless RFID sensor system for cyber centric monitoring applications," *IEEE Trans. Microwave Theory Tech. 57(5),* pp. 1303-1309. 2009.

[42] D. Girbau, Á. Ramos, A. Lázaro, S. Rima and R. Villarino. Passive wireless temperature sensor based on time-coded UWB chipless RFID tags. *Microwave Theory and Techniques, IEEE Transactions on 60(11),* pp. 3623-3632. 2012.

[43] S. Hu, Y. Zhou, C. L. Law and W. Dou. Study of a uniplanar monopole antenna for passive chipless UWB-RFID localization system. *Antennas and Propagation, IEEE Transactions on 58(2),* pp. 271-278. 2010.

[44] A. Lazaro, A. Ramos, D. Girbau and R. Villarino. Chipless UWB RFID tag detection using continuous wavelet transform. *Antennas and Wireless Propagation Letters, IEEE 10*pp. 520-523. 2011.

[45] A. Ramos, D. Girbau, A. Lazaro, A. Collado and A. Georgiadis. Solar-powered wireless temperature sensor based on UWB RFID with self-calibration. *Sensors Journal, IEEE 15(7),* pp. 3764-3772. 2015.

[46] J. Yao, Y. M. Hew, A. Mears and H. Huang, "Strain gauge-enable wireless vibration sensor remotely powered by light," *IEEE Sensors Journal 15(9),* pp. 5185-5192. 2015.

[47] Y. Hew, S. Deshmukh and H. Huang, "A wireless strain sensor consumes less than 10 mW," *Smart Mater. Struct. 20(10),* pp. 105032. 2011.

[48] G. Scholl, F. Schmidt, T. Ostertag, L. Reindl, H. Scherr and U. Wolff, "Wireless passive SAW sensor systems for industrial and domestic applications," *Presented at Frequency Control Symposium, 1998. Proceedings of the 1998,* IEEE, 1998, .

[49] L. M. Reindl, A. Pohl, G. Scholl and R. Weigel, "SAW-based radio sensor systems," *IEEE Sensors Journal 1(1),* pp. 69-78. 2001.

[50] Q. Fu, H. Stab and W. Fischer, "Wireless passive SAW sensors using single-electrode-type IDT structures as programmable reflectors," *Sensors and Actuators A: Physical 122(2),* pp. 203-208. 2005.

[51] L. Reindl and W. Ruile, "Programmable reflectors for SAW-ID-tags," Presented at Ultrasonics Symposium, 1993. Proceedings., IEEE 1993. 1993.

[52] A. Pohl, "A review of wireless SAW sensors," *Ultrasonics, Ferroelectrics, and Frequency Control, IEEE Transactions on 47(2),* pp. 317-332. 2000.

[53] L. Reindl, I. Shrena, S. Kenshil and R. Peter. Wireless measurement of temperature using surface acoustic waves sensors. Presented at Frequency Control Symposium and PDA Exhibition Jointly with the 17th European Frequency and Time Forum, 2003. Proceedings of the 2003 IEEE International. 2003.

[54] J. R. Humphries and D. C. Malocha, "Wireless SAW strain sensor using orthogonal frequency coding," *Sensors Journal, IEEE 15(10),* pp. 5527-5534. 2015.

[55] J. Humphries and D. Malocha, "Passive, wireless SAW OFC strain sensor," *Presented at Frequency Control Symposium (FCS), 2012*, IEEE, 2012.

[56] L. Reindl, G. Scholl, T. Ostertag, C. Ruppel, W. Bulst and F. Seifert. SAW devices as wireless passive sensors. Presented at Ultrasonics Symposium, 1996. Proceedings., 1996 IEEE. 1996.

[57] T. Salpavaara, J. Verho, P. Kumpulainen and J. Lekkala. Wireless interrogation techniques for sensors utilizing inductively coupled resonance circuits. *Procedia Engineering* 5pp. 216-219. 2010.

[58] K. J. Loh, J. P. Lynch and N. A. Kotov, "Inductively coupled nanocomposite wireless strain and pH sensors," *Smart Structures and Systems 4(5),* pp. 531-548. 2008.

[59] J. Riistama, E. Aittokallio, J. Verho and J. Lekkala, "Totally passive wireless biopotential measurement sensor by utilizing inductively coupled resonance circuits," *Sensors and Actuators A: Physical 157(2),* pp. 313-321. 2010.

[60] J. C. Butler, A. J. Vigliotti, F. W. Verdi and S. M. Walsh. Wireless, passive, resonant-circuit, inductively coupled, inductive strain sensor. *Sensors and Actuators A: Physical 102(1),* pp. 61-66. 2002.

[61] V. Sridhar and K. Takahata. A hydrogel-based passive wireless sensor using a flex-circuit inductive transducer. *Sensors and Actuators A: Physical 155(1),* pp. 58-65. 2009.

[62] T. Salpavaara, J. Verho, P. Kumpulainen and J. Lekkala. Readout methods for an inductively coupled resonance sensor used in pressure garment application. *Sensors and Actuators A: Physical 172(1),* pp. 109-116. 2011.

[63] A. Daliri, A. Galehdar, W. S. Rowe, K. Ghorbani and S. John, "Utilising microstrip patch antenna strain sensors for structural health monitoring," *J Intell Mater Syst Struct 23(2),* pp. 169-182. 2012.

[64] H. Huang. Flexible wireless antenna sensor: A review. *Sensors Journal, IEEE 13(10),* pp. 3865-3872. 2013.

[65] U. Tata, H. Huang, R. Carter and J. Chiao. Exploiting a patch antenna for strain measurements. *Measurement Science and Technology 20(1),* pp. 015201. 2008.

[66] J. W. Sanders, J. Yao and H. Huang. Microstrip patch antenna temperature sensor. Sensors Journal, IEEE 15(9), pp. 5312-5319. 2015.

[67] I. Mohammad and H. Huang. "Monitoring fatigue crack growth and opening using antenna sensors." *Smart Mater. Struct. 19(5),* pp. 055023. 2010.

[68] J. Yao, C. Xu, A. Mears, M. Jaguan, S. Tjuatja and H. Huang. "Pressure sensing using low-cost microstrip antenna sensor." Presented at SPIE Smart Structures and Materials Nondestructive Evaluation and Health Monitoring. 2015.

[69] A. Deivasigamani, A. Daliri, C. H. Wang and S. John. A review of passive wireless sensors for structural health monitoring. *Modern Applied Science 7(2),* pp. 57. 2013.

[70] B. Ozbey, E. Unal, H. Ertugrul, O. Kurc, C. M. Puttlitz, V. B. Erturk, A. Altintas and H. V.

Demir. Wireless displacement sensing enabled by metamaterial probes for remote structural health monitoring. *Sensors 14(1),* pp. 1691-1704. 2014.

[71] S. Deshmukh and H. Huang. Wireless interrogation of passive antenna sensors. *Measurement Science and Technology 21(3),* pp. 035201. 2010.

[72] J. Boccard, T. Aftab, J. Hoppe, A. Yousaf, R. Hütter and L. M. Reindl, "High-resolution, far-field, and passive temperature sensing up to 700° C using an isolated ZST microwave dielectric resonator," *IEEE Sensors Journal 16(3),* pp. 715-722. 2016.

[73] D. Thomson, D. Card and G. Bridges. "RF cavity passive wireless sensors with time-domain gating-based interrogation for SHM of civil structures." *Sensors Journal, IEEE 9(11),* pp. 1430-1438. 2009.

[74] J. Chuang, D. Thomson and G. Bridges. Embeddable wireless strain sensor based on resonant RF cavities. *Rev. Sci. Instrum. 76(9),* pp. 094703. 2005.

[75] H. Cheng, X. Ren, S. Ebadi, Y. Chen, L. An and X. Gong. Wireless passive temperature sensors using integrated cylindrical resonator/antenna for harsh-environment applications. *Sensors Journal, IEEE 15(3),* pp. 1453-1462. 2015.

[76] A. Daliri, A. Galehdar, W. S. Rowe, S. John, C. H. Wang and K. Ghorbani. "Quality factor effect on the wireless range of microstrip patch antenna strain sensors." *Sensors 14(1),* pp. 595-605. 2014.

[77] X. Xu and H. Huang. Battery-less wireless interrogation of microstrip patch antenna for strain sensing. *Smart Mater. Struct. 21(12),* pp. 125007. 2012.

[78] X. Yi, C. Cho, J. Cooper, Y. Wang, M. M. Tentzeris and R. T. Leon, "Passive wireless antenna sensor for strain and crack sensing—electromagnetic modeling, simulation, and

testing," *Smart Mater. Struct. 22(8),* pp. 085009. 2013.

[79] X. Yi, T. Wu, Y. Wang, R. T. Leon, M. M. Tentzeris and G. Lant,. "Passive wireless smart-skin sensor using RFID-based folded patch antennas," *International Journal of Smart and Nano Materials 2(1),* pp. 22-38. 2011.

[80] Q. Qiao, L. Zhang, F. Yang, Z. Yue and A. Z. Elsherbeni, "Reconfigurable sensing antenna with novel HDPE-BST material for temperature monitoring," *Antennas and Wireless Propagation Letters, IEEE 12*pp. 1420-1423. 2013.

[81] M. Hasani, A. Vena, L. Sydanheimo, L. Ukkonen and M. M. Tentzeris, "Implementation of a dual-interrogation-mode embroidered RFID-enabled strain sensor," *Antennas and Wireless Propagation Letters, IEEE 12*pp. 1272-1275. 2013.

[82] X. Yi, T. Wu, Y. Wang and M. M. Tentzeris, "Sensitivity modeling of an RFID-based strain-sensing antenna with dielectric constant change," *IEEE Sensors Journal 15(11),* pp. 6147-6155. 2015.

[83] M. Hasani, A. Vena, L. Sydänheimo, M. M. Tentzeris and L. Ukkonen, "A novel enhanced-performance flexible RFID-enabled embroidered wireless integrated module for sensing applications," *IEEE Transactions on Components, Packaging and Manufacturing Technology 5(9),* pp. 1244-1252. 2015.

[84] H. Cheng, S. Ebadi, X. Ren and X. Gong. Wireless passive high-temperature sensor based on multifunctional reflective patch antenna up to 1050 degrees centigrade. *Sensors and Actuators A: Physical 222*pp. 204-211. 2015.

[85] J. Yao, S. Tjuatja and H. Huang. Real-time vibratory strain sensing using passive wireless antenna sensor. *Sensors Journal, IEEE 15(8),* pp. 4338-4345. 2015.

[86] M. I. Skolnik, *Introduction to Radar Systems*, 3rd ed. Boston, MA: McGraw-Hill, 2011.

[87] S. Bouaziz, F. Chebila, A. Traille, P. Pons, H. Aubert and M. Tentzeris, “Novel micro-fluidic structures for wireless passive temperature telemetry medical systems using radar interrogation techniques in ka-band,” *IEEE Antennas & Wireless Propagation Letters*, vol. 11, pp. 1706-1709, 2013.

[88] E. Hyun and J. Lee, "Method to improve range and velocity error using de-interleaving and frequency interpolation for automotive FMCW radars," *International Journal of Signal Processing, Image Processing and Pattern Recognition 2(2),* pp. 11-21. 2009.

[89] A. Tessmann, S. Kudszus, T. Feltgen, M. Riessle, C. Sklarczyk and W. H. Haydl," Compact single-chip W-band FMCW radar modules for commercial high-resolution sensor applications," *IEEE Trans. Microwave Theory Tech. 50(12),* pp. 2995-3001. 2002.

[90] A. G. Stove, "Linear FMCW radar techniques," *Presented at IEEE Proceedings F-Radar and Signal Processing*, 1992.

[91] H. Huang, J. Yao, and B. Shonkwiler, “Detecting impact damage in composite materials using microwave patch antennas,” *Presented at the 19th International Workshop on Electromagnetic Non Destructive Evaluation (ENDE2014)*, Xi’an China, Jun 2014.

[92] J. Yao, F. M. Tchafa, A. Jain, S. Tjuatja and H. Huang, "Far-field interrogation of microstrip patch antenna for temperature sensing without electronics," *IEEE Sensors Journal 16(19),* pp. 7053-7060. 2016.

[93] H. Mosallaei and K. Sarabandi. Antenna miniaturization and bandwidth enhancement using a reactive impedance substrate. *Antennas and Propagation, IEEE Transactions on 52(9),* pp. 2403-2414. 2004.

[94] L. Li, Y. Li, T. S. Yeo, J. R. Mosig and O. J. Martin. A broadband and high-gain metamaterial microstrip antenna. *Appl. Phys. Lett. 96(16),* pp. 164101. 2010.

[95] J. Yao, S. Tjuatja, and H. Huang, “A Compact FMCW Interrogator of Microstrip Antenna for Foot Pressure Sensing,” *Presented at Progress In Electromagnetics Research Symposium (PIERS)*, Shanghai, China, Augest 2016.

[96] H. Huang, J. Yao and S. Eilbeigi, “Simultaneous Shear/Pressure Antenna sensor,” *Presented at the 9th International Conference on Pervasive Technologies Related to Assistive Environment (PETRA)*, Corfu, Greece, July 2016.

[97] Balanis C, *Antenna Theory Analysis and Design*, 3rd ed. New York: Wiley Interscience, 2005.

[98] Rogers Corporation. (2016). RT/duroid® 5870 /5880 Datasheet. [Online].

[99] S. Chao, H. Wang, C. Su and J. G. Chern, "A 50 to 94-GHz CMOS SPDT switch using traveling-wave concept," *IEEE Microwave and Wireless Components Letters 17(2),* pp. 130-132. 2007.

[100] T. Johnson and S. P. Stapleton, "RF class-D amplification with bandpass sigma–delta modulator drive signals," *IEEE Transactions on Circuits and Systems I: Regular Papers 53(12),* pp. 2507-2520. 2006.

[101] J. A. Shaw, "Radiometry and the friis transmission equation," *American Journal of Physics 81(1),* pp. 33-37. 2013.

[102] W. Roh, J. Seol, J. Park, B. Lee, J. Lee, Y. Kim, J. Cho, K. Cheun and F. Aryanfar, "Millimeter-wave beamforming as an enabling technology for 5G cellular communications: Theoretical feasibility and prototype results," *IEEE Communications*

Magazine 52(2), pp. 106-113. 2014.

[103] Rogers Corporation. (2015). RO3000 Series Circuit Materials Datasheet. [Online].

[104] H. Huang and T. Bednorz. "Introducing S-parameters for ultrasound-based structural health monitoring." *Ultrasonics, Ferroelectrics, and Frequency Control, IEEE Transactions on 61(11),* pp. 1856-1863. 2014.